The Hydrodynamics of Pool-Riffle Sequences with Changing Bedform Length

by

Lana M. Obach

A thesis

presented to the University of Waterloo

in fulfillment of the

thesis requirement for the degree of

Master of Applied Science

in

Civil Engineering

Waterloo, Ontario, Canada, 2011

I hereby declare that I am the sole author of this thesis. This is a true copy of the thesis, including any required final revisions, as accepted by my examiners.

I understand that my thesis may be made electronically available to the public.

ABSTRACT

Previous research has demonstrated that pool-riffle bedforms play a critical role in channel stability and ecosystem health in many natural gravel-bed channels. Although the bedform length is known to scale with channel width, no experimental research has yet isolated the effect of bedform length on pool-riffle hydrodynamics. To improve the understanding of the hydrodynamics of these bedforms so that they can be better incorporated in restoration practices, flume experiments were conducted testing the flow at seven different bedform lengths.

Velocity profiles are measured in a 17 m flume with movable PVC bedforms using ultrasonic velocity profilers (UVPs). Smooth two-dimensional (no sinuosity) bedforms are used in order to isolate the key dynamics in convective acceleration and deceleration. The angle of transition between pool and riffle heights was 7°, so that permanent flow separation did not occur. Parameters calculated from the velocity and turbulence profiles include the Coles' wake parameter (a measure of the deviation from the log law), shear stress estimated from the velocity profile, shear stress estimated from the Reynolds shear stress, and vertical velocity. From the individual velocity time series, the integral length scale and the integral time scales are also calculated.

Overall, the length of riffles and pools exert a fundamental control on the distribution of flow and turbulence within a channel. In the pool, energy is dissipated both through turbulence and as the flow is redistributed to uniform flow conditions. In the riffle, kinetic energy increases as the flow velocity increases, and as the length increases, the flow moves towards a new uniform flow condition. The results start to explain the reasons behind the persistent scaling relation between width and bedform length. It can be concluded that uniform flow conditions exist at the end of the pool when the bedform length ratio is greater than approximately 1:5.0 when the riffle length is held constant, and that uniform flow conditions are no longer observed at the end of the pool when the bedform length ratio exceeds 1:7.0 when the pool length is held constant.

Future research should concentrate on extending the results to include three-dimensional pool-riffle configurations, repeating bedform configurations, internal scaling parameters, and sediment transport. Ultimately, as the hydrodynamics of pool-riffle sequences are better understood, better bedform designs can be implemented in restoration projects.

ACKNOWLEDGMENTS

I would like to thank my supervisor, Dr. Bruce MacVicar, for his constant advice and support throughout the entire research project. Without your previous trials and tribulations on the experimental set-up and MATLAB coding, this project would not have been completed on time.

I would also like to thank Dr. Jim Best and Dr. Marcelo Garcia from the University of Illinois at Urbana-Champaign for their collaboration and access to their hydrosystems research facility. I would also like to thank Gianluca Blois for his hospitality during my stay in Champaign, IL, while I was conducting my research.

In addition, I would like to acknowledge financial contributions from the Natural Sciences and Engineering Research Council of Canada (NSERC), the Ontario Government Scholarship Program (OGSST), as well as the Ven Te Chow Hydrosystems Laboratory in Champaign IL, USA.

Lastly, I would like to thank my husband, Matthew, for his patience, knowledge, and support during these past two years.

TABLE OF CONTENTS

List of Figures

List of Tables

List of Symbols

A = amplitude

a = major axis

b = minor axis

c = speed of sound in the transmitting medium

C = constant of integration

C_s = speed of sound in water

d = total depth

d_i = diameter

dt = time step

dx = distance step

$\frac{du}{dz}$ = slope

f = frequency

f_c = cutoff frequency

f_D = sampling frequency

f_N = Nyquist Frequency

f_o = ultrasound basic frequency

f_{50} = half-power frequency

F_D = Doppler shift

Fr = Froude number

g = gravitational acceleration

h = height

k = order of exponential filter

L = meander length

n = length of the raw data

N_{DU} = number of 'Doppler units'

P_{max} = maximum depth

r = distance from the transducer

r_m = mean radius of curvature

Re = Reynolds number

R_t = time-shifted cross-correlation sequence

R_x = spatial cross-correlation sequence

t = time

t_o = reference time

T = time at which correlation exceeds 99% significance limit

T_w = temperature of water

δt = time delay

Δt = change in time

u = velocity

u_c = maximum velocity in the profile

u_i = filtered velocity series

u_r = velocity of the particle in the measuring volume

$\bar{u}$, U = average streamwise velocity

u^* = shear velocity

$\bar{u}'$ = deviation from the streamwise velocity

$\vec{u}$ = component of velocity

Δu_i = first derivative of filtered velocity series

$\Delta^2 u_i$ = second derivative of filtered velocity series

V_{range} = maximum measurable velocity component range

ΔV = velocity resolution

w = width

$\bar{w}$, W = average velocity components in the vertical direction

$\bar{w}'$ = deviation from the vertical velocity

x = downstream direction

X = distance at which correlation exceeds 95% significance limit threshold

x_o = reference position

Δx = change in position

z/Z = normalized water depth

z = height above the bed

z_c = height above the bed at which the maximum velocity occurs

z_o = reference bed level

Greek Symbols

α = major axis standard deviation

β = minor axis standard deviation

θ = rotation angle of the principal axis

κ = von Karman constant

λ = wavelength

λ_U = maximum velocity threshold

μ = kinematic viscosity

Π = Coles' wake parameter

ρ = water density

$\hat{\sigma}$ = standard deviation

τ = shear stress

τ_r = shear stress estimated from the Reynolds stress profile

τ_{Re} = Reynolds stress

τ_u = shear stress estimated from the velocity profile

Chapter 1

INTRODUCTION

Rivers have played a crucial role in the development of human society. Many cities and civilizations around the world were founded along rivers, using the river as their primary water source and incorporating the river with their industrial needs to help grow their economy. With time, it is frequently the case that the rivers that humanity has benefited from have been degraded to an unnatural state. Rivers have been lined with concrete or rip rap to reduce erosion and to remove water as quickly as possible during high flow events (Keller, 1978). Rivers have been straightened, reducing the meander length, so that new development can be constructed in previously flooded areas (Newbury and Gaboury, 1993). Rivers have been dredged so that large boats can pass through the channel for economic gain (Holtschlag and Hoard, 2009). These changes to the rivers natural morphology has led to a decrease in ecological habitat diversity in the river, created dangerous fast flowing channels during runoff and peak event conditions, and led to unstable channels leading to flooding and damage to urban and rural structures (Harper et al., 1998; Walker et al., 2004).

With increasing problems related to reduced aquatic habitats, poor channel stability, and flashy runoff conditions in domesticated and urban watersheds, river rehabilitation and restoration have become important activities to reverse or counteract anthropogenic incursions. The number of river rehabilitation projects has increased significantly in the past couple of decades with more than 14 000 river rehabilitation projects undertaken since 1964 in the United States alone, with a total cost of $7.2 billion USD (NRRSS, 2006). Over 94% of these river rehabilitation projects have occurred since 1990 (NRRSS, 2006). In southern Ontario, over 120 river restoration projects took place in the 1990s at a total cost exceeding $11.9 million CAD (Heaton et al., 2002).

River rehabilitation must integrate ecology, geomorphology, hydraulics, and hydrology to be successful (Clarke et al., 2003; Julien, 2002). Engineers and scientists have been working together to understand river mechanics and how geomorphology affects the hydrodynamic forces governing the motion of water and sediment in river systems (Julien, 2002). A pool-riffle sequence is a bedform naturally found in rivers, and is well known to be a stable geomorphic feature (Yang, 1971; Keller and Melhorn, 1978;

Wohl et al., 1993). In recent rehabilitation projects in low-slope gravel-bed rivers, pool-riffle bedforms have frequently been used to create stable river channels which can promote a diverse range of aquatic habitats (Pasternack et al, 2008). However, both successes and failures have been seen with this type of bedform installed during rehabilitation projects, where some bedforms have become eroded or filled in with sediment leading to failures in stability and increased flooding (Walker et al., 2004). These results indicate that there is still more to learn about the pool-riffle sequence and its application to river rehabilitation projects.

The overall objective of this thesis is to characterize the hydrodynamics of the pool-riffle sequence at different bedform lengths. This includes obtaining an understanding of how the flow and turbulence in a channel, particularly close to the bed and side walls, change as the scale of the bedform changes.

In this thesis, the known literature on riffle-pool sequences will be reviewed, including previous field and laboratory studies completed on the topic to provide the background needed for clarity of the research. At the end of the literature review section, the detailed objectives of this thesis are outlined. Next the laboratory equipment used to test the effect of the length of the pools and riffles on hydrodynamics of pools will be explained. Following this, the experimental methods and analysis of the measured velocities will be outlined. A complete set of results of the hydrodynamic changes observed over different pool and riffle lengths are presented after the experimental methods are outlined. Finally, a discussion of the results and a comparison to previous studies are presented, concluding with recommendations for future research.

Chapter 2

LITERATURE REVIEW

This section of the thesis defines the pool-riffle sequence, and discusses the scale at which they naturally occur in open channels. The role that pool-riffle sequences play on channel stability and ecology is highlighted, previous field and laboratory studies that have been completed on the topic are summarized, and the objectives of this research are outlined.

2.1 Bedform Classification

Each channel reach in different drainage systems will have different characteristics associated with them including slope, grain size, and roughness elements. In alluvial systems, which are systems that have unconsolidated materials that can be eroded and transported by the flow (Keller and Melhorn, 1978), there are five distinct reach bedform types that can occur based on different combinations of these characteristics. The different bedform types include cascade, step pool, plane bed, pool-riffle, and dune ripple (Montgomery and Buffington, 1997) (Figure 1).

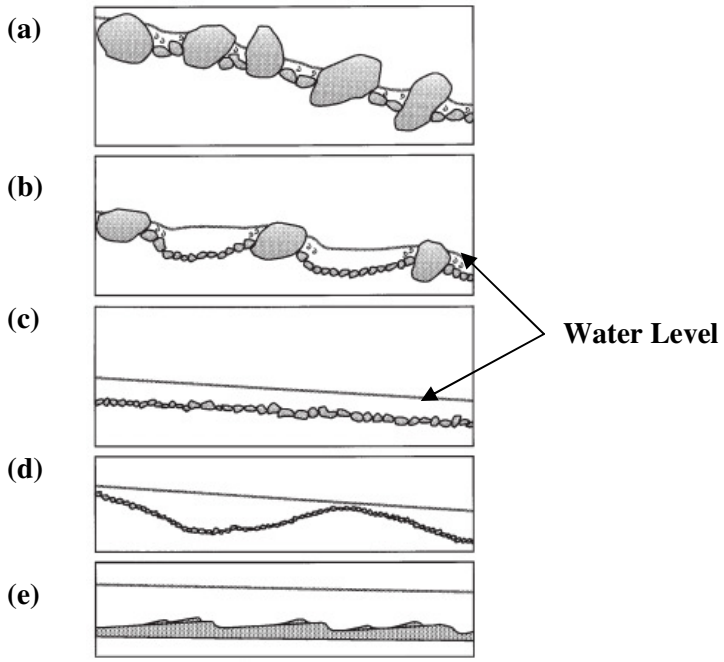

Figure 1. Sketch of the side view of different bedform classifications including (a) cascade, (b) step pool, (c) plane bed, (d) pool-riffle, and (e) dune ripple (Montgomery and Buffington, 1997).

Montgomery and Buffington (1997) summarized the differences of the five bedform morphologies to mark the differences in the major fundamental factors that govern each type (Table 1).

Table 1. Diagnostic features of different alluvial bedforms.

	Dune Ripple	Pool-Riffle	Plane Bed	Step Pool	Cascade
Type of bed material	Sand	Gravel	Gravel-cobble	Cobble-boulder	Boulder
Bedform pattern	Multilayered	Laterally oscillatory	Featureless	Vertically oscillatory	Random
Dominant roughness elements	Sinuosity, bedforms (dunes, ripples, bars), grains, banks	Bedforms (bars, pools), grains, sinuosity, banks	Grains, banks	Bedforms (steps, pools), grains, banks	Grains, banks
Pool spacing (channel widths)	5 to 7	5 to 7	None	1 to 4	<1

All of these different bedform types are important and unique in alluvial stream systems, however, this thesis focuses only on the pool-riffle sequence.

2.2 Pool-Riffle Form

Pools and riffles are common bedforms in alluvial gravel-bed streams (Leopold and Wolman, 1957; Keller, 1978; Leopold et al., 1964), but can also be found in some bedrock streams (Keller and Melhorn, 1978). Pool-riffle sequences generally occur over low slopes, generally less than 2% (Montgomery and Buffington, 1997; Madej, 1999; Carling, 1991). Pools are the topographic low of the bed, while the riffles are the topographic high (Montgomery and Buffington, 1997), and collectively they create an undulating bedform (Leopold et al., 1964) (Figure 2).

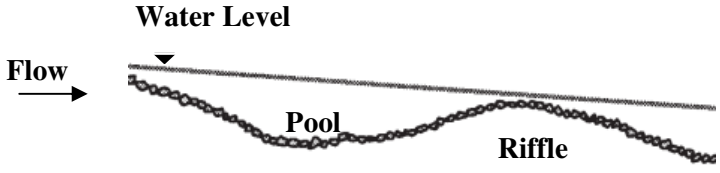

Figure 2. Side view of a pool-riffle sequence (Montgomery and Buffington, 1997).

The dominant type of planform morphology of a pool-riffle sequence is meandering, which increases the length and reduces the slope of a channel (Leopold et al., 1964). With the development of

meandering, there is a decrease in tractive forces on the apex of the bends, and it is in this location where point bars develop (Church and Jones, 1982). From the planform view, it is common to associate bars with the pool-riffle sequence, and collectively they are referred to as the pool-riffle-bar sequence (Figure 3).

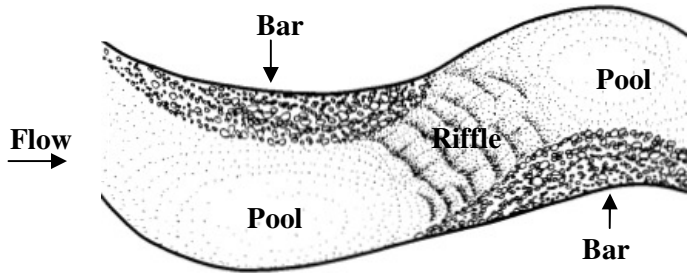

Figure 3. Planform view of a pool-riffle bar sequence (Montgomery and Buffington, 1997).

Riffles are shallower, steeper zones, and occur in the straight segments, or cross overs, between pools. Riffles store very little transient material, and their relatively large material may be exposed (Church and Jones, 1982). Riffles are generally lobate in shape, and slope alternately first toward one bank and then toward the other (Leopold et al., 1964; Church and Jones, 1982). Due to the diagonal riffle, the water in the channel at low flow bends around the low point of the riffle, and thus tends to have a sinuous course even within the banks of a straight reach (Leopold et al., 1964). Riffles are typically 15-33% wider at the tops than pools during low flows (Richards, 1976). Riffles act as energy dissipators in the channel, and promote stability while also allowing periodic transport of coarse bed sediment to occur at high flows (Church and Jones, 1982).

Pools are associated with adjacent point bars which results in an asymmetric cross-channel profile (Keller and Melhorn, 1978). The pool length varies with channel gradient and sediment transport conditions (Wohl et al., 1993), while the pool depth is also influenced by discharge (Lisle, 1982, Wohl et al., 1993). The pool exit is an area of strong turbulent energy dissipation, increased sediment deposition, and also controls the size of material leaving the pool (Sear, 1996; Thompson et al, 1996).

Alluvial bar development requires a sufficiently large width to depth ratio and small grain sizes relative to boulders that are easily mobilized and stacked by the flow (Church and Jones, 1982). Bars deform slowly and are usually adjusted to long-term trends in sediment load and flow conditions due to their size and mobility, and therefore, they are relatively stable (Lisle, 1982). Point bars have the length and height on the same order as the channel width and mean depth, respectively (Church and Jones, 1982). Bars act as energy dissipators that help maintain channel stability when sediment transport is occurring, and provide a major storage sink for bed material sediments (Church and Jones, 1982).

A pool-riffle sequence can be formed freely or it can be forced. A freely formed pool (Figure 4a) is created by the lateral mobility of the channel (Keller and Melhorn, 1978), sediment transport, flow regime, and the resulting convergence and divergence of flow (Montgomery et al., 1995). Forced pools (Figure 4b) are created by bends or obstructions which cause flow convergence and turbulent velocity fluctuations that scour the channel bed (Montgomery et al., 1995).

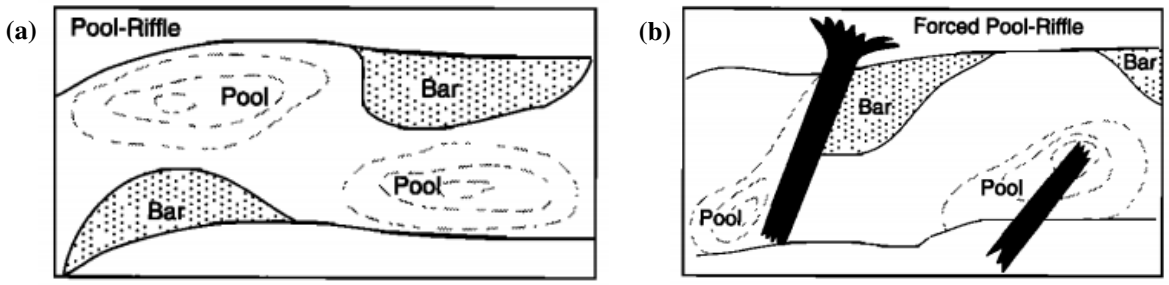

Figure 4. A sketch of a (a) freely formed pool-riffle sequence, and (b) forced pool-riffle sequence (Montgomery et al., 1995).

The pool-riffle sequence is present in nearly all perennial channels in which the bed material is larger than coarse sand, but appears to be most characteristic of gravel bed streams (Leopold et al., 1964; Montgomery and Buffington, 1997). Pool-riffle sequences will have a range of bed material size, with a coarse layer on the surface layer and a finer layer on the subsurface (Leopold et al., 1964). The largest bed materials in pools, in both the surface and subsurface, are significantly finer than the largest bed materials in the riffles (Keller, 1971; Leopold et al., 1964). In riffles, the largest material commonly forms in a single layer on the surface (Keller, 1971).

The pool-riffle sequence is persistent over a range of flow stages (Keller and Melhorn, 1978), so it generally does not migrate up and down the channel (Leopold et al., 1964; Wilkinson et al., 2004). Very rarely is the whole bed in motion, and the material eroded from one riffle is commonly deposited on a downstream riffle (Sear, 1996; Montgomery and Buffington, 1997). Pools tend to scour at high flow and fill during low flow, whereas riffles fill during high flow and winnow during low flow (Leopold et al., 1964; Keller, 1971; Keller and Melhorn, 1978). High sediment loads tend to bury pool-riffle sequences, whereas frequent high magnitude flows wash them out (Keller 1978). Thompson (2002) assessed the morphological response of pools to flow dynamics, finding that pools elongate at a rate of ten times at which they deepen.

In a study on alluvial streams, Madej (1999) determined that immediately after a high flow event (12 year flood), a river bed will reorganize itself so that the pool-riffle bar sequence has very low variations in elevation. As time elapses from the high flow event, the stream bed topography increases in elevation variations and the sequence of pool, riffle, bar, becomes more pronounced. Following a pulse

of sediment and debris during a high flow event, the river channel processes and forms will adjust and evolve towards a new equilibrium (Madej, 1999). High flow disturbances leading to a stable riffle-pool channel will result in riffles becoming more extensive, pools becoming smaller and shallower, and bed material textures becoming finer (Lisle, 1982).

2.3 Scale of Form

Rivers tend to move and shift in two dimensions, laterally and vertically. Lateral movements have been studied extensively due to the ease of measurement from maps, and have revolved around the parameters of meander length or wavelength (L), amplitude (A), and mean radius of curvature (r_m) (Figure 5).

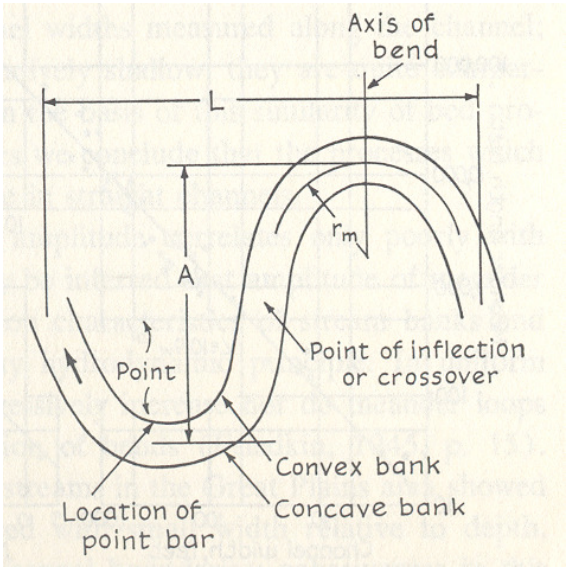

Figure 5. Lateral scaling parameters of a river from the planform view (Leopold et al., 1964).

These studies led to the discovery that a channel wavelength is a function of stream width, and therefore, indirectly a function of discharge. Thus, twice the distance between successive points of inflection is proportional to the square root of the dominant discharge (Leopold and Wolman, 1957). The straight line mean meander wavelength roughly averages to be eleven times the mean channel width (w) (Leopold and Wolman, 1964), as:

$$L = 10.9w^{1.01} \quad (1)$$

From these studies, it was also determined that the channel's mean radius of curvature can be empirically related to the mean meander length (Leopold et al., 1964), as:

$$L = 4.7r_m^{0.98} \quad (2)$$

The exponents in Equations 1 and 2 are so close to unity that they are generally both considered as linear, and hold true for a very large range of stream sizes (Figure 6).

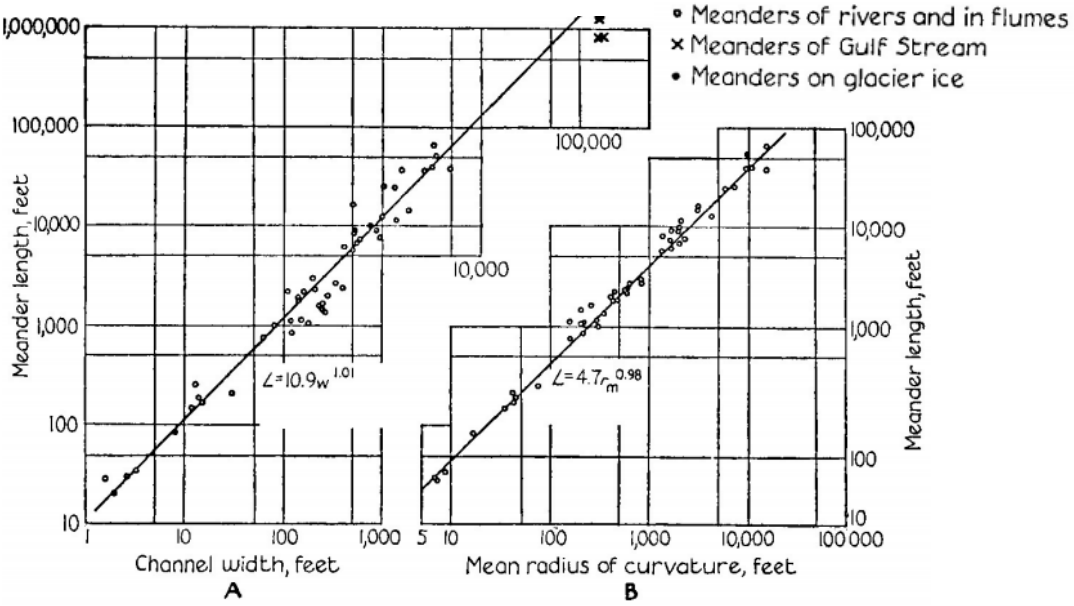

Figure 6. Channel width and mean radius of curvature relationship to meander length (Leopold et al., 1964).

In contrast to planform measurements, the vertical form of rivers has only been studied extensively in the last few decades. Recent studies have focused on the characterization of riffle height, riffle length, pool depth, pool length, and the riffle to riffle length (Figure 7).

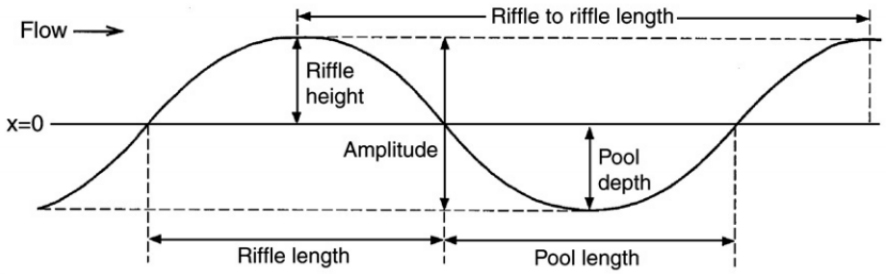

Figure 7. Vertical scaling parameters in a river from the side view (Lofthouse and Robert, 2008).

Freely formed pool-riffles units, for both straight and meandering channels, generally have a riffle to riffle spacing at a repeating distance equal to between 5 and 7 channel widths (Leopold et al., 1964; Keller and Melhorn, 1978). The similarity in spacing of riffles in both straight and meandering channels suggests that the mechanism that maintains pool-riffle sequences is present in both channel types, and is not necessarily only associated with a meandering channel (Leopold et al., 1964). In forced pool-riffles, there is no regular spacing due to the random forcing element distribution (Madej, 1999), and can result in a spacing value of less than the expected range for freely formed pool-riffle channels (Montgomery et al., 1995). Lofthouse and Robert (2008) found that an increase in the overall curvature increases the pool-riffle sequence length. When this occurs, the curvature appears to promote an increase in pool length more so than an increase in riffle length.

The riffle height is constantly proportioned to the bankfull depth at a ratio of approximately 1:0.16, and the riffle length was found to increase with the bankfull depth (Carling and Orr, 2000). The pool becomes longer and shallower as the gradient and available energy decreases in a channel (Wohl et al., 1993). The average riffle length is in the range of 1:1.3 to 1:4.5 channel widths (Lisle, 1986; Carling and Orr, 2000). The average ratio of pool length to riffle length has been reported in the range of 1:0.9 to 1.9 (Carling and Orr, 2000; Wohl et al., 1993) in channels with gradients less than or equal to 2%.

2.4 Pool-Riffle Function

A pool-riffle sequence has two main functions in a channel, a physical function, and an ecological function. Physically, the pool-riffle provides stabilization to a channel by minimizing the potential energy loss per unit mass of water (Yang, 1971; Keller and Melhorn, 1978; Wohl et al., 1993). At low flows, the riffle acts as a hydraulic control on flow through the upstream pool (Richards, 1978). At high flows, the riffle is submerged and functions more as a large-scale roughness element (Caamaño et al., 2009) to help stabilize the channel. In a study by Walker et al. (2004) it was found that 50 to 100% of the total energy was lost over a riffle and its downstream pool at high flows, proving its importance as a stabilization structure.

The pool-riffle sequence plays an important role on the river's ecology (Moir et al., 2004). The pool-riffle sequence has a wide range of conditions that are needed for ecological diversity in a healthy channel (Boulton and Lake, 1992), including substrate particle size, current velocity, turbidity, dissolved oxygen, aquatic vegetation, depth, temperature, and substrate permeability (Gorman and Karr, 1978; Brown and Brown, 1984; Ross et al., 1993). A range of these optimal conditions are found in both the pool and riffle, in general, however, it was found that higher densities of organisms are found in the riffle compared to the pool (Logan and Brooker, 1983).

Pool-riffle sequences play an important role in the welfare of fish habitat as they provide areas for feeding, breeding, and cover (Keller, 1978). Stuart (1953) found that water flowing through the gravel of a riffle provides aeration essential to the incubation of fish ova. Pool-riffle sequences create a backwater effect (backs water upstream in the pool due to the riffle), which is necessary to produce high-quality spawning habitats in the tail end of the pool, for such species as the Chinook, steelhead, and Atlantic salmon (Heggberget et al, 1986; Pasternack et al., 2008). Backwater conditions also help embryos survive moderate floods by limiting the sediment's mobility to only partial transport, whereas in a uniform channel the full bed would be mobile (Pasternack et al., 2008). The natural sorting of coarser bed material on riffles provides an optimal environment for bottom dwelling organisms (Keller, 1978). These organisms are important as they provide a major food source for the fish (Keller, 1978).

2.5 River Restoration

Anthropogenic disturbances such as urban development, flood controls, and mining practices degrade channels and lead to a decrease in natural pool-riffle topography, and a reduction in ecological populations (Harper et al., 1998; Walker et al., 2004). Rehabilitation projects have tried to recreate channel forms believed to be favored by particular species (specie- or habitat-driven rehabilitation). These projects have not addressed the underlying geomorphical processes that create channel form, which results in non-self-sustaining channels that require continual management input (Clarke et al., 2003). River rehabilitation must integrate ecology, geomorphology, hydraulics, and hydrology to be successful (Clarke et al., 2003).

More recent rehabilitation projects in gravel-bed rivers have used riffle-pool sequences as the central bedform (Pasternack et al, 2008). These projects, however, if improperly constructed, can lead to increased flooding, channel instability, and no net increase of ecological populations (Walker et al., 2004). An increase in understanding of the characteristics and controls of the pool-riffle mechanics is essential in water resource planning, ecological, and river management issues (Harper et al., 1998; Newbury and Gaboury, 1993; Clifford et al., 2006; Clifford, 1993a; Emery et al., 2003; Clarke et al., 2003).

2.6 Field Observations

Most pool-riffle studies previously conducted have been field experiments. The data collected from field experiments are often limited to one size of bedform, low flow measurements, and often sectioned averaged profiles (Clifford and Richards, 1992; MacVicar and Roy, 2007a). Very few studies measure with a high spatial density at high flood stages, and very few divide the channel into sections based on expansion and contraction boundaries (MacVicar and Roy, 2007a). This means that most

measurements previously taken are insufficient to characterize the pool-riffle hydrodynamics because they did not take into account the vertical and lateral distribution of flow parameters, or sensitive enough to measure the near-bed velocities during expansion and contraction in the pool (MacVicar and Roy, 2007a). Spatially distributed data is also hard to collect in the field due to unsteady flow and changing discharge (Booker et al., 2001). However, despite these measurement disadvantages, field observations do provide critical information as their bedform geometries form naturally, their roughness and planforms are accurate, their discharge fluctuates, and sediment transport processes can be observed and measured.

A number of different hypotheses derived from field studies are available to explain the formation and maintenance of pools, including the reversal hypothesis (Keller, 1971), the lateral variability of flow parameters (Clifford and Richards, 1992, Thompson et al., 1998, Booker et al., 2001, MacWilliams et al, 2006, Harrison and Keller, 2007), scour by turbulent vortices (Clifford, 1996; Thompson, 2006), and routing of sediment around the deepest part of the pool due to flow convergence and divergence (Booker et al., 2001; MacWilliams, et al., 2006). However, there is no consensus on one hypothesis to explain all pool-riffle sequences.

2.6.1 The Reversal Hypothesis

The first pool-riffle theory was proposed by Keller (1971), who postulated a reversal hypothesis. This hypothesis stated that as the river discharge increased, the velocity in the bottom of a pool increased faster than that in the riffle, so that eventually the bottom velocity of a pool exceeded that in the riffle. Therefore, when the bottom pool velocity is greater than the bottom riffle velocity, the tractive forces will be greater in the pool. As a result, the largest bed-load particles will generally be found on the riffles, and the relatively finer particle will be found in the pools. Keller developed his reversal idea on Gilbert's (1914) observations of contrasting surface agitation in streams during high and low flows while working for the U.S. Geological Survey (Clifford and Richards, 1992). Keller proposed his hypothesis after measuring the bed velocity at 15.2 mm (0.05 ft) above the stream bed over four different flow rates (Figure 8).

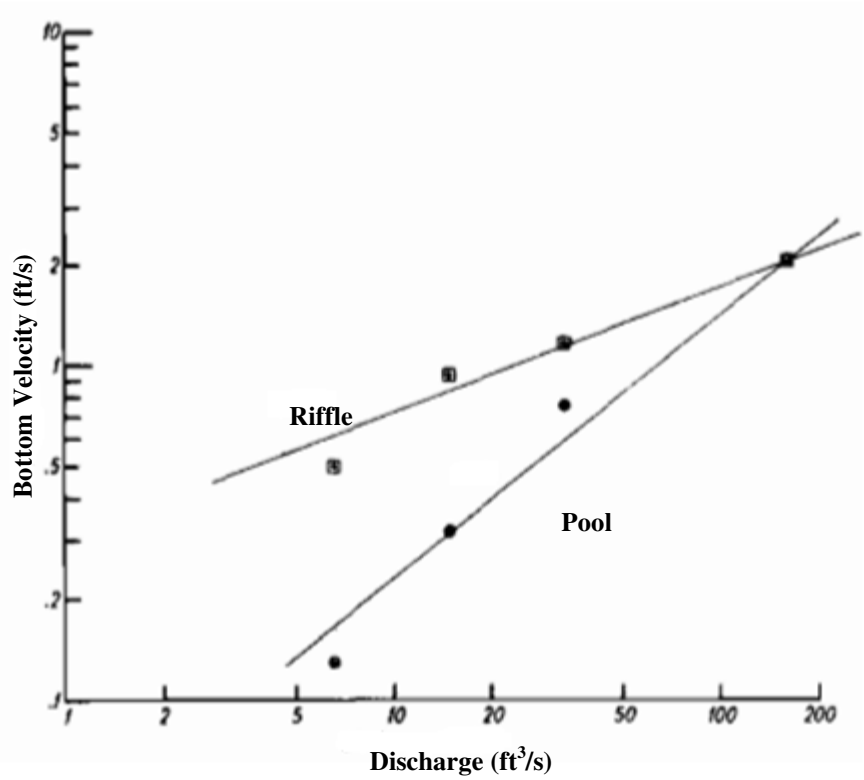

Figure 8. The velocity above the stream bed for both the riffle and pool (Keller, 1971).

It should be noted that the axes are on a log-log scale, and the data trends follow the power law. Using this theory, at low flow below the velocity reversal, only the finer materials are transported, and the bottom velocity of the pool is less than the bottom velocity of the riffle. At an increasing discharge, a transitional point is reached where the bottom velocity of the pool equals the bottom velocity of the riffle, and large material can be transported through both the riffle and the pool. Above the reversal velocity, the bottom velocity of the pool exceeds that of the riffle, and the largest bed materials are moved through the pool and deposited in the stable area of the river in the riffle (Keller, 1971) (Figure 9).

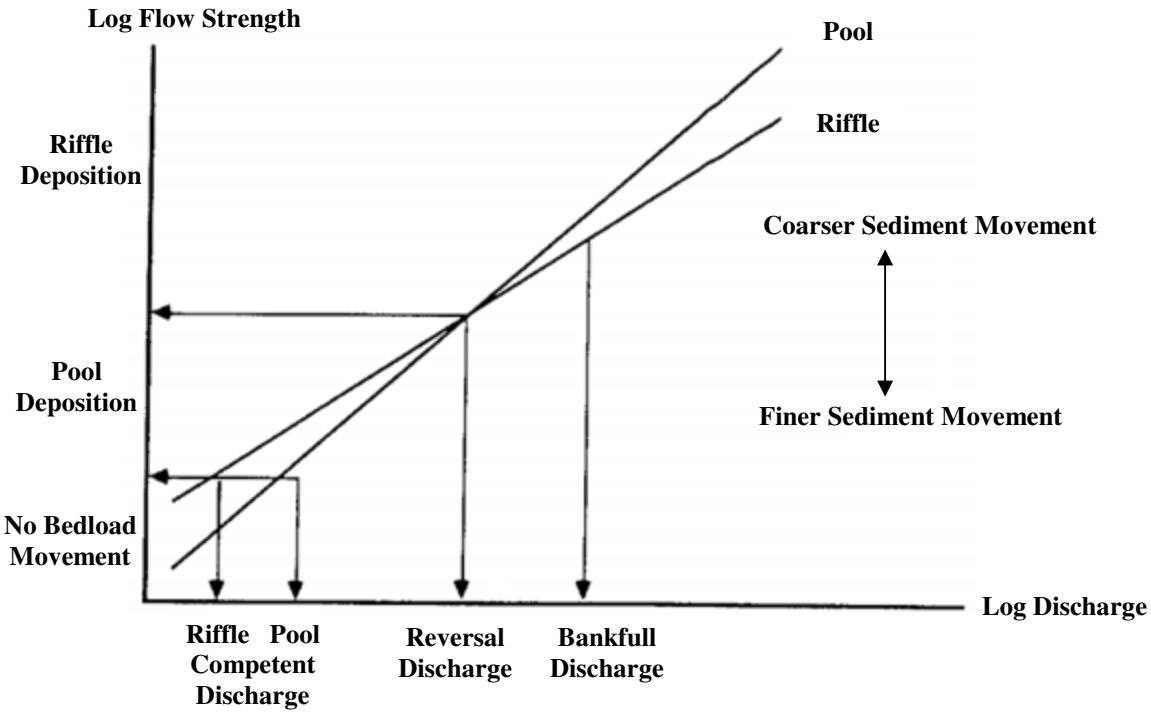

Figure 9. A diagram explaining the reversal hypothesis (Clifford and Richards, 1992).

Several investigations have shown that a velocity reversal can occur (Keller, 1971; Thompson et al., 1996, 1998, 1999; Booker et al., 2001; Wilkinson et al., 2004; MacWilliams et al., 2006). Some have found that with increasing discharge the velocity increased at a faster rate through the pool than over the riffle, but did not observe a velocity reversal (Carling, 1991; Cliffords and Richards 1992), and there are some that reject the existence of a velocity reversal (Teleki, 1972; Bhowmik and Demissie 1982). Although literature suggests that a velocity reversal does occur in some cases, it is not clear whether a reversal of some type is a prerequisite for pool maintenance, or whether the reversal hypothesis is applicable for all pool-riffle sequences (MacWilliams et al., 2006).

Clifford and Richards (1992) discussed four key weaknesses of Keller's reversal theory. First, Keller assumed the power law holds in both riffle and pool over the entire range of discharge, even though the only data comes from low flow discharge measurements. Second, Keller assumed these relationships are similar for riffles and pools regardless of the type of channel planform, whether straight, meandering, or braided. Third, the reversal hypothesis assumed occurrence for all paired cross-sections designated as riffle and pool, regardless of spatial variables. Fourth, Keller used mean sectioned velocities and mean boundary shear stresses, while the researchers who compared their studies to his used a wide range of different flow parameters.

Clifford and Richards (1992) state that if a reversal was going to occur, three things would have to happen for continuity. First, the riffle and pool channel geometries would have to vary so that the rate

of change of the discharge in the cross-sectional area of the riffle is greater than that in the pool. Second, the differences in hydraulic geometries would have to result from the changing distribution of flow resistance through the sequence. Third, scour would have to take place at high discharges in the pool and or deposit sediment at the riffle in order to reduce variations in the channel's cross-sectional area. Clifford and Richards (1992) conclude that the nature of the flow-sediment interaction in riffle-pool sequences may be more complicated than the reversal hypothesis implies. Although many studies of pool-riffle sequences have shown a convergence in mean parameters in pools and riffles, there is no evidence to suggest that a reversal in velocity must occur, and in fact some studies have shown that reversals do not occur at all in pool-riffles (Teleki, 1972; Bhowmik and Demissie, 1982). It can be shown that a velocity reversal can occur due to non-uniform flow without causing a continuity problem, which will be discussed in Section 2.7.2. Overall, from the different studies mentioned, it can be concluded that the reversal hypothesis is not the dominant process for pool-riffle maintenance (Clifford and Richards, 1992; MacWilliams et al., 2006).

2.6.2 Lateral Variability of Flow Parameters

Clifford and Richards (1992) found that a reversal, or the absence of a reversal, could be demonstrated simultaneously for a given pool-riffle sequence depending on which parameter was evaluated, and the location of the measurement cross-section. This was due to the fact that there is lateral variability of flow parameters, including both velocity and shear stress.

It was shown that the velocity in the pool section had the highest value near the surface and that the flow tended to be concentrated in the center of the channel (MacWilliams et al., 2006). The velocities near the bed were the highest on the point bar side of the pool rather than in the deepest section of the pool (MacWilliams et al., 2006). Clifford and Richards (1992) showed that the location of the maximum flow velocity shifts with changing discharge. Thompson et al. (1998) demonstrated that for two channels with similar cross-sectional areas, lateral constriction could result in higher local velocities in the pool compared to an adjacent riffle. By considering this lateral variability, it has been found that the highest shear stresses frequently occur over the upstream riffle, and in a narrower zone through the pool cross section, despite the overall widening of the pool downstream of the riffle cross-section (MacWilliams et al., 2006; Harrison and Keller, 2007). The maximum bed shear stresses at the pool cross-section occur on the slope of the point bar rather than in the deepest part of the pool over a range of discharges (MacWilliams et al., 2006).

The lateral variability of flow parameters means that measuring the velocity at a fixed point for an entire cross-section would not explain pool-riffle maintenance. Therefore, section-averaged data is not sufficient in explaining the characteristics of flow and form interactions of pool-riffle sequences (Clifford and Richards, 1992; MacWilliams et al., 2006).

2.6.3 Scour by Turbulent Vortices

Generally, when considering sediment transport, shear stress is typically only estimated from the magnitude or gradient of velocity near the bed, and used in a threshold prediction, like in the Shields diagram (Dingman, 2009). However, it is known that turbulent fluctuations can increase the rate of sediment transport (Nelson et al., 1995; Sumer et al., 2003), and can even cause sediment transport when the ensemble mean average critical shear stress hasn't been achieved (Hassan and Woodsmith 2004; Sumer et al., 2003). The observation of higher turbulence at the head of the pool (Sear, 1996; Clifford, 1996) led to the hypothesis that turbulent vortices are important for pool scour (Thompson 2002, 2004, 2006, 2007). This theory explains why the pool center has a larger range of grain sizes despite having a lower mean bed shear stress, as the turbulence effects causes enhanced entrainment and higher bed load transport. (Hassan and Woodsmith, 2004).

2.6.4 Routing of Sediment around the Deepest Part of the Pool

Another theory for the maintenance of pool-riffle sequences involves the convergence and divergence of flow. Studies have observed that many pools are characterized by a constricted width, which forces the lateral convergence of flow at the head of the pool (Montgomery et al., 1995; Thompson et al., 1998). This constriction causes a zone of greater near-bed velocities, shear stresses, turbulence, and secondary circulation (MacWilliams et al., 2006; Montgomery et al., 1995; Thompson et al., 1998; Sear 1996; Harrison and Keller, 2007). This zone is the primary pathway for sediment routing through or around the pool, and can serve to route the coarsest sediment away from the deepest part of the pool (MacWilliams et al., 2006; Booker et al., 2001) (Figure 10).

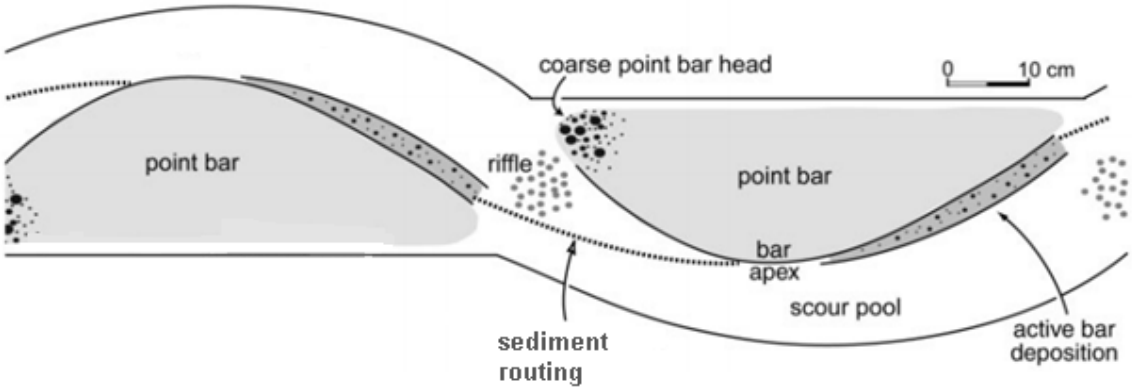

Figure 10. Routing of sediment around deepest part of the pool due to flow convergence from the plan view (Pyrce and Ashmore, 2005).

Results indicate that the maintenance of the pool-riffle morphology could be due to the lack of sediment being routed into pools rather than an increased ability to erode based on convergence of flow into the pool (Booker et al., 2001). At the tail of the pool, the flow diverges at the head of the riffle, leading to deposition on the riffle and the maintenance of a topographic high at the tail of the pool (MacWilliams et al., 2006). Therefore, it has been hypothesized that flow convergence routing could be the primary mechanism for maintaining pool-riffle morphology (MacWilliams et al., 2006; Booker et al., 2001; Harrison and Keller, 2007).

Each of the three theories discussed above have been observed at different field sites, and the authors concluded that each method could be the primary maintenance mechanism. However, in a field study by MacVicar and Roy (2007a,b), near-bed velocity reversals, flow convergence, and turbulence generation were all present at bankfull discharge.

This led to the conclusion that multiple mechanisms need to be considered to explain pool formation and maintenance (Thompson and Wohl, 2009; MacVicar and Roy, 2009; MacVicar and Rennie, in review), and that previous theories have had too narrow of a focus. The key to understanding how pools and riffles are formed and maintained may be hidden by a lack of understanding of the more general process of convective acceleration and deceleration.

2.7 Laboratory Studies

A number of laboratory studies have been completed that, despite their idealized conditions, serve to characterize flow properties during convective acceleration and deceleration. There are two limitations in existing laboratory studies that prevent direct comparisons between field and lab results. First, existing flume tests of accelerating and decelerating flow typically measure parameters along the channel centerline as a means of minimizing the variability induced by proximity to the channel walls (Song and Chiew 2001). Due to the fact that bedforms scale with the channel width, the effect of the channel side wall is needed to understand the effect the wall has on accelerating and decelerating flow (MacVicar and Rennie, in review). The second limitation is that flume experiments are set to have equilibrium flow, but bedforms produce non-equilibrium transitions between accelerating, decelerating, and more uniform sections (MacVicar and Rennie, in review). Despite the disadvantages that laboratory studies have, they are useful in obtaining detailed measurements over a high spatial density and wide range of flows. The first non-uniform flow studies were completed on flat beds to try to understand the underlying differences non-uniform flow has on velocity, shear stress, and turbulence.

2.7.1 Flat Bed Experiments with Non-Uniform Flow

Changes in bed elevation in pool-riffle sequences cause non-uniform flow. Non-uniform flow occurs when the flow is accelerating or decelerating, and causes the slope of the water surface to not be parallel to the bed surface (Figure 11).

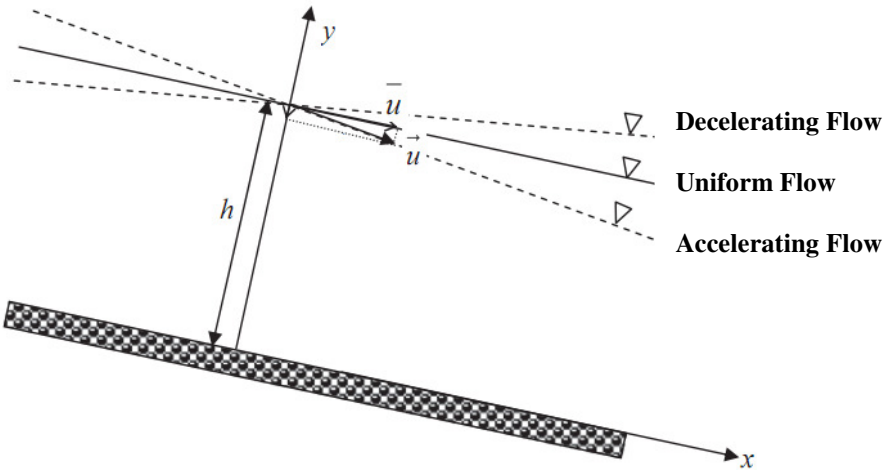

Figure 11. A sketch of uniform, decelerating and accelerating flow (Yang and Chow, 2008).

In uniform flow in open channels with flat beds, the streamwise velocities as well as Reynolds stresses follow characteristic profiles due to a balance between the accelerating force of gravity and the resistance from the channel bed and walls (Nezu and Nakagawa, 1993). The streamwise velocity follows the log-law, and the Reynolds stress follows a linear profile decreasing in value as the distance from the bed increases. In non-uniform flow, however, these characteristic profiles do not hold true, as the velocity profile in the outer region will follow the Coles' wake law (Coles, 1956), and the Reynolds stress will no longer follow a linear profile (Yang and Chow 2008). The streamwise velocity in accelerating flow generally has a convex shape (bowed outwards) when compared to uniform flow, where the peak velocity occurs below the water surface (Coles, 1956; Kironoto and Graf, 1995; Song and Chiew, 2001; Yang and Chow, 2008) (Figure 12a). In decelerating flow, the velocity has a relatively less-convex shape, with the peak velocity near the water surface. The Reynolds stress is relatively lower in accelerating flow but relatively higher in decelerating flow when compared to the linear uniform distribution. In an accelerating flow, the Reynolds shear stress has a concave shape, and in decelerating flow, the Reynolds stress becomes convex in shape, with the peak below the water surface (Figure 12b). The Reynolds stress tends to increase above the bed in decelerating flow due to the generation of new turbulence (Kironoto and Graf 1995, Song and Chiew 2001, Yang and Chow 2008).

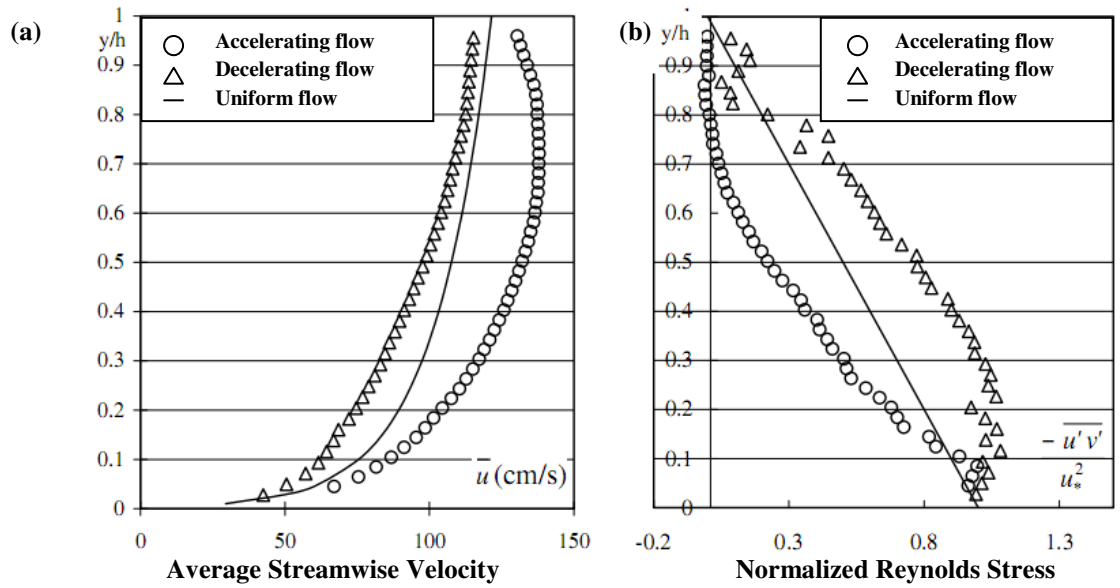

Figure 12. Velocity and Reynolds stress profiles for uniform and non-uniform flow for (a) streamwise velocity and (b) Reynolds stress (Yang and Chow, 2008).

Accelerating flow generally hampers the turbulence intensities, whereas decelerating flow strengthens the turbulence (Figure 13). This understanding leads back to the explanation as to why the Reynolds shear stress increases in decelerating flow (Figure 12b).

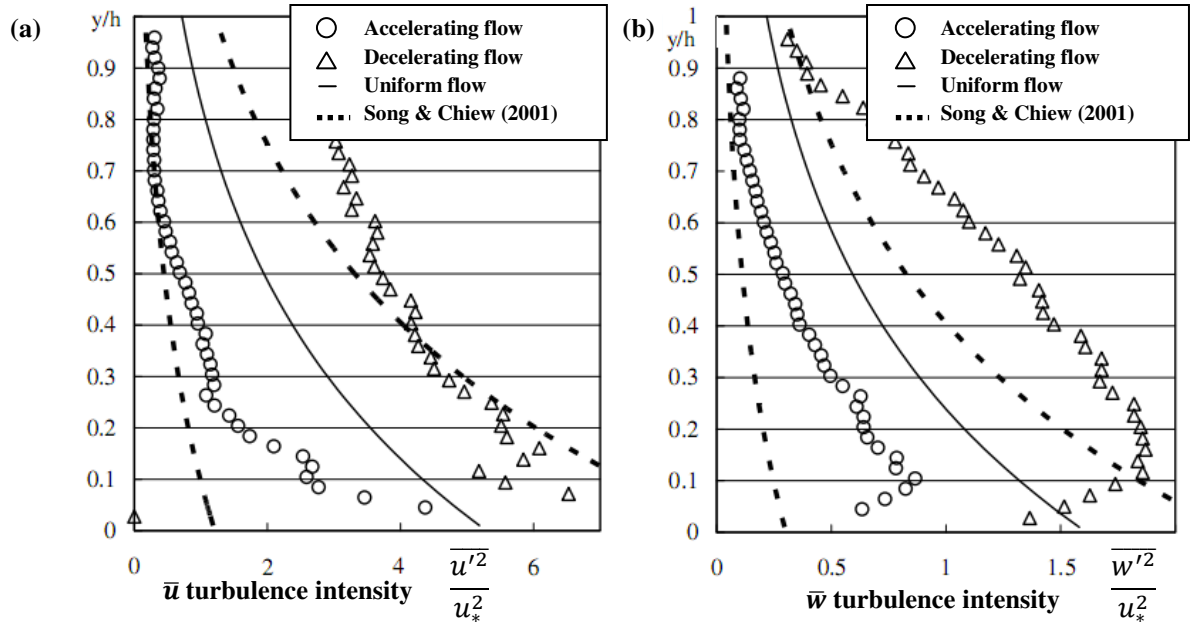

Figure 13. Turbulence intensity for uniform and non-uniform flow in the (a) streamwise, and (b) vertical direction (Yang and Chow, 2008).

The most important characteristic of non-uniform flow is the existence of the non-zero wall-normal velocity. Decelerating flow generates upward wall-normal velocities, whereas accelerating flow yields downward wall-normal velocities (Yang and Chow, 2008). In uniform flow, the wall-normal velocity is generally considered zero, however, it can be non-zero due to secondary currents. Secondary currents are velocity vectors perpendicular to the main streamwise flow (Dingman, 2009), i.e., flow moving up or down, or laterally across the channel. Secondary currents can be caused by the centripetal force resulting from channel curvature, heterogeneous turbulence generation, or both (Van Balen et al., 2009). Secondary currents can lower the maximum velocity location some distance below the water surface at the centerline, a phenomenon known as 'velocity dip' (Dingman, 2009). The magnitude of secondary currents is typically on the order of 5% of the downstream velocity (Dingman, 2009), but has been shown to be as great as 40% in very sharp bends (Blanckaert, 2009). Regardless, if the wall-normal velocity are caused by secondary currents or non-uniform flow, the turbulence characteristics are substantially different if the directions of wall-normal velocity are opposite, as the wall normal velocity is responsible for the re-distribution of Reynolds shear stress and turbulence intensities (Yang and Chow, 2008) (Figure 12b and Figure 13).

2.7.2 Non-Flat Bed Experiments with Non-Uniform Flow

The effect of a non-flat bed must also be considered along with the flat bed experiments previously discussed, further complicate the flow hydrodynamics over pool-riffle sequences. In a pool-riffle sequence the flow depth will first increase and then decrease in a pool, causing flow deceleration in the upstream portion of the pool and flow acceleration in the downstream portion of the pool (MacVicar and Rennie, in review). This non-uniformity causes a distribution of the velocity so that the streamwise velocity is relatively low near the bed and high near the water surface in decelerating flow, while the velocity in accelerating flow will have relatively high velocities near the bed (Kironoto and Graf 1995, Song and Chiew 2001, Yang and Chow 2008, Afzalimehr and Rennie 2009). This increase in near-bed velocity provides the necessary mechanism for a velocity reversal to occur in the downstream portion of the pool, but only in zones of flow acceleration (MacVicar et al., 2010). The velocity reversal does not contradict the laws of continuity as partial flow velocity reversal can occur without a reversal of bulk velocity (MacVicar et al., 2010). These results are similar to those of Thompson (2004), who found that the velocity reversal can occur without a bulk velocity reversal when a lateral constriction is introduced.

Previous experimental and numerical studies on non-flat beds have been completed (Yalin, 1971; Alfrink and van Rijm, 1983; Stansby and Zhou, 1998; Christian and Corney, 2004; Best and Kostachuk, 2002; Onitsuka et al., 2009). However, the non-flat beds used in these previous studies (generally trenches and dunes) are typically characterized by steeper slopes than that found in riffles, leading to flow separation at the expansion. The previous results also have not considered the wall effect, and

only consider the flow at the channel centerline. Pool-riffle sequences are not characterized by flow separation and scale with the channel width, and therefore, new studies must be completed to test these parameters.

To test the effect that bedforms have on shear stress in non-uniform flow in a pool-riffle sequence, MacVicar and Rennie (in review) conducted preliminary flume experiments using a single bedform configuration. They concluded that there are three phenomena that affect the shear stress on the bed. The first is the lateral convergence of mean flow and shear stress through a straight pool. The second is the flow deceleration at the upstream portion of the pool that causes the main flow to move away from the bed of the channel, which produces a vertical flow convergence near the water surface that matches the lateral convergence in the center of the channel. Lastly, the acceleration of the flow in the downstream portion causes the velocity to move more of the flow towards the bed, so that the near-bed velocity increases in the downstream portion of the pool as flow diverges across the width of the channel. MacVicar and Rennie (in review) concluded that the increase in near-bed velocity in the pool tail, the increase in turbulence in the pool head, and the flow convergence through the pool are all linked to convective acceleration and deceleration. They suggest that more research is needed to clarify the processes that occur in non-equilibrium transitions over multiple bedform geometries that are not characterized by flow separation as a means of better understanding flow over macrobedforms.

2.8 Thesis Objectives

The aim of this thesis is to better explain the effect that bedform scale has on the hydrodynamics of pool-riffle sequences. This thesis followed from the preliminary experiments of MacVicar and Rennie (in review), that tested the effect of a two-dimensional macro-scale bedform in an open channel on the three-dimensional structure of the flow. The specific objective of this thesis is to understand how the length and spacing of simplified bedforms affect the distribution of flow and turbulence in the channel, particularly, close to the channel bed or side walls where it could be significant for sediment transport. In the research described in this thesis, the geometry of straight artificial pools and riffle were implemented. Research was conducted using ultrasonic velocity profilers (UVPs) over movable PVC bedforms in a laboratory flume to allow multiple analyses on pool-riffle bedform ratios. This research was completed to try to identify the mechanism(s) that lead to the formation and maintenance of a riffle-pool in a simplified macro-scale bedform structure. Ultimately, this research will help to improve sustainable engineering design for the restoration of channelized rivers by improving our ability to manage sediment transport, maintain ecological integrity, and reduce the risk of flooding associated with pool-riffle sequences.

Chapter 3

METHODOLOGY

The following section outlines the experimental and analytical methods used in for this research including the experimental apparatus, the experimental runs, error detection and removal, and the analysis of the data.

3.1 Experimental Apparatus

3.1.1 Flume Description

The laboratory experiments were conducted in a 17 m long, 0.3 m deep, 0.6 m wide molded fiberglass flume (Figure 14), located at the Ven Te Chow Hydrosystems Laboratory in Urbana-Champaign, Illinois, USA.

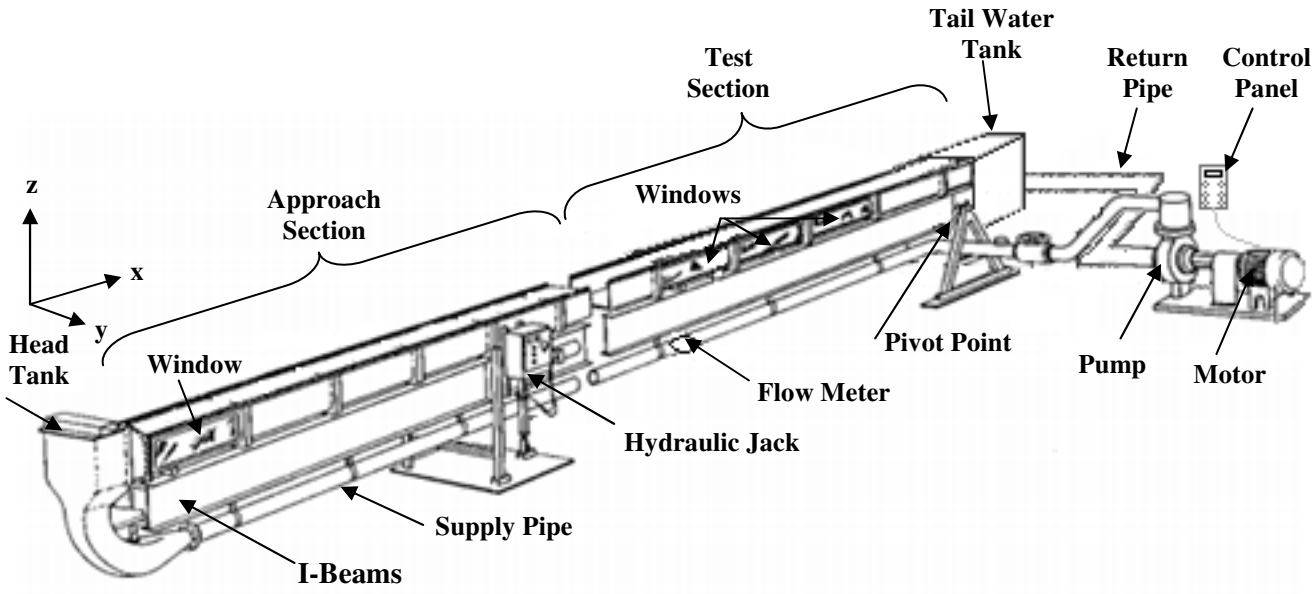

Figure 14. Sketch of the flume used in the experiments (Butman and Chapman, 1989).

The smooth-walled channel has plate glass windows at six locations in the middle of the raceway. The windows are 1.02 m long, by 270 mm high, by 6.3 mm thick, mounted flush to the sidewalls for minimal flow disturbance (Butman and Chapman, 1989). The flume is supported by two steel I-beams that pivot at the end of the flume. The slope is controlled by a hydraulic jack, and was set to a slope of

0.0016 m/m. Attached to the entrance of the flume channel is a head box that allows for a transition between turbulent incoming flow from the 152.4 mm (6 in) supply pipe to the uniform flow in the entrance region. The transition has an expanding and turning section to help minimize surface waves and secondary flow (Butman and Chapman, 1989). The water exits the transition at the level of the raceway where the water is driven down the raceway due to gravity (Butman and Chapman, 1989). The head box contains a weighted Styrofoam piece to help dampen surface waves (Figure 15b), and a flow straightener made out of an 18 by 10 matrix of 2.54 cm (1 in) PVC tubing that is approximately 0.43 m (1.4 ft) long (Figure 15c).

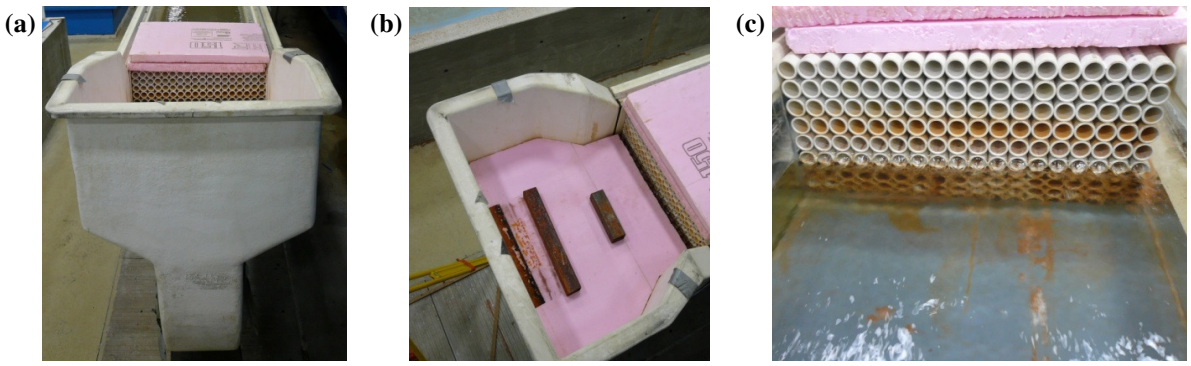

Figure 15. Picture of (a) the head tank, (b) the flow dampener within the head tank, and (c) the downstream view of the flow straightener.

At the end of the flume channel is a curtain style tail water control. For the purposes of this experiment, the tail water control was always wide open, and therefore, made no impact on the flow regime. Beyond the tail water control is the tail water tank which feeds the return line.

The flume uses a re-circulating water system controlled by an electric Aurora centrifugal pump. The pump is run by an electric motor controlled by a variable frequency drive controller, which allows a precise speed to be selected, ensuring test repeatability. The flow rate is measured with an ultrasonic Ultra-Mag flow meter, which has an accuracy of ±0.05% of the actual flow (McCrometer Inc., 2011). The flume raceway consists of two sections, the approach section and the test section. The approach section is six meters in length and consists of a flat bed which allows the flow to reach a uniform state before entering the test section. The test section, which follows the approach section, is eleven meters in length and contains the different bedforms.

On the top of the two sidewalls of the flume's raceway is a guiderail for an instrumentation cart. The cart is used to hold and transport different instrumentation up and down the length of the flume. The instrumentation cart ran on four wheels and has an adjustable upper frame to ensure it is level. The

instrumentation cart contains a lorry bracket which can slide along the width of the instrumentation cart.

An adjustable point gauge attached to the instrumentation cart's lorry bracket is used to measure the water and bed surface elevations (Figure 16). The water surface and bed heights were recorded at three locations across the flume, 0.04, 0.30, and 0.57 m (1.75, 11.75, and 22.25 in) from the near side wall, so that an average can be determined. The point gauge is accurate to ±0.0254 mm (0.001 in).

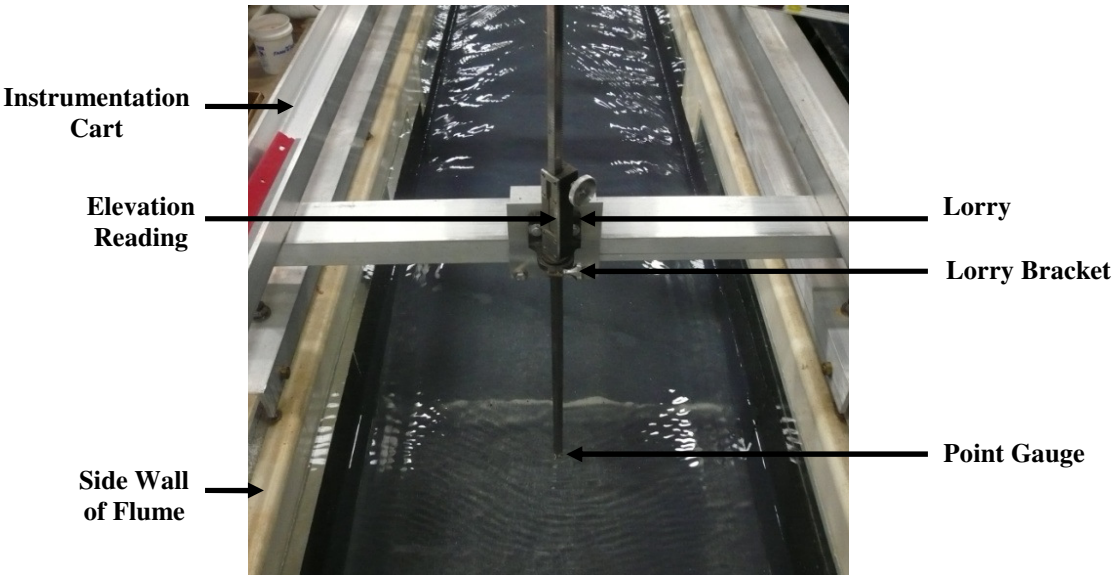

Figure 16. Measuring the water surface elevation with the point gauge at 0.30 m width.

3.1.2 Velocity Measurements

Velocity profiles were measured using 5 mm IMASONIC probes, with Optek Ultrasonic Velocity Profile (UVP) software Version 3.0, all coupled with a UVP-DUO data logger, as shown in Figure 17.

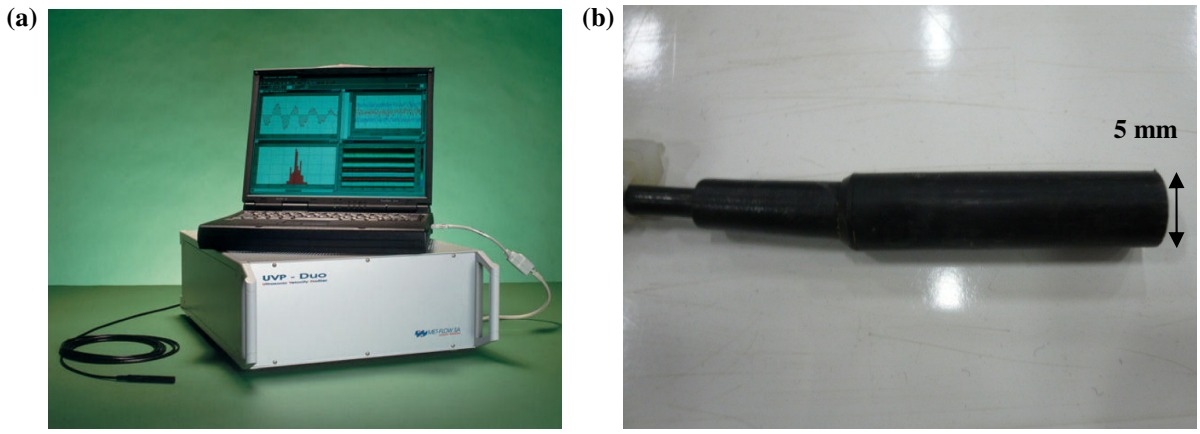

Figure 17. (a) UVP-DUO data logger and software (Met-Flow, 2002), and (b) an IMASONIC probe.

The UVP probe sends out a short ultrasonic pulse into the water column at a frequency of 4 MHz, and receives multiple echoes returning from the reflecting particles found along the acoustic path, which have velocity vectors at frequencies greater than 25 Hz (Met-Flow, 2002). The time delay (δt) between emissions of a pulse and reception of a corresponding echo from a region located a distance 'r' from the transducer is equal to:

$$\delta t = \frac{2r}{c} \tag{3}$$

where: c = speed of sound in the transmitting medium

The particles in the volume of water from which the sound is being scattered are moving with a radial velocity 'u_r' along the axis of sound transmission. Any backscatter sound will represent a Doppler shift of the frequency with respect to the original frequency when measured at the transducer (Met-Flow, 2002). Since the frequency is shifted twice, once when it hits the particle and again when it is reflected, the relation between the measured Doppler shift (F_D) and the velocity of the particle in the measuring volume is given by:

$$u_r = \frac{F_D \lambda}{2} \tag{4}$$

where: λ = wavelength of the ultrasound

The Doppler shift frequency is calculated by the UVP-DUO using a time domain algorithm for each channel. Since a Doppler-shifted echo burst from a channel is much shorter than the time corresponding to the required frequency measurement, several echoes are required to compute the shift frequency. From each echo a single sample of Doppler shift frequency is measured until the entire frequency is reconstructed (Met-Flow, 2002). The complete details of the Doppler shift determination can be found in the work of Lhermitte and Serafin (1984), and Lhermitte and Lemmin (1994).

Essentially, the UVP-DUO measures the Doppler shift and the time delay, and from them computes the component of the particle velocities inside the different measuring volumes.

The UVP probe can measure multiple positions along the transmission axis. The different positions along the axis were determined by the channel distance, and by selecting the total number of channels (Figure 18). The channel distance is a function of the speed of sound in water, and is set so that channel volumes never overlap. The number of channels selected depended on the water depth. The channel distance ranged from 1.43 to 1.47 mm depending on temperature of the water, and the number of channels ranged from 35 to 100, depending on the flow depth.

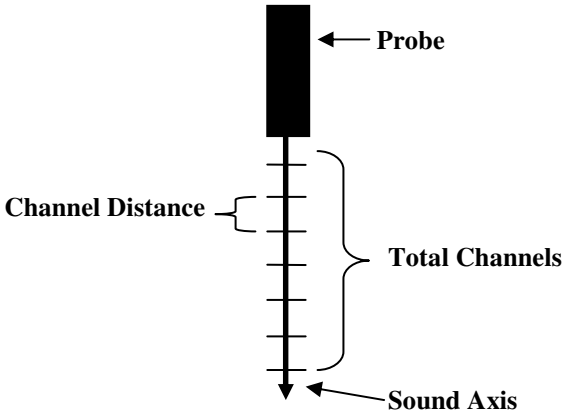

Figure 18. Sketch of the UVP probe sound axis, channel distance and total channels.

The UVP probes were set to have a sampling period of 25 ms (40 samples per second), and to measure the velocity over a time period of 120 s. With these parameters, each channel collected 4800 velocity samples in the two minutes of testing. The velocity sensitivity of the UVP probe depends on the velocity resolution, or the least resolvable difference in velocity, given by (Met-Flow, 2002):

$$V_{range} = \frac{C_s^2}{4 f_o P_{max}} \tag{5}$$

$$\Delta V = \frac{V_{range}}{N_{DU}} \tag{6}$$

where:
- V_{range} = maximum measurable velocity component range [m/s]
- C_s = speed of sound in water [m/s],
- f_o = ultrasound basic frequency [Hz]
- P_{max} = maximum depth [m]
- ΔV = velocity resolution [m/s]
- N_{DU} = number of Doppler units

The number of Doppler units represents the number of possible velocity values coming from the digital signal processer. Due to the fact that the UVP-DUO uses an 8-bit word, the number of bit combinations available in the digital signal processor is 256 values (Met-Flow, 2002). Using Equations 5 and 6 and the values of $f_o = 4$ MHz, $P_{max} = 0.06$ m, and $c = 1450$ m/s (which are values encountered in the testing phase), the least resolvable difference in velocity is estimated to be 0.009 m/s.

3.1.3 Water Temperature

The temperature of the water in the flume was subject to change with room temperature. This change in water temperature caused a change in the speed of the ultrasound transmitted by the UVP. In order to account for the differences in the speed, the water temperature was measured periodically throughout each run to calculate the speed of sound used in the UVP software calculations. The speed of sound in water at different temperatures is determined as (as per Table 2 in Lubbers and Graaff, 1998):

$$C_s = 1405.03 + 4.624(T_w) - 0.0383(T_w^2) \quad (7)$$

where: C_s = speed of sound in water [m/s]
T_w = temperature of water [°C]

3.1.4 Seeding

The UVP does not measure the velocity of the fluid, but of particles that are suspended in the fluid. Therefore, it is important to choose a seeding material that is compatible with water and the frequency at which the UVP is operating. It is recommended that the reflecting particles should have a diameter greater than a quarter of the wavelength (Met-Flow, 2002):

$$d_i > \frac{\lambda}{4} \quad (8)$$

where: d_i = diameter of reflecting particle [m]
λ = wavelength [m]

The wavelength is proportional to the velocity divided by the frequency of the emitted pulse (Met-Flow, 2002):

$$\lambda = \frac{C_s}{f} \quad (9)$$

where: f = frequency [Hz]

The UVP operated at a frequency of 4 MHz for all trials. The speed of sound at room temperature is 1480 m/s. Therefore, the wavelength emitted is 0.37 mm, and the reflecting particles should have a diameter greater than 93 µm. The density of water at room temperature is 1.0 g/mL, therefore, the reflecting particles should have a density of approximately 1.0 g/mL, and a diameter of approximately 93 µm.

Griltex A1 P82, a thermoplastic adhesive manufactured by EMS Griltech, was selected for use as seeding material for the experiment because it is approximately neutrally buoyant, with a density $\rho = 1.07$ g/mL, and has a diameter suitable for reliable reflectance of the emitted 4 MHz UVP signal (80 µm to 200 µm) (Met-Flow, 2002; Barrie, 2009). The seeding particles were added to the water at the start of each run, and periodically throughout the runs when the signal-to-noise ratio indicated a poor quality return.

3.2 Experimental Runs

3.2.1 Bedform Description

Simplified two-dimensional bedforms were utilized in this experiment, which meant that no lateral variability was modeled. No sediment was added to the flume so that all experiments were run on clear water. Modular PVC bedforms were set on the bottom of the raceway so that different bedform geometries could be tested. Bedforms were constructed as a series of shallow and deep sections connected by gradual transitions. The hydrodynamics over seven different bedform lengths were tested by changing the length of the shallow and deep sections (Table 2 and Figure 19).

Table 2. Details of the bedform geometries for each run.

Run	Total Bedform Length (m)	Shallow Section Length (m)	Deep Section Length (m)	Width / Total Length Ratio
1	1.82	0.40	0.40	3.0
2	2.22	0.40	0.80	3.7
3	3.02	0.40	1.60	5.0
4	3.82	0.40	2.40	6.4
5	4.22	0.80	2.40	7.0
6	5.02	1.60	2.40	8.4
7	5.82	2.40	2.40	9.7

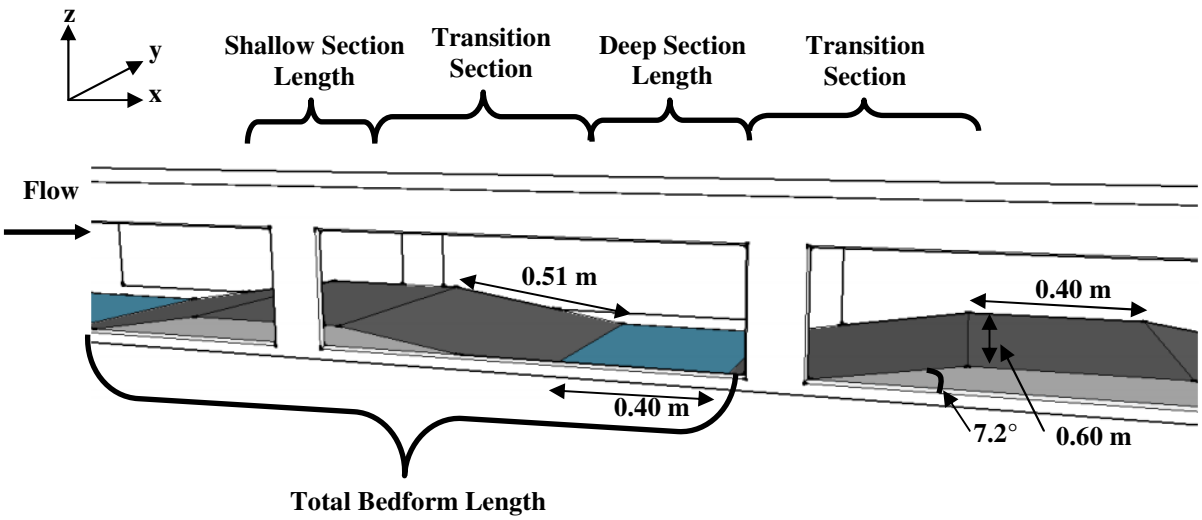

Figure 19. Sketch of flume with bedforms.

The ratio between channel width and total bedform length ranges from 3 to almost 10 (Table 2), which sufficiently covers the expected scale of 5 to 7 channel widths naturally observed in pool-riffle sequences.

The transition sections were angled at 7.2° from horizontal over a streamwise distance of 0.50 m, giving a change in height of 0.06 m, and a bed slope length of 0.51 m. This slope ensures that permanent flow separation does not occur (Simpson, 1989), and is in the range of typical leeside angles in macrobedforms (Best and Kostaschuk, 2002; Carling et al, 2000). This slope is similar to MacVicar and Rennie's (in review) flume experiments (5°), and based on MacVicar and Roy's (2007a,b) field study of a forced pool-riffle.

The velocity was measured over the first bedform in the series for all runs. The measurement section began 0.20 m upstream of the transition to the first bedform and continued 0.5 m downstream of the first pool. Downstream of the testing area consisted of a 0.40 m length shallow depth and another transition section down to a flat bed.

The bedforms were affixed to the side walls using a 100% silicone rubber sealant. This silicone was also used in between modular bedform sections to help reduce any secondary currents that may have been unintentionally created. When changing between different bedform configurations, the silicone was removed from side wall as best as possible, however, there were still remnants of silicone on the side walls and windows. This small layer of silicone on the side walls was assumed to be insignificant, and the walls of the flume were still assumed to be smooth.

3.2.2 Probe Positioning

Data was collected from three orientations to provide data for two-dimensional velocity volumes. These orientations were measured on the vertical profile at 0°, -30°, and 30°, which are referred to as vertical, upstream, and downstream orientations, respectively (Figure 20). Lateral data was also collected through the clear windows where possible using the probes along with Spectra 360 Electrode Gel (ultrasound jelly) as a medium. However, this data is incomplete due to the limited windows along the flume, and has proven difficult to analyze due to additional noise related to the reflectance of the ultrasound pulse within the windows, so it is not included.

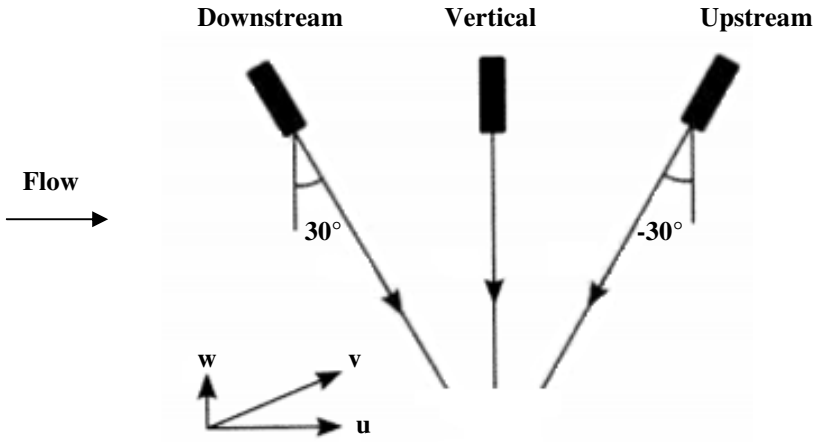

Figure 20. Probe orientations used in the experiments.

Each of the orientations used four UVP probes spaced 95 mm apart starting at 15 mm away from the inside wall of the raceway. This spacing allowed for the fourth probe to be placed at 300 mm, or at exactly half of the flume's width. Analysis was completed using data from only one half of the flume width based on the assumption that the flow is symmetric about the center axis of the flume. In order to obtain a higher spatial density of data in the transition to the deep section, additional measurements were taken by moving the probes to 66 mm from the inside wall.

The probes were held in plastic probe holders and fixed with set screws. These plastic holders had milled holes at set angles to allow for the three orientation angles. The probe holders were attached to an aluminum brace that was in turn attached to an adjustable point gauge, which was fixed to the instrumentation cart. The apparatus was designed to minimize the possibility for positioning errors. The aluminum brace was leveled and squared to the flume wall at each position prior to velocity measurements. The probes were positioned so the tips of the probes were completely submerged in the water (Figure 21).

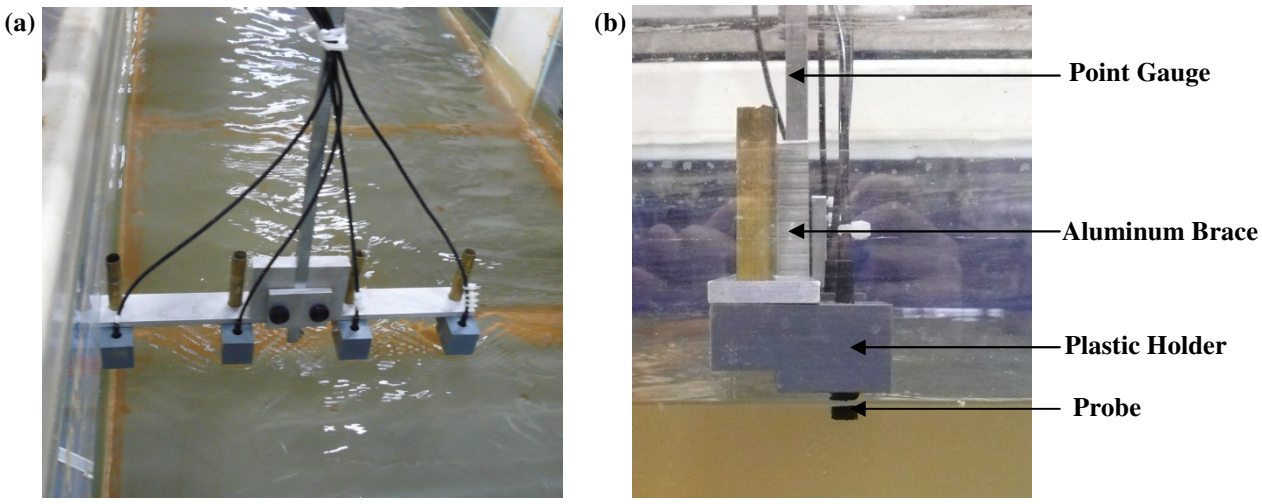

Figure 21. Measurement apparatus (a) looking downstream, and (b) looking from the side.

The probes were moved in 153 mm (0.5 ft) increments downstream for each test. The exceptions were Runs 4, 5, 6, and 7, where the probes were moved in 305 mm (1ft) increments through the deep section (Figure 22).

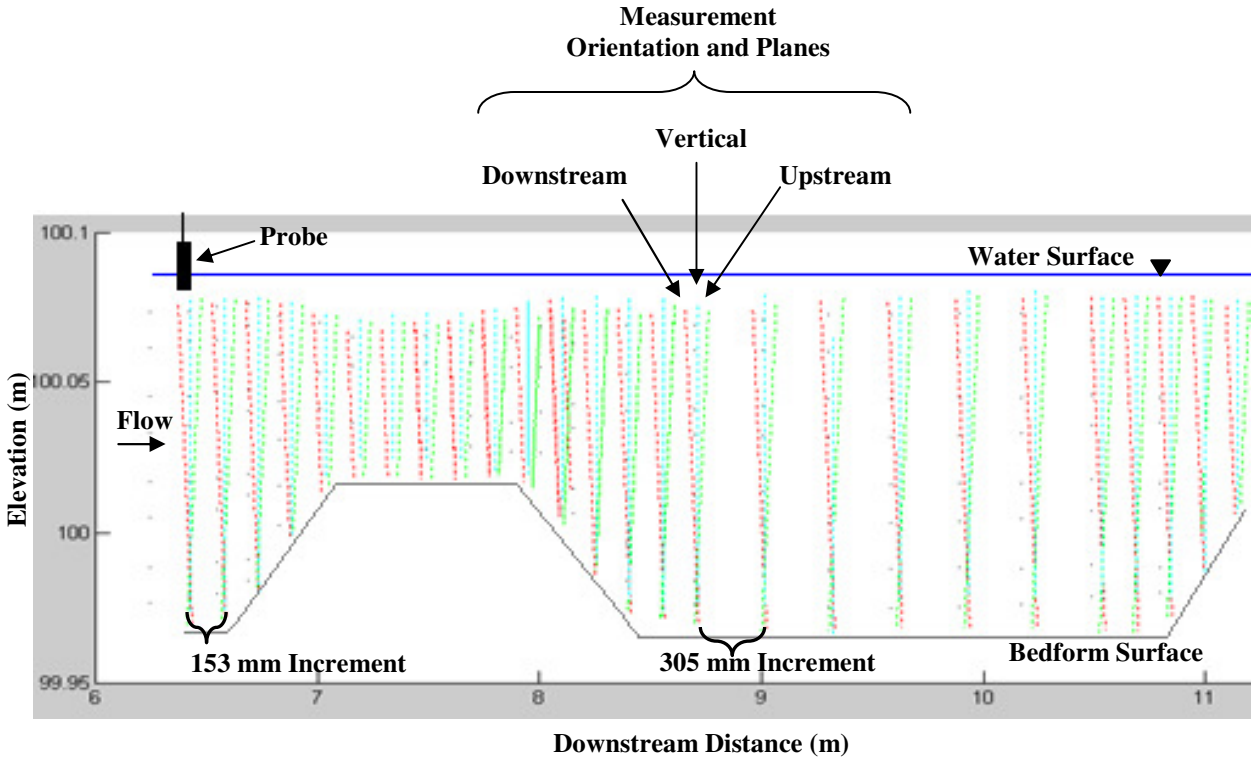

Figure 22. Sketch of Run 5's probes measurement planes and probe increment movements downstream from the side view.

At each measurement location, the point gauge and cart position were recorded. The point gauge provided the vertical location of the probes. The cart position allowed the calculation of the streamwise position of the probes by using the geometric relationships between the cart, the point gauge, the aluminum brace, and the plastic holder, to the center of the probe. The horizontal position of the probes was noted, but was predetermined to be at either the 15 mm or 66 mm away from the inside flume wall.

3.2.3 Water Depth and Discharge

The flow rate was held constant at 15.4 L/s and the depth of the water upstream of the bedforms was kept at a constant 120 mm in all runs. With these inlet conditions, the bulk velocity was 0.21 m/s in the approach section, and the water depth in the deep and shallow sections was approximately 120 mm and 60 mm, respectively, for all bedform configurations. The purpose for these conditions was to keep the water depth in the pool twice as deep as the water in the riffle, which was similar to MacVicar and Rennie's (in review) flume experiments based on MacVicar and Roy's (2007a,b) field study. This water depth maintained a width to depth ratio of 1:10 in the shallow section, and a 1:5 ratio in the deep section, which is sufficiently wide so that a velocity dip is not expected at the channel centerline. The bulk velocity was higher than the previous studies conducted by MacVicar and Roy (2007a, b), but was decided upon primarily because it was sufficient in keeping the seeding material in suspension, which is necessary in order to obtain high quality data using the UVPs.

3.2.4 Froude and Reynolds Numbers

The Froude number relates inertial forces to gravitational forces, and represents the effect that gravity has on the state of flow in open channels (Dingman, 2009), and is defined as:

$$\mathrm{Fr} = \frac{\bar{u}}{\sqrt{gd}} \tag{10}$$

where: Fr = Froude number
$\bar{u}$ = average streamwise velocity [m/s]
g = gravitational acceleration [9.81 m/s^2]
d = total water depth [m]

In this experiment, it was important that the Froude number always indicated subcritical flow, which occurs when Fr < 1. This was important so as to not introduce a hydraulic jump, and so that the Froude number was similar to previous field and lab studies that this experiment was based upon. A hydraulic jump is the rise of the water surface level that takes place due to the transformation of supercritical flow to subcritical flow (Dingman, 2009).

The Reynolds number relates inertial forces to viscous forces, and is used to determine whether a flow is laminar or turbulent, and is defined as:

$$\mathrm{Re} = \frac{\bar{u} * d * \rho}{\mu} \tag{11}$$

where: Re = Reynolds number

ρ = water density [1000 kg/m^3]

μ = kinematic viscosity [0.01 m^2/s]

In this experiment, it was important that the Reynolds number indicated turbulent flow on the same order of magnitude as previous field studies in order to have similar flow conditions. Table 3 shows the maximum Reynolds and Froude numbers from all experimental runs and values from previous field and lab studies. A spatial distribution of the Froude and Reynolds numbers can be seen in Appendix A and Appendix B, respectively.

Table 3. Comparison of the maximum Froude and Reynolds number from Runs 1 through 7 versus previous field and lab studies.

Study	Max Fr	Max Re
Run 1	0.60	3.2E+04
Run 2	0.57	3.0E+04
Run 3	0.61	3.2E+04
Run 4	0.60	3.1E+04
Run 5	0.64	3.0E+04
Run 6	0.67	3.2E+04
Run 7	0.72	3.3E+04
MacVicar and Rennie (in review)	0.27	7.5E+04
MacVicar and Roy (2007a)	0.59	7.8E+05

The Froude values created in the experiment are much higher than the lab study completed by MacVicar and Rennie (in review), but relatively close to the values from the field study conducted by MacVicar and Roy (2007a). The Reynolds numbers tested in this experiment are lower than the lab and field studies, however, they are on the same order of magnitude, and are in the fully turbulent regime.

3.2.5 Uniform Flow and Repeatability

In order to ensure that the flow was uniform after the 6 m approach section, and to show that the tests were repeatable, the velocities at the end of the approach section was measured in each run for all orientations. If the flow was uniform, the velocity profiles in each run should follow the same trend, and if the tests were repeatable and the upstream conditions were held the same, the profiles should be of similar magnitudes. The velocity data from the specific probe orientations were utilized to create the velocity profiles. For the upstream, vertical, and downstream orientations, the velocity profiles, magnitudes, and trends are very similar in each run, indicating uniform flow and repeatability of the velocity measurements (Figure 23).

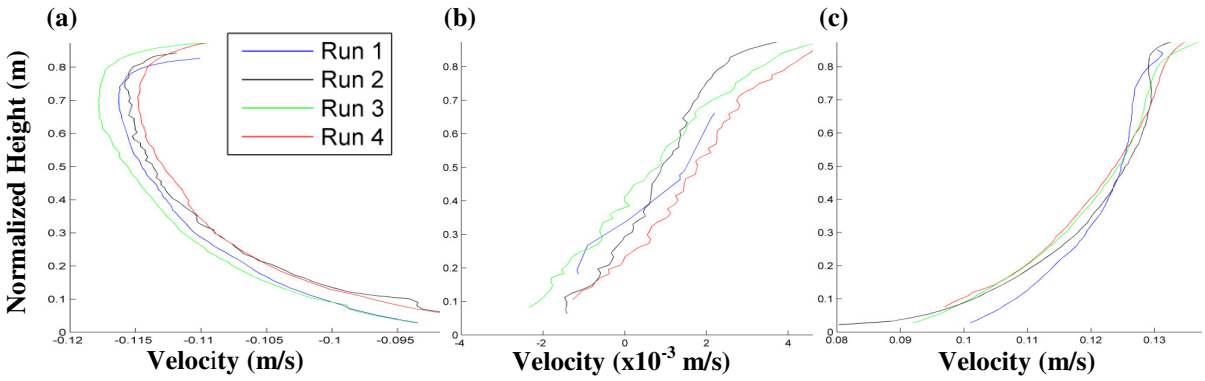

Figure 23. Centerline uniform flow profiles along the axis of the probe in the (a) upstream, (b) vertical, and (c) downstream orientations.

It should be noted that the vertical radial velocities are at least two orders of magnitude smaller than the upstream and downstream radial velocities, which is why there is more variation in these measurements, as the velocity is nearing the lower limit of the measurement resolution. The vertical velocity is more variable than the streamwise velocity due to the sensitivity of the probes.

3.3 Analysis

The analysis of the raw data is a complicated and extensive procedure comprised of a series of error analysis and calculation steps (Figure 24).

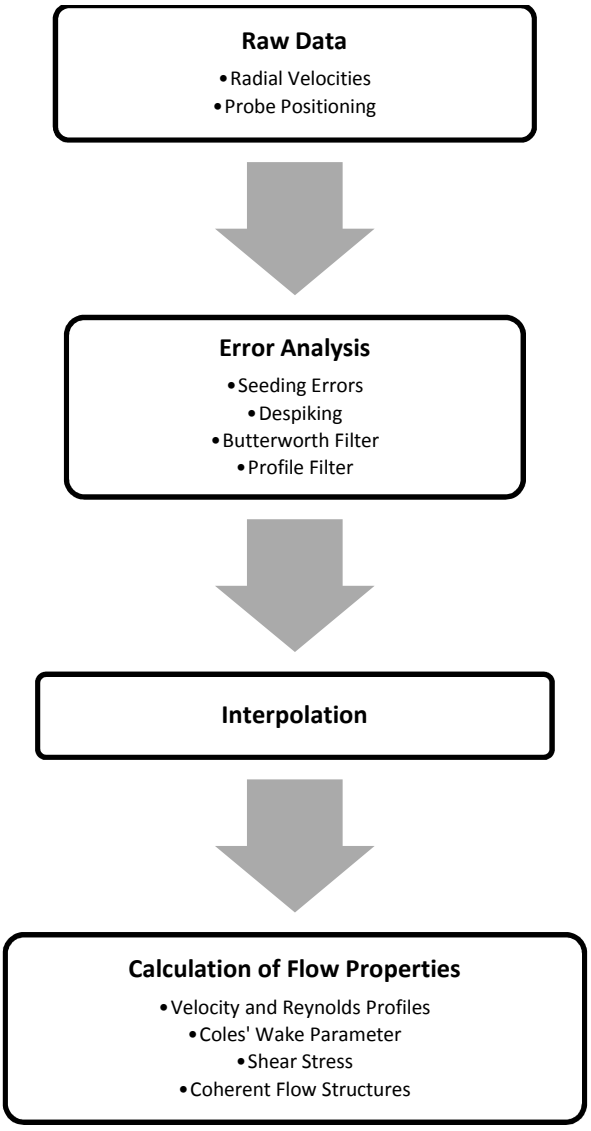

Figure 24. Flow chart of the data analysis.

The analysis process is explained in detail, starting from the raw data, moving on to the results of the error analysis, through the interpolation process, and concluding with the calculation of different flow properties used in the results of this thesis.

3.3.1 Raw Data

As stated in Section 3.1.2, the UVP probes were set to have a sampling period of 25 ms, so each channel collected 4800 samples of raw data in the two minutes of testing. The raw data of the velocity measurements were then stored as an MPROF file format, which is a unique format specifically programmed for the UVP Optec software. The raw data collected included the time delay, Doppler shift frequency, channel distance, and channel width, plus numerous other variables. The raw data was

then converted by the software into a beam velocity in the direction of the probe for each channel based upon the time delay and Doppler shift frequency. The average and range of the velocity data for each channel in the profile was provided in a summary to the user at the end of each testing period (Figure 25).

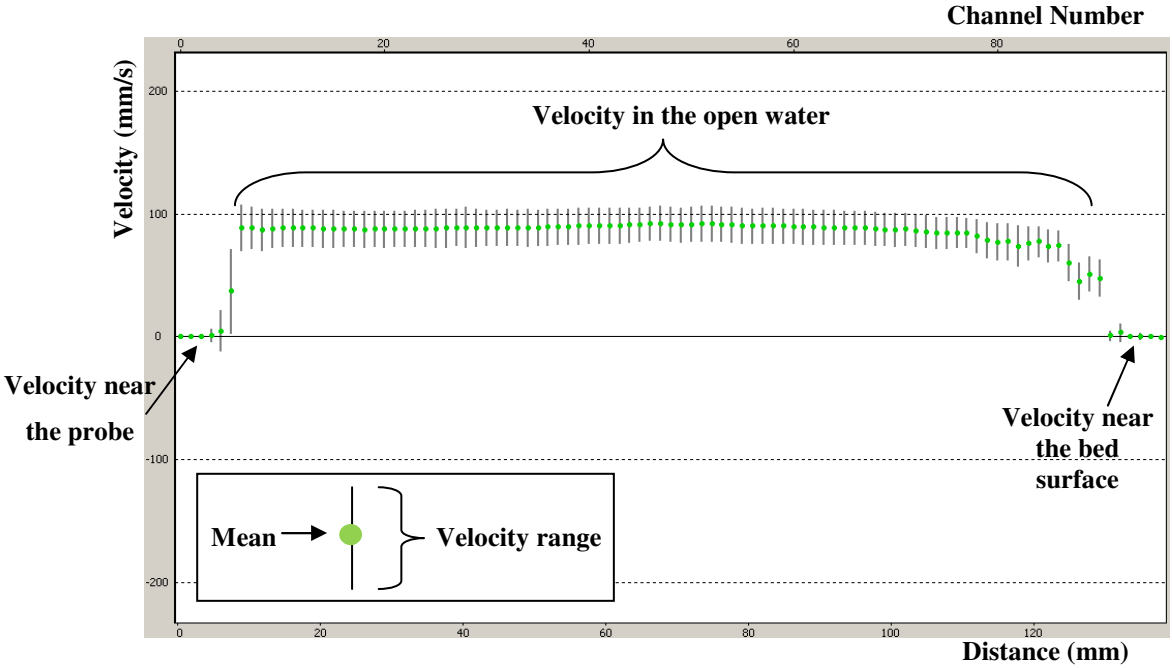

Figure 25. Average and range of the raw radial velocity data in a MPROF file from the downstream orientation.

Further analysis of the raw data must be conducted to determine downstream velocity, but before this occurs, the data is analyzed for errors.

3.3.2 Error Analysis

Errors that can occur in the UVP measurements include, but are not limited to, the computation of the Doppler shift (Pedocchi and Garcia, 2009; Goring and Nikora, 2002), the random motion of the velocity inside the sampling volume (Pedocchi and Garcia, 2009), and a lack of data points due to insufficient seeding. These errors will result in white noise, wrapping errors, and spikes, and some of the erroneous data will look similar to the natural fluctuations in the velocity (Nikora and Goring, 2002). To remove erroneous data points and identify data series with significant error that could not be removed, the data was filtered for spikes, white noise, and wrapping errors.

3.3.2.1 Seeding Error Filter

One error that occurred in Run 2's upstream orientated data only was a wrapping error caused by insufficient seeding material. This error led to an increase in near zero values caused by no data, which led to an increase in standard deviation and resulted in a mean velocity closer to zero in comparison with other runs (Figure 26).

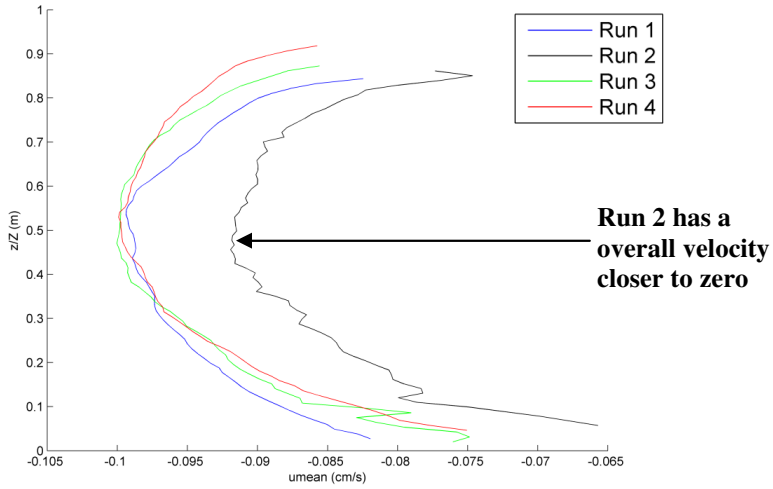

Figure 26. Velocity profiles at 6.4 m in the upstream orientation from Run 1 through 4.

This error was remedied by creating a de-wrapping program in MATLAB, which was only applied to Run 2's upstream data before it was sent to the subsequent filters. Because this type of error resulted in data that was closer to zero than the mode, a secondary mode of data appeared in the histogram (Figure 27).

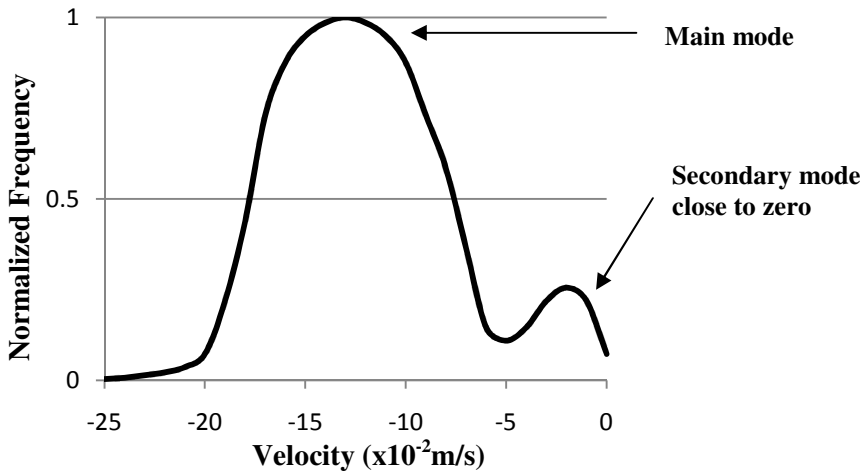

Figure 27. Example of a histogram from Run 2's upstream data.

To eliminate this data, an estimate of the standard deviation of the main mode was calculated from the data that was farther from zero than the secondary mode. Assuming all of the data should follow a single distribution, likely error points were determined as those that had a z score greater than 6, which is equivalent to the 99.9999999th percentile of the data. Such an extreme value was found to be necessary to prevent the misclassification of good data where data was strongly negatively skewed, which was the case in some locations due to shear layers. The bad data was then replaced with an interpolated value from the surrounding good data points. Data series with greater than 5% seeding error were removed from further analysis. Of the approximately 32 million total data points in Run 2's upstream orientation data, this source of error affected only 2.52% of the data.

3.3.2.2 Single Point Error Filtering

Each channel within a probe's profile collects 4800 velocity readings during the 120 seconds of testing. A normal velocity signal will have natural fluctuations attributed to it, but it can also have erroneous fluctuations known as spikes (Figure 28).

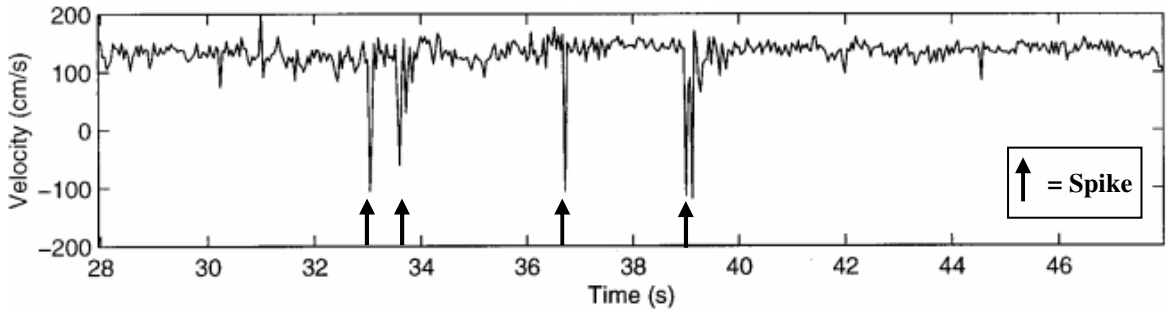

Figure 28. Example of spikes in a velocity time series.

These spikes occur for a variety of different reasons, as discussed previously. The spikes may account for a small percentage of the data, but will have large impacts on the data quality and statistics, and therefore they need to be identified and replaced by a more probable data point. Single point error filtering was conducted on every time series for better quality data. If a time series was identified to have more than 5% spikes attributed to it, it was classified as bad data and was completely disregarded. If less than 5% of the data was identified as spikes, the spikes were replaced with an interpolated value from the surrounding good data. Spikes were identified using the Goring and Nikora (2002) filter algorithm. The method is based on the assumption that good data cluster in a dense cloud in a three-dimensional ellipsoid formed by the velocity and its first and second derivatives (Figure 29).

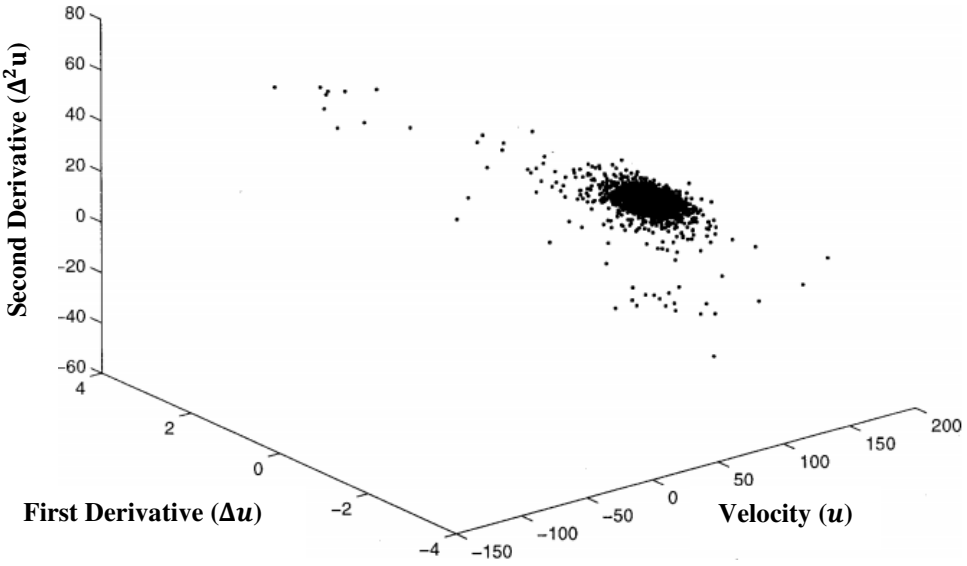

Figure 29. Example of a three-dimensional cluster of good data when the velocity and its first and second derivatives are plotted against each other (Goring and Nikora, 2002).

Following the work of Goring and Nikora (2002), detrended velocity series were calculated by removing the mean and long-period fluctuations from the raw data using a high-pass filter. These were added back in after despiking. Surrogates of the velocity were calculated for the first and second derivative as:

$$\Delta u_i = (u_{i+1} - u_{i-1})/2 \tag{12}$$

$$\Delta^2 u_i = (\Delta u_{i+1} - \Delta u_{i-1})/2 \tag{13}$$

where: u_i = detrended velocity series

Δu_i = surrogate for first derivative of the detrended velocity series

$\Delta^2 u_i$ = surrogate for second derivative of the detrended velocity series

To calculate the surrogates, the velocity is not divided by the time step, so the velocity's order of magnitude does not differ from that of the second derivative, which removes and the possibility of complex solutions to Equations 12 and 13 (Goring and Nikora, 2002). The theoretical maximum velocity threshold from the detrended data series and the first and second derivative surrogates were then calculated, as:

$$\lambda_U = \sqrt{2\ln(n)}\,\hat{\sigma} \tag{14}$$

where: λ_U = maximum velocity threshold

n = length of the raw data series

$\hat{\sigma}$ = standard deviation

The rotation angle (θ) of the principal axis ($\Delta^2 u_i$ versus u_i) of the ellipsoid was determined using the filtered velocity and the surrogate's second derivative, as:

$$\theta = \tan^{-1}\left(\sum(u_i \Delta^2 u_i) \Big/ \left(\sum u_i^2\right)\right) \tag{15}$$

Once the rotation angle of the principal axis is determined, the three ellipses can be determined using the three pairs of variables shown in Table 4.

Table 4. Pair of major and minor axis standard deviation variables.

Major Axis Standard Deviation (α)	**Minor Axis Standard Deviation (β)**
$\hat{\sigma}_{u_i}$	$\hat{\sigma}_{\Delta u_i}$
$\hat{\sigma}_{u_i}$	$\hat{\sigma}_{\Delta^2 u_i}$
$\hat{\sigma}_{\Delta u_i}$	$\hat{\sigma}_{\Delta^2 u_i}$

The major and minor axes, respectively, of the three ellipses are the ellipsoid geometry solutions of:

$$(\lambda_U \alpha)^2 = a^2 cos^2\theta + b^2 sin^2\theta \tag{16}$$

$$(\lambda_U \beta)^2 = a^2 sin^2\theta + b^2 cos^2\theta \tag{17}$$

where: a = major axis
b = minor axis

As an example, for $\Delta^2 u_i$ versus u_i, the major axis is $\lambda_U \hat{\sigma}_u$, and the minor axis is $\lambda_U \hat{\sigma}_{\Delta_u^2}$. Each radial velocity data point is then checked to determine if they lie within the created ellipse (Figure 30). If a data point is identified as falling outside the ellipse, it was considered to be a spike, and was replaced with an interpolated value from the surrounding good data points. If the data series had greater than 5% spike replacement, the series was considered poor quality, and was removed from further analysis.

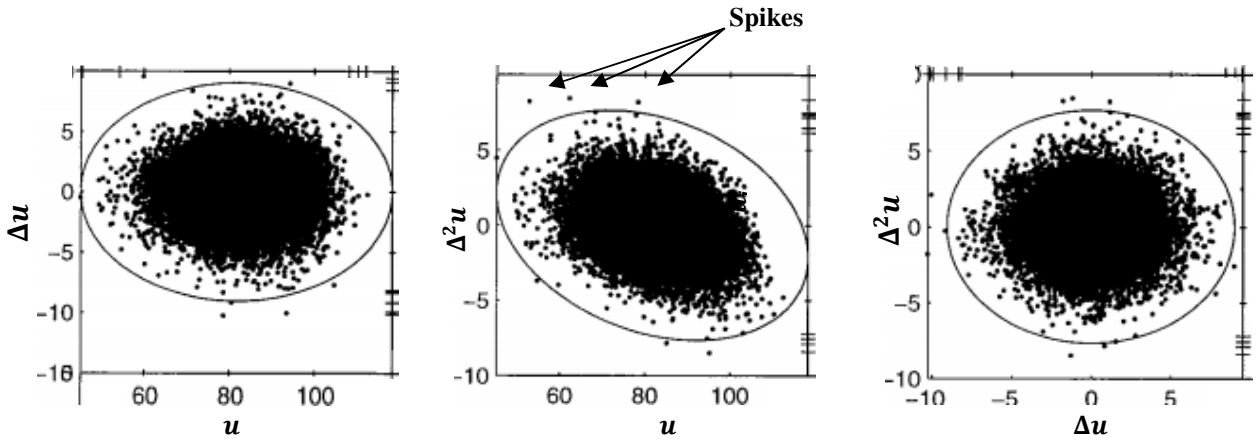

Figure 30. Example of calculated ellipsoid surrounding good data for different pairs of variables (Goring and Nikora, 2002).

3.3.2.3 Butterworth (Low Pass) Filtering

The UVP transducer sends out a set frequency and receives a wide range of frequencies back in response. The high frequency data returned has a low output signal amplitude versus input frequency relationship (M(f)), which indicates that the return signal is due to noise and not due to the velocity of a fluid element. A frequency filter can be used to remove undesirable frequency information from a signal. A low-pass filter, or a Butterworth filter, allows frequencies below a cutoff frequency to pass while blocking the frequencies above the cutoff frequency (f_c). A sharp cutoff of an ideal filter cannot occur in a practical filter, as all filter's response curves will contain a transition band over which the magnitude ratio decreases relative to the frequency. The slope of the transition band will depend on which order of exponential filter (k) is selected (Figure 31).

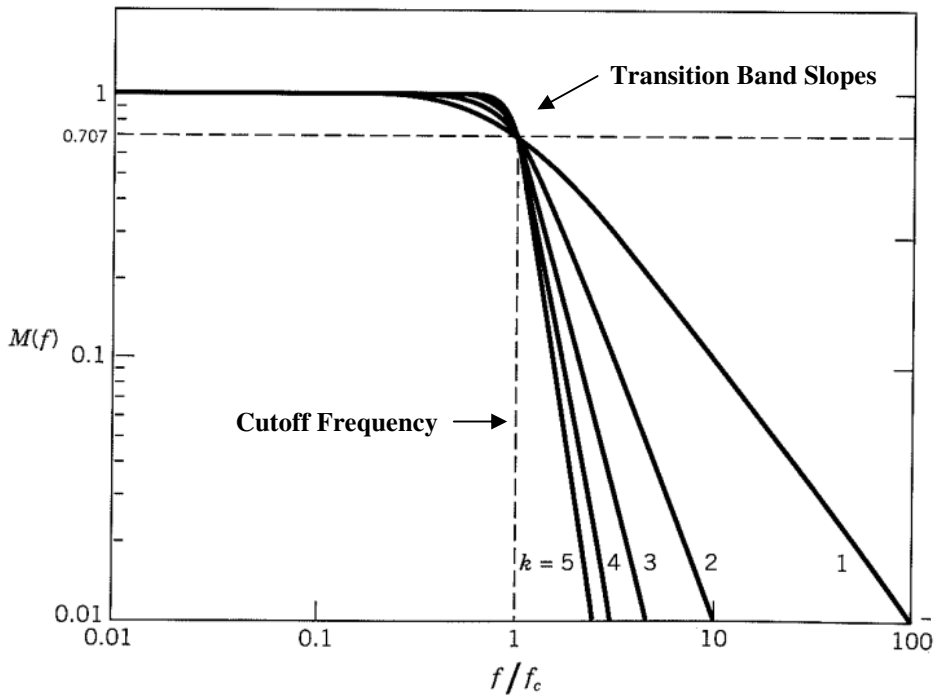

Figure 31. Frequency response function versus normalized frequency showing different orders of exponential filters (Figliola and Beasley, 2006).

The high frequency data of each beam velocity series was filtered using a third order Butterworth filter, where the cutoff frequency was calculated using the Nyquist frequency (Roy et al., 1997). The Nyquist frequency (f_N) is half of the sampling frequency (f_D) of a discrete signal, and it used in order to have an unbiased reconstruction of the signal (Roy et al., 1997; Met-Flow, 2002). No useful information above the Nyquist frequency can be obtained. The Nyquist frequency is defined as:

$$f_N = \frac{f_D}{2} \tag{18}$$

The half-power frequency (f_{50}) for a third order Butterworth filter was based on Table 1 from Roy et al. (1997), and is defined as:

$$f_{50} = \frac{f_D}{2.93} \tag{19}$$

The cutoff frequency used in the Butterworth filter was calculated using:

$$f_c = \frac{f_{50}}{f_N} \tag{20}$$

3.3.2.4 Profile Filtering

After the above filters had been achieved on the individual raw data series, the filtered velocity profiles were then filtered using statistical calculations. This was necessary because of poor data located close to the probe and channel bed, and due to a reflectance problem, where some data in the middle of the profile was poor. The profile filtering was accomplished by fitting an algorithm to the mean velocity, standard deviation, and skewness data using a third order polynomial equation. If the data fell outside the polynomial fit by having values less than in the 99th percentile of the cumulative normal probability, the data was considered to be an outlier and was removed from further analysis (Figure 32).

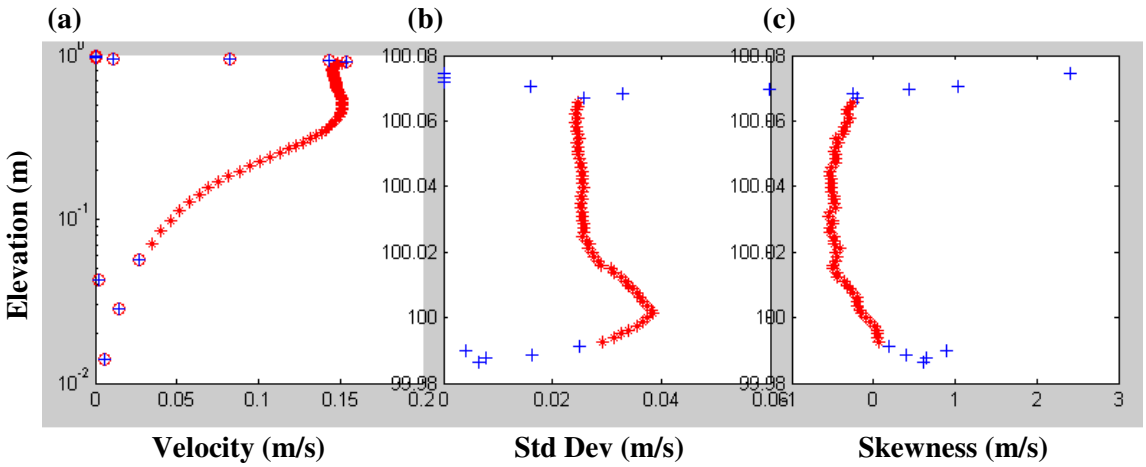

Figure 32. Statistical filtering of the velocity profile using (a) mean velocity, (b) standard deviation, and (c) skewness, where: red = good data, blue = bad data, blue with red circle = touching bed or water surface.

3.3.2.5 Error Results

The overall effect of the wrapping, spikes, and profile filtering was assessed by calculating the number of channels removed from further analysis per probe orientation in each run (Table 5). The total error for each run ranges from 2.8 to 6.1%, which is considered to be within acceptable limits. The vertical orientation had higher error due to reflectance issues from the bed, and the main issues in the upstream and downstream orientations occurred during the transition sections due to the complex nature of the flow.

Table 5. Error based on each probe orientation for Runs 1 through 7.

Run	Upstream			Downstream			Vertical			Total Error
	Bad Channels	Total Channels	Error	Bad Channels	Total Channels	Error	Bad Channels	Total Channels	Error	
1	64	4116	1.6%	151	4185	3.6%	112	3280	3.4%	2.8%
2	269	5344	5.0%	86	5767	1.5%	394	5061	7.8%	4.6%
3	339	7148	4.7%	170	7044	2.4%	472	6332	7.5%	4.8%
4	319	6908	4.6%	349	6705	5.2%	612	7788	7.9%	6.0%
5	389	8206	4.7%	388	7696	5.0%	603	6798	8.9%	6.1%
6	406	8174	5.0%	385	8258	4.7%	262	7057	3.7%	4.5%
7	440	8401	5.2%	323	8201	3.9%	496	7042	7.0%	5.3%

3.3.3 Interpolation

Beam velocity measurements were taken every 153 mm or 305 mm (0.5 ft to 1 ft) down the flume's raceway, and data from all orientations was only available in locations were beam velocities intersected (Figure 22). Therefore, it was necessary to estimates beam velocities by interpolation on an orthogonal grid using a program written in MATLAB. The interpolation was completed using a grid spacing of 0.01, 0.02, and 0.05 in the x, y, and z directions, respectively, and used a linear interpolation method. This grid spacing created a 101 x 11 x 51 three dimensional matrix of the beam velocity components treating the entire flume measurements as one volume.

The interpolation process was also completed treating the entire flume as four different consecutive volumes that corresponded with the change in bed slope. In this case, the grid spacing was 0.025, 0.05, 0.005 in the x, y, and z directions, respectively. This grid spacing created a 41 x 11 x 201 three dimensional matrix of the beam velocity components for each volume.

3.3.4 Calculation of Flow Properties

The analysis up to this point has been based on the velocity in the probe's radial orientation. Now that the raw data has been filtered for errors, and interpolated across a grid of the flume, it is possible to calculate the orthogonal components of velocity (u, w), and the Reynolds stresses ($\overline{u'w'}$).

3.3.4.1 Calculation of Velocity and Reynolds Stress

The UVP probes were orientated as shown in Figure 33, where α is the angle from the vertical, and u_{r1}, u_{r2}, and u_{r3} are the instantaneous radial velocities.

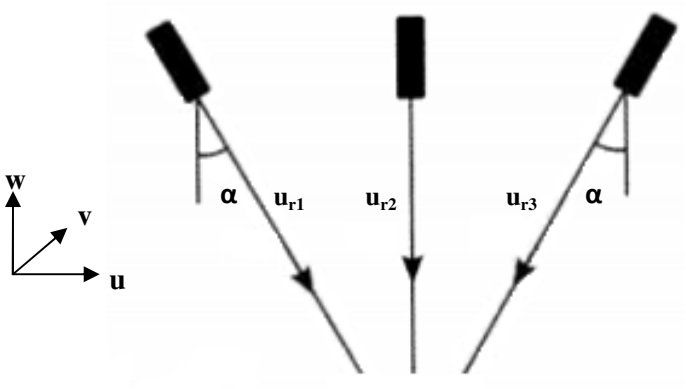

Figure 33. UVP probe orientations and radial velocity components (Pedocchi and Garcia, 2009).

From geometry, the radial velocities, u_{r1}, u_{r2}, and u_{r3} are a function of the horizontal (u_i) and vertical (w_i) velocities at each point along the sound path, as:

$$u_{r1} = u_1 \sin\alpha - w_1 \cos\alpha \tag{21}$$

$$u_{r2} = -w_2 \tag{22}$$

$$u_{r3} = -u_3 \sin\alpha - w_3 \cos\alpha \tag{23}$$

Adding and subtracting Equations 21 and 23 yields:

$$u_{r1} + u_{r3} = (u_1 - u_3)\, sin\,\alpha - (w_1 + w_3)\, cos\,\alpha \tag{24}$$

$$u_{r1} - u_{r3} = (u_1 + u_3)\, sin\,\alpha - (w_1 - w_3)\, cos\,\alpha \tag{25}$$

Averaging over several points and assuming the flow is statistically uniform (i.e. $\overline{u_1} = \overline{u_3} = \bar{u}$ and $\overline{v_1} = \overline{v_3} = \bar{v}$), the average velocity components in the streamwise ($\bar{u}$) and vertical ($\bar{w}$) direction can be expressed as:

$$\bar{u} = \frac{\overline{u_{r1}} - \overline{u_{r3}}}{2\sin\alpha} \tag{26}$$

$$\bar{w} = -\frac{\overline{u_{r1}} + \overline{u_{r3}}}{2\cos\alpha} \tag{27}$$

$$\bar{w} = -\overline{u_{r2}} \tag{28}$$

Equation 28, which calculates the vertical velocity directly from the vertical probe, gives more appropriate results, as it does not enhance the vertical velocity errors by analytical manipulation. Therefore, Equation 28 was utilized for the presentation of the vertical velocity results.

The Reynolds stress (τ_{Re}) was calculated using the deviation from the streamwise velocity ($\bar{u}'$), and the deviation from the vertical velocity ($\overline{w}'$), as:

$$\tau_{Re} = -\rho\overline{u'w'} = 1000\left(\frac{u_{r3}'^2}{2sin^2\alpha}\right) \tag{29}$$

In general, the Reynolds stress is approximately equal to the total shear stress in a flat bed. However, with the introduction of bedforms, the total shear stress must be calculated through different methods based on the velocity profile and the Reynolds stress profile.

3.3.4.2 Calculations from Profiles

Velocity profiles describe the variation of velocity with distance from the bed surface. The distance from the bed (z) was normalized by the water depth (d) as:

$$z/Z = \frac{z}{d} \tag{30}$$

where: z/Z = normalized water depth [m/m]

The inner region (z/Z = 0 to 0.20) of a uniform flow velocity profile in an open channel can be expressed by the log law (Nezu and Nakagawa, 1993; Onitsuka, et al., 2009), as:

$$\frac{\bar{u}}{u^*} = \frac{1}{\kappa}\ln\left(\frac{zu^*}{\mu}\right) + C \tag{31}$$

where: $\bar{u}$ = point velocity [m/s]
z = height above the bed [m]
z_o = reference bed level [m]
u^* = shear velocity [m/s]
κ = von Karman constant [~0.4]
C = constant of integration, where C = 0 for a rough bed and ~ 5 for a smooth bed

The outer region (z/Z = 0.2 to 1) of the velocity profile can be expressed by the Coles' wake law (Coles, 1956; Song and Chiew, 2001; Onitsuka et al., 2009), as:

$$\frac{\bar{u}}{u^*} = \frac{1}{\kappa}\ln\left(\frac{zu^*}{\mu}\right) + C + \frac{2\Pi}{\kappa}\sin^2\left(\frac{\pi}{2}\frac{z}{z_c}\right) \tag{32}$$

where: z_c = height above the bed at which the maximum velocity occurs [m]

Π = Coles' wake parameter

u^* = shear velocity [m/s]

z_o = reference bed elevation of the shear velocity [m]

The Coles' wake parameter is defined as the deviation of a velocity profile from the log law of uniform flow (Figure 34), and indicates the wake-strength in the outer region of the turbulent velocity profile (Song and Chiew, 2001). In uniform flow in wide channels where the width to depth ratio is greater than 5, Π is equal to zero because there are no inertial effects in the outer layer, and the velocity distribution will follow a straight line in a log-linear plot (Coles, 1956). Coles (1956) showed that Π will be greater than zero during convective deceleration due to the relatively high inertia in the outer zone, which is when the near surface velocities are relatively high. He also showed that Π will be less than zero during convective acceleration, as the flow will have relatively low inertia in the outer zone, while the near-bed velocities are relatively high.

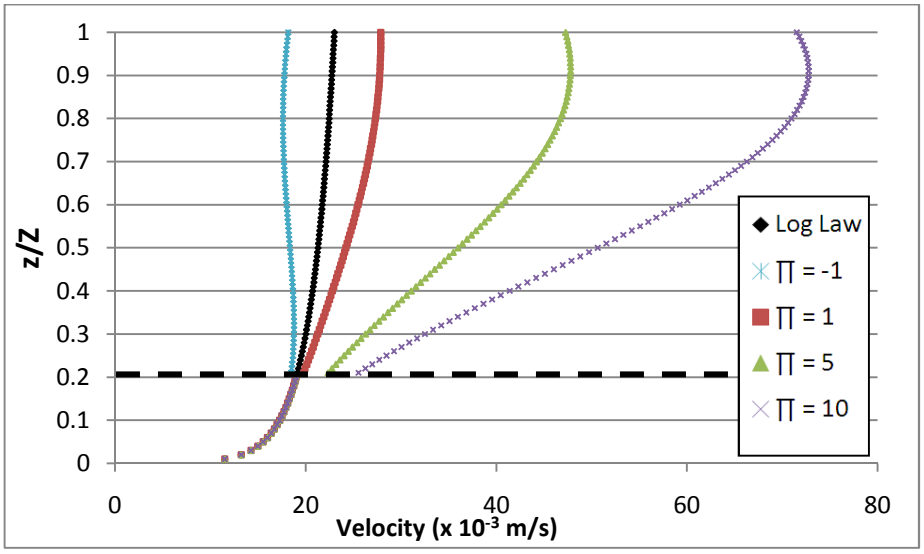

Figure 34. Comparison of the log law versus the Coles' wake law for different Π values when $z_c = 0.9$.

3.3.4.2.1 Shear Stress Estimated Using the Inner Velocity Profile

The shear stress transmitted from the water on the bed is critical for the prediction of sediment entrainment. The general form for calculating shear stress is:

$$\tau_u = \rho u^{*2} \tag{33}$$

where: τ = shear stress [kg/ms^2]
u_* = shear velocity [m/s]

The value of u* was extrapolated using the Clauser chart method following Wei et al. (2005) using the velocity data of the inner zone as:

$$\frac{\bar{u}}{u_c} = \sqrt{\left(\frac{u^*}{u_c}\right)^2}\left(\frac{1}{\kappa}\ln\left(\frac{z*u_c}{\mu}\right) + \frac{1}{\kappa}\ln\left(\sqrt{\left(\frac{u^*}{u_c}\right)^2}\right) + 5\right) \tag{34}$$

where: u_c = maximum velocity in the profile [m/s]

3.3.4.2.2 Shear Stress Estimated Using the Reynolds Stress Profile

The Reynolds stress (τ_{Re}) profiles were calculated using Equation 29. The shear stress measurement from the Reynolds stress (τ_r) was taken from the first good data point near the bed. Extrapolation of the Reynolds stress to the bed caused irregular results due to the high slope near the bed. This especially occurred in areas of deceleration, and therefore, an extrapolation method was not used.

3.3.4.2.3 Coles' Wake Parameter Estimated Using the Outer Velocity Profile

The Coles' wake parameter (Π) was calculated by fitting the velocity profile of the outer zone to the following equation (Onitsuka et al., 2009):

$$\frac{u_c - \bar{u}}{u^*} = \frac{2\Pi}{\kappa}\cos^2\left(\frac{\pi}{2}\frac{z}{z_c}\right) - \ln\left(\frac{z}{z_c}\right)/\kappa \tag{35}$$

In order to obtain realistic results, a condition was set that stated that at least three points had to be in the profile in order for the fitting function to occur. If this condition was not met, the Π value was not calculated for that profile and the result will show a blank space on the contour plot.

3.3.4.3 Calculation of Coherent Structures

Coherent structures describe how the largest structures in turbulent flow are organized, and are defined by a length or time period. Coherent structures are important in understanding the process of energy production and dissipation in the flow due to turbulence (O'Neill et al., 2004). A correlation function describes how related two random data series are to one another through different changes in time or distance steps. For example, data sampled from two time series close to one another should have a higher correlation than data sampled from a larger time step. The integral time scale (ITS) is defined as the characteristic time scale for the dynamics of measured quantities in turbulent flow. The integral length scale (ILS) is a measure of the longest correlation distance between the velocities at two points in the flow field (O'Neill et al, 2004). The correlation characteristics for both parameters are similar, showing a fast decay of the correlation at small distances followed by a slowly damped oscillation (Figure 35).

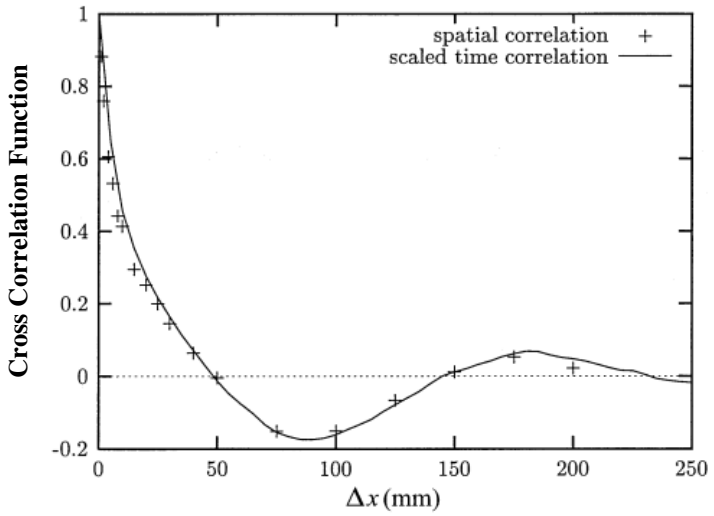

Figure 35. Spatial and temporal cross correlation function at different time and distance steps (Uijttewaal and Tukker, 1998).

The characteristic length or time scale of the large scale motion is the distance or time between the first and second maximum of the oscillation. The characteristic length or time of the small scale motions are more difficult to define, but can be estimated from the distance or time where the fast decaying correlation changes over the oscillating characteristic (~20 mm in Figure 35).

3.3.4.3.1 Integral Time Scale

The ITS is a measure of the correlation sequence of a turbulent process at one location through shifts in time. The time-shifted cross-correlation sequence is given by (Uijttewaal and Tukker, 1998):

$$R_t(\Delta t) = \frac{\langle u(x,t_o)\cdot u(x,t_o+\Delta t)\rangle}{(\langle u^2(x,t_o)\rangle\langle u^2(x,t_o+\Delta t)\rangle)^{0.5}} \quad (36)$$

where: R_t = time-shifted cross-correlation sequence
t_o = reference time [s]
Δt = change in time [s]
x = position [m]
$< >$ = denotes average of time interval

The cross-correlation sequence of the velocity data was calculated in MATLAB, and was set to have a lag range of -500 to 500, and to be normalized so that the autocorrelations at zero lag are identically equal to 1.0. The correlation sequence was then checked against the 99% significance level threshold, which was equal to a correlation value of 0.034. When the correlation value dropped below this threshold, the correlation sequence was considered to no longer be significantly related, and the ITS of the correlation was computed, as:

$$ITS = \int_0^T R_t\,(t)dt \quad (37)$$

where: t = time [s]
dt = time step [s]
T = time at which correlation still exceeds 99% significance limit threshold [s]

3.3.4.3.2 Integral Length Scale

The ILS is a measurement of the longest correlation distance between the velocities at two points in the flow field. The spatial cross-correlation sequence was estimated in MATLAB (Uijttewaal and Tukker, 1998), as:

$$R_x(\Delta x) = \frac{\langle u(x_o)\cdot u(x_o+\Delta x)\rangle}{(\langle u^2(x_o)\rangle\langle u^2(x_o+\Delta x)\rangle)^{0.5}} \quad (38)$$

where: R_x = spatial cross-correlation sequence
x_o = reference position [m]
Δx = change in position [m]

The cross-correlation sequence was set to have a lag range of 0, and to be normalized so that the autocorrelations at zero lag were identically equal to 1.0. The cross-correlation data is compared against the 95% significance level threshold, which was equal to a correlation value of 0.024. When

the correlation value dropped below this threshold, the correlation sequence was considered to no longer be significantly related, and the ILS of the correlation was computed, as:

$$\mathrm{ILS} = \int_0^X R_x(x)\,dx \tag{39}$$

where: R_x = spatial cross-correlation sequence

x = distance [m]

dx = distance step [m]

X = distance where correlation still exceeds 95% significance limit threshold [m]

Chapter 4

RESULTS

The results section presents the flow parameters calculated for the different configurations tested. These results are broken into two subsections, the results from the change in pool length, and the results from the change in riffle length. The results are presented in a variety of views including from the side (XZ plane), from the top (XY plane), and from a cross-sectional view (YZ plane). For clarity, the bedform sections are referred to by their specific zone, which is based on the bed slope, as indicated below (Figure 36).

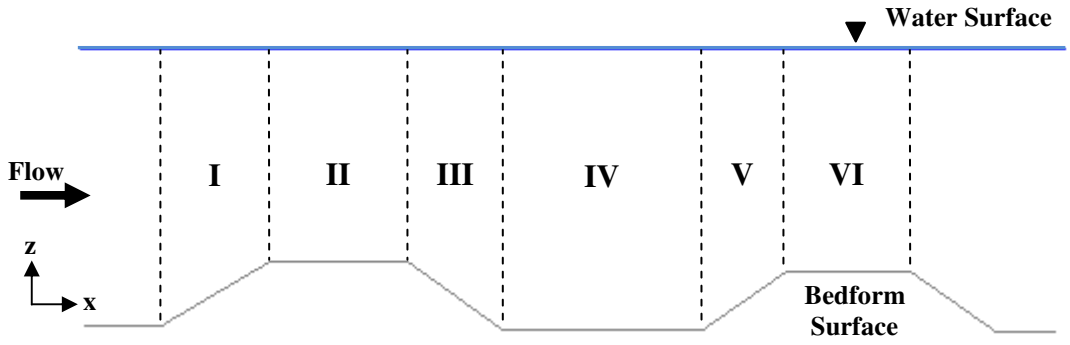

Figure 36. Sketch of the bedform zones in the XZ plane.

When the results are presented in the XY plane, the zoning system will be considered the same way as above, and the sloped sections will be indicated by a set of short horizontal lines connected to the vertical line that is the highest part of the section, i.e., the edges of the riffle (zone II) (Figure 37).

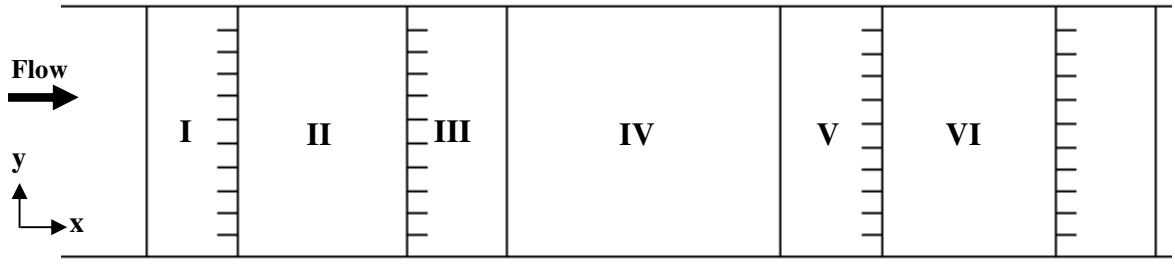

Figure 37. Sketch of the bedform zones in the XY plane.

When the results are presented in the YZ plane, they will be shown from cross-sections at 10%, 50%, and 80% of the pool (Figure 38).

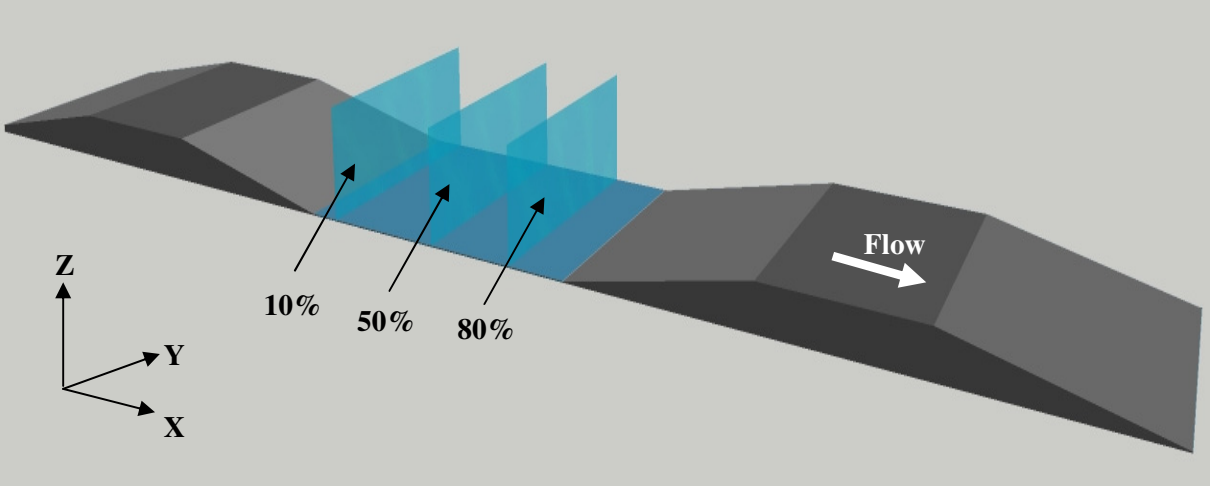

Figure 38. Model showing pool cross-sections at 10%, 50%, and 80%.

The first results presented are the changes in the mean streamwise velocity. From the streamwise velocity, the changes in the Coles' wake parameter (Π), and one estimate of the shear stress (τ_u) can be explored, as these parameters are fit to the slope of the velocity profile. Following this, the vertical velocity is considered, showing the impact of the bedforms on the flow distribution. The Reynolds shear stress is then presented along with the shear stress estimated on the Reynolds stress (τ_r), which is important in determining turbulence strength and characteristics. Finally, the coherent structures of the different runs are presented showing the strength and location of coherent turbulence as it is affected by the different configurations of the bedforms.

4.1 Pool Length

The first variable tested was the effect that the pool length, or the length of zone IV, had on the hydrodynamics within the flume. These results include the data collected from Run 1 to Run 4 (Table 2).

4.1.1 Distribution of Flow

The streamwise velocity profiles in zones I, II, and III, have similar contours in all runs (Figure 39). This result verifies that the flow is uniform before entering the testing area, and that the downstream configurations are not impacting the flow in the initial contraction section. The contour lines in all runs change from angled to nearly vertical at the end of zone I and through zone II, and return to angled or

even horizontal in zone III and zone IV (Figure 39). These results indicate that the vertical velocity gradient is decreasing as the flow moves through zone I, and increasing in zone III and IV.

The streamwise velocity in zone IV changes as the pool length increases (Figure 39). When zone IV is short in length, the water velocity near the surface stays relatively high across the section, and the velocity near the bed is relatively slow. When zone IV's length increases, the velocity in the middle of the section near the surface decreases, and increases near the bed. These results suggest that in longer bedforms the flow is more redistributed, as the velocity slows near the water surface and increases near the bed surface. Overall, longer lengths of zone IV result in lower velocities near the surface and reduce the vertical velocity gradient at the end of the zone.

Deviations from smooth contours can be observed in many of the streamwise velocity plots in zone I (Figure 39). These bumps are thought to be related to a reflectance problem from the UVPs pointed in the downstream direction that causes poor quality data. This problem is observed in multiple runs and is considered to be an error that was not remedied by the filtering process. All other bumps observed in this area will also be considered errors and will not be described in subsequent results.

When viewed near the channel wall, the streamwise velocity profiles in zones I, II, and III, have similar contours for all runs as the length of zone IV increases (Figure 40). The only difference is the slight change in velocity gradient contours at the transition from zone II to zone III near the bed surface.

There is little difference in the velocity magnitude in zone IV near the wall, despite the fact that the pool length is changing, and despite the differences observed at the centerline (Figure 40). These results show that the pool length does not impact the flow distribution near the wall in the same way that it does on the flow at the centerline.

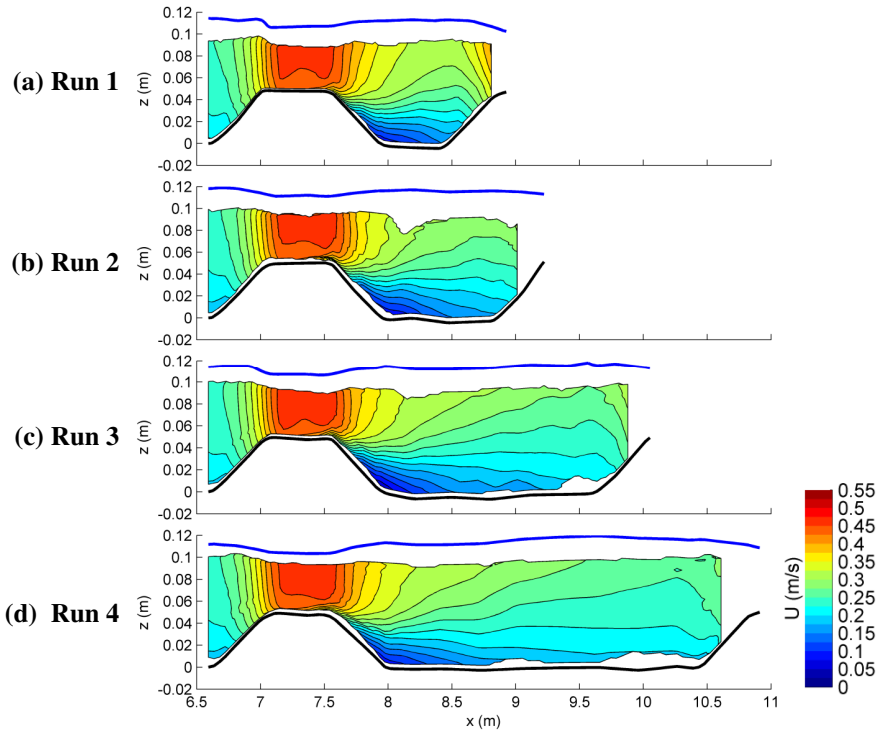

Figure 39. Mean streamwise velocity (U) in the XZ plane at the channel centerline (y=0.30 m) for Runs 1 through 4.

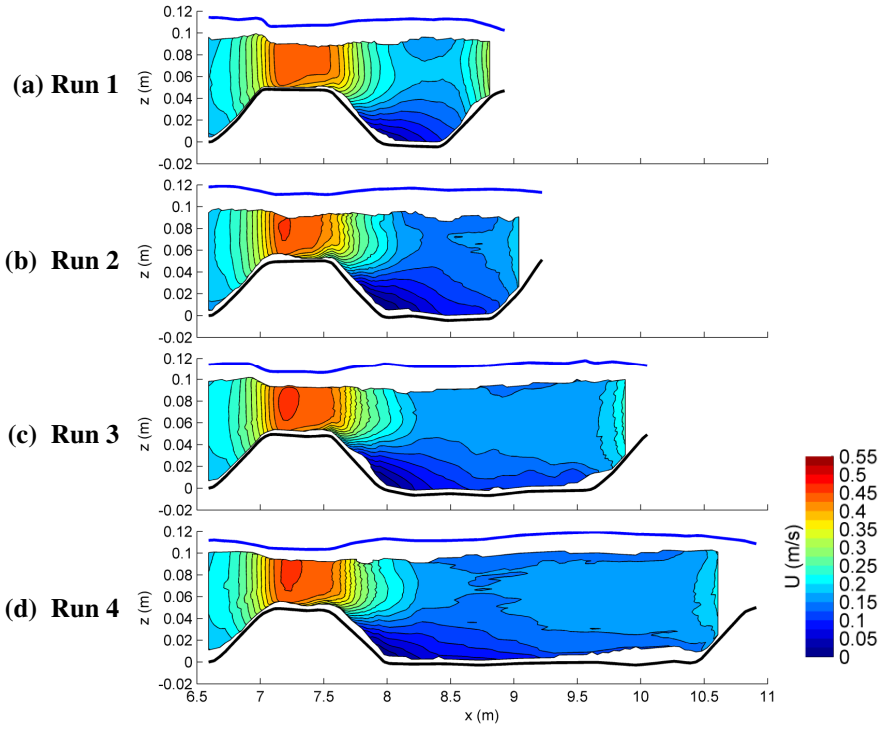

Figure 40. Mean streamwise velocity (U) in the XZ plane near the channel wall (y=0.03 m) for Runs 1 through 4.

Viewed in cross-section, it is clear that higher velocities in zone IV occur near the center of the channel, while the lower velocities occur near the bed and side walls (Figure 41). Towards the end of zone IV, the higher streamwise velocities extend to more regions of the cross-section, creating boundary velocities more similar to those in the rest of the cross section (Figure 41iii). The streamwise velocity in Runs 1 and 2 show rapid velocity gradients at the end of zone IV, while Runs 3 and 4 show gradual changes in velocity gradients near the end of zone IV (Figure 41iii). These results show that longer pools produce a more uniform velocity flow distribution at the end of the pool. Overall, the velocity is lower near the water surface, but higher near the bed and side walls as zone IV's length increases.

A dip in the streamwise velocity is observed in the cross-sectional results, particularly in the downstream end of the longer pools (Figure 41iic,d and Figure 41iiib,c,d). Near the water surface, the velocity gradient contours bend creating a rounded contour, so the maximum velocity is below the free water surface. This result indicates that the walls are having an influence on the flow distribution.

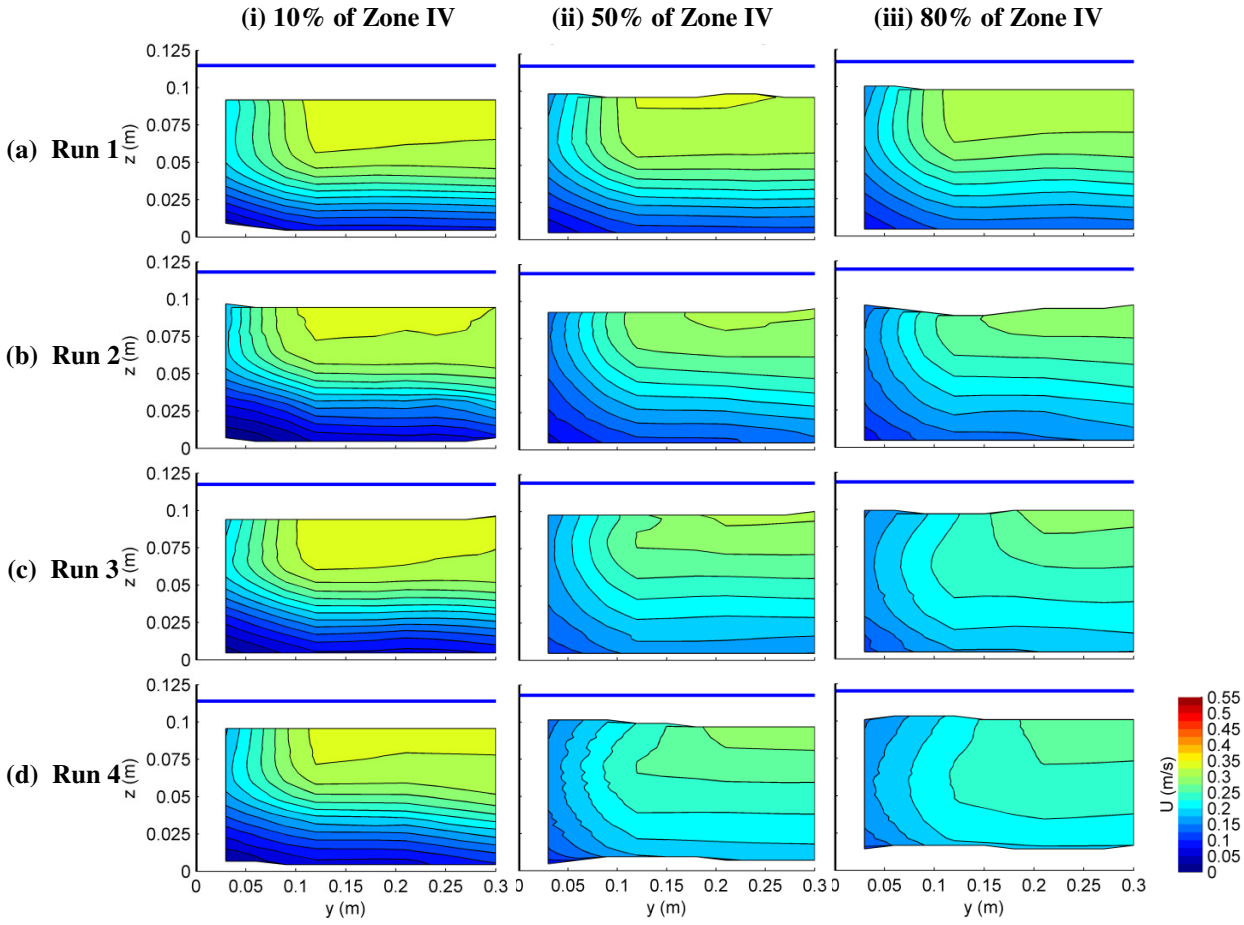

Figure 41. Mean streamwise velocity (U) in the YZ plane for Runs 1 through 4 at 10%, 50%, and 80% of zone IV.

The velocity profiles at the start of zone IV are similar for all runs, marked by a prominent change in slope at z/Z≈0.045 (Figure 42). By the end of zone IV, Run 1 still has that similar profile shape, while Run 4 has a more linear velocity profile at the channel centerline (Figure 42a). Overall, the velocity increases as the distance from the bed increases, and all velocities are similar at z/Z≈0.3. At the start of zone IV near the wall, the velocity profile is similar for all runs, with slight variations in magnitude near the bed (Figure 42b). At the end of zone IV near the wall, the velocities are very similar, and there is less velocity gradient through the water depth. In the middle of zone IV, at both the channel centerline and wall, the longer pools have faster near-bed velocities and slower near surface velocities with a pivot point at approximately z/Z≈0.3 (Figure 42ii). These differences have largely disappeared by the end of the pool.

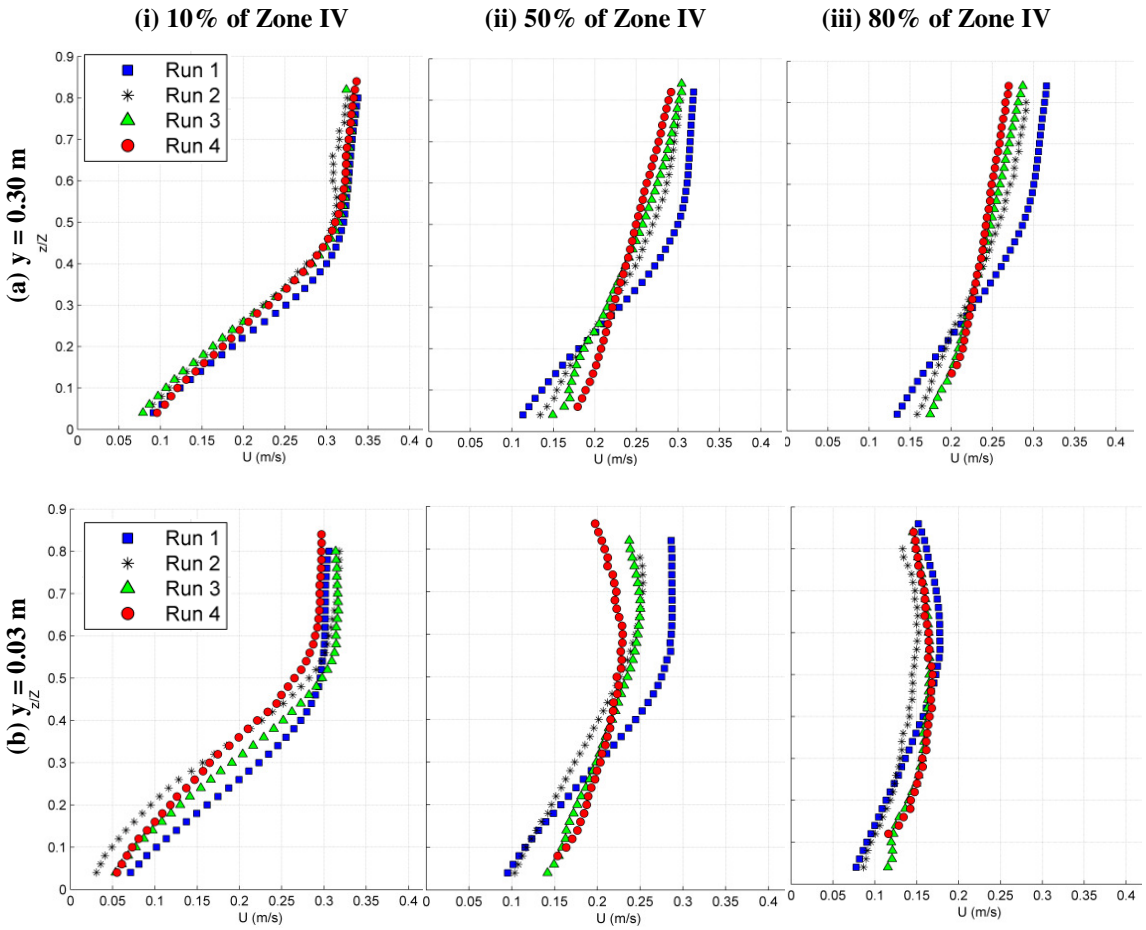

Figure 42. Streamwise velocity (U) profiles for Runs 1 through 4 at 10%, 50% and 80% of zone IV at y = 0.30 m and 0.03 m.

The shear stress estimated from the velocity gradient in the inner zone increases at the end of zone I and through zone II, and decreases in zone III (Figure 43). These results indicate that the velocity profile has a steeper slope near the bed in zones I and II due to the increase in velocity, and that this slope

decreases in zone III due to the deceleration of flow. Areas of higher shear stress in the center of the longer pools confirm the increase in near-bed velocities shown in Figure 39. The shear stress in zone IV is near zero at the beginning and along the side wall, and increases towards the middle of the channel as the flow moves downstream (Figure 43). The bed velocities in zone III, at the start of zone IV, and near the wall through zone IV, are slow, which leads to very low shear stress in those areas. The bed velocities near the end of zone IV increase with increasing zone length, leading to the observed increase in shear stress (Figure 43).

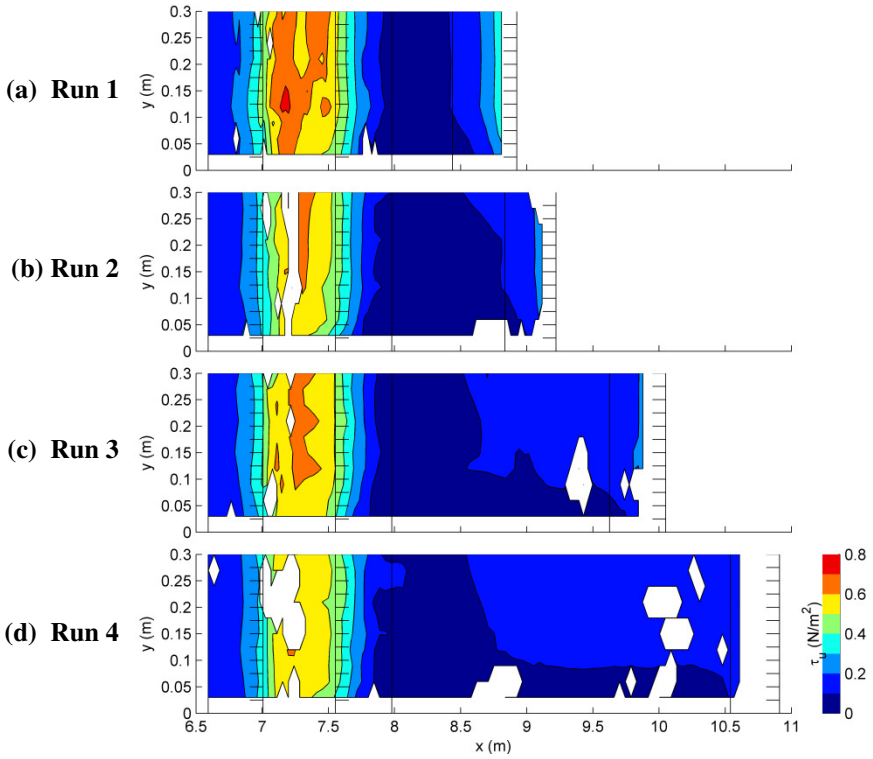

Figure 43. Shear stress estimated from the velocity profile (τ_u) in the XY plane for Runs 1 through 4.

The peak value of the Coles' wake parameter (Π) occurs in zone III, and the magnitude decreases in zone IV (Figure 44). These results indicate that the Π parameter is greatly affected by the channel wall and from the bedform expansion as there is a strong increase in wake strength of the velocity profile near the wall.

The value of Π is approximately zero by the end of zone IV for the longer runs (Figure 44). This indicates that the flow has achieved uniform flow by the end of zone IV, as the velocity profile is close to that of the log law (Equation 31). In shorter pools, Π remains high at the downstream end of the pool, and the flow distribution in zone V is not similar to the flow distribution in zone I. It should be noted that the white region in each planform contour plot occurs because there is not enough data over

its entire depth that meets the criteria to calculate the Coles' wake parameter, as discussed in Section 3.3.4.2.3.

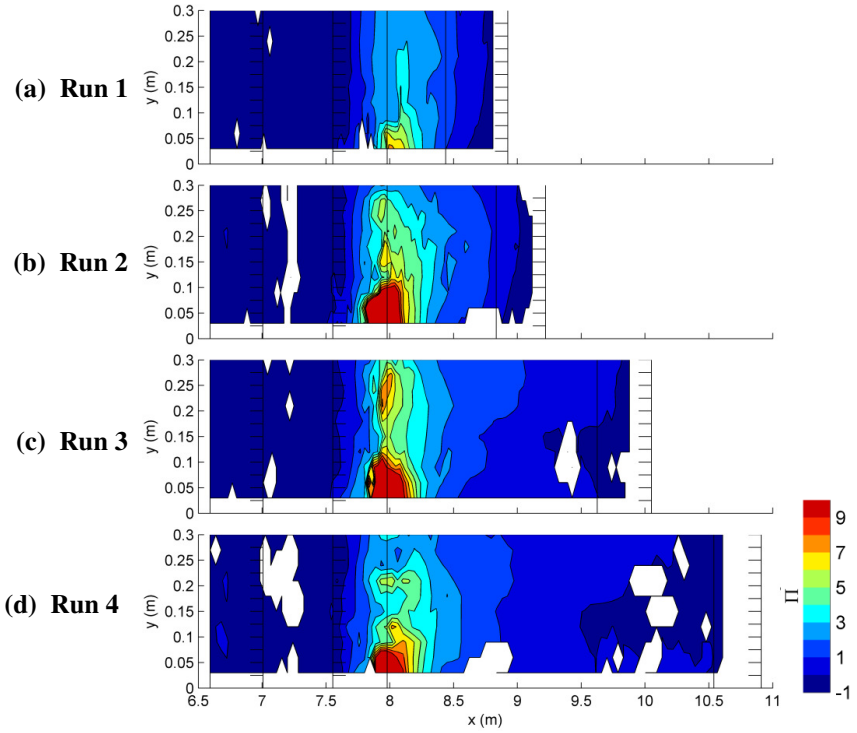

Figure 44. Coles' wake parameter (Π) in the XY plane for Runs 1 through 4.

4.1.2 Secondary Circulation

The vertical velocity can be utilized as an indication of secondary currents, as it can help describe the direction of the flow redistribution. The vertical velocity is usually used for this application when lateral current data is unavailable. Due to the probe's sensitivity, the vertical velocity is more variable than the streamwise velocity. In spite of this sensitivity, however, the patterns of the vertical velocity are still clearly visible. The vertical velocities are positive in zone I and negative in zone III (Figure 45), particularly near the bed. The maxima and minima of the positive and negative velocities are observed along the bed in between zone I and zone II, and in between zone II and zone III, respectfully. The vertical velocity in zone IV is slightly negative in all runs throughout the entire water depth.

The vertical velocity near the side wall and water surface in zone IV is consistently slightly positive, and the vertical velocity near the bed is slightly negative, with the transition occurring at approximately half the depth (Figure 46). This trend is observed in all runs and extends throughout almost the entire length of zone IV. This pattern seems to be related to the impact of both the channel walls and the bedform.

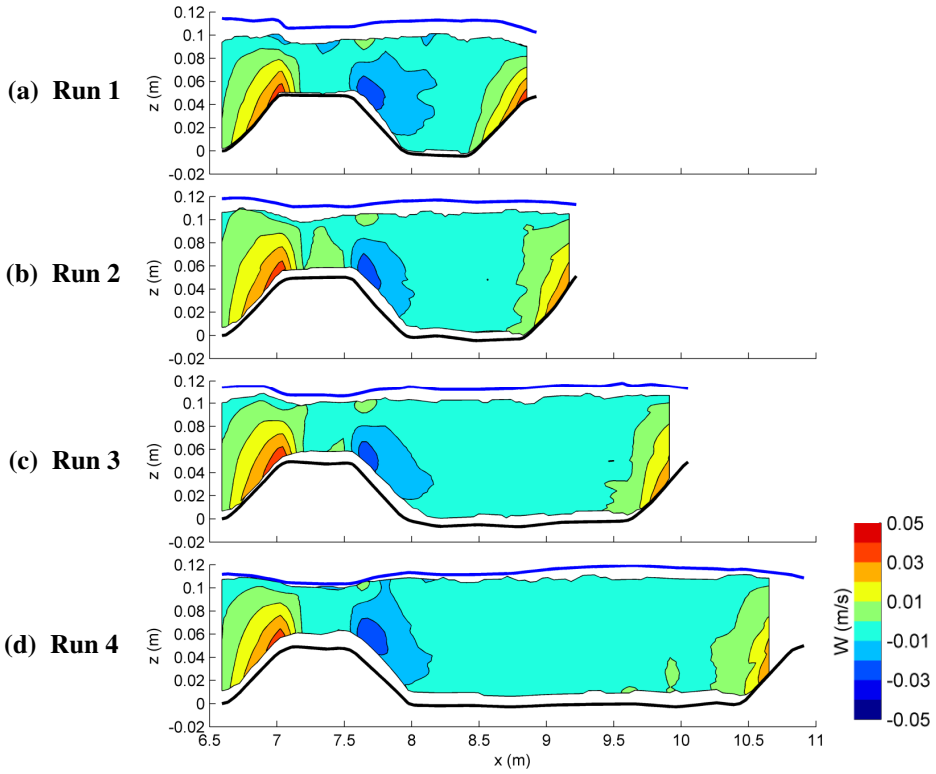

Figure 45. Mean vertical velocity (W) in the XZ plane at the channel centerline (y=0.30 m) for Runs 1 through 4.

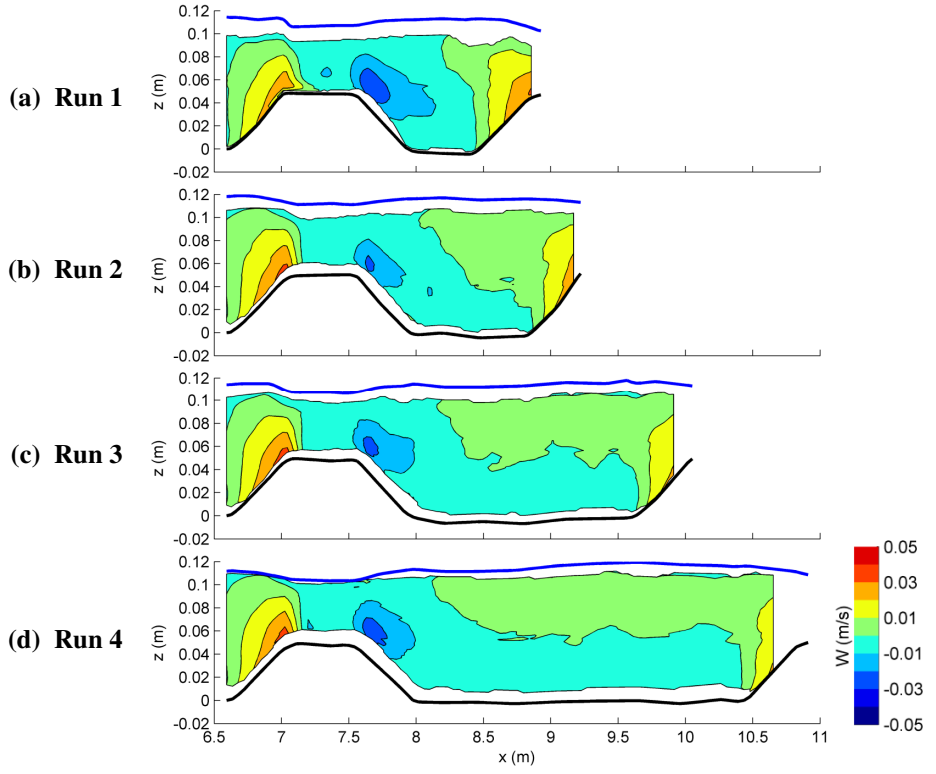

Figure 46. Mean vertical velocity (W) in the XZ plane near the channel wall (y=0.03 m) for Runs 1 through 4.

The magnitude of the vertical velocity increases as the flow moves through zone IV (Figure 47) (Note the change in colour scale from previous figures). Overall, the vertical velocities at the start of zone IV are negative. By the end of zone IV, the vertical velocities near the channel wall and water surface have a positive velocity, especially in the longer pools (Figure 47). The extent to which the vertical velocity near the wall extends into the channel width increases as the length of zone IV increases, and the positive velocities near the bed increase higher into the water depth as the length of the zone increases. The near wall flow in the vertical direction is redistributed toward the channel centerline as it reaches the water surface.

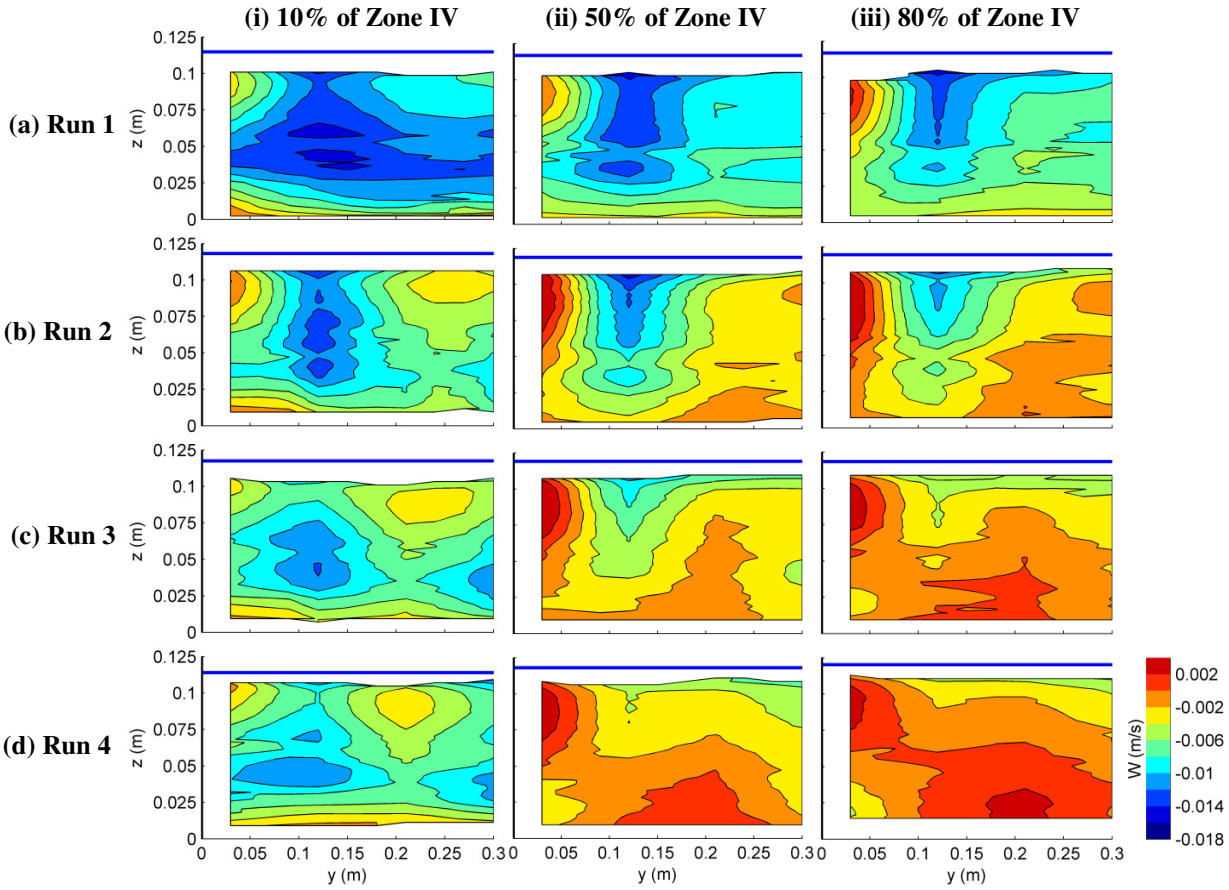

Figure 47. Mean vertical velocity (W) in the YZ plane for Runs 1 through 4 at 10%, 50%, and 80% of zone IV.

4.1.3 Distribution of Turbulence

Turbulence is generated as the flow expands through zone II and into zone III (Figure 48). The peak in the Reynolds stress occurs in zone III and at the start of zone IV. This location corresponds to areas of the lowest bed velocities, the flow expansion, and rapid velocity gradients in the streamwise direction. The peak in Reynolds stress is farther from the bed at the end of the pool as the length of zone IV

increases (Figure 48). This location corresponds to an increase in both positive vertical velocities, and τ_u.

It should be noted that there is an error in Run 2, as discussed in Section 3.3.2.1, which is especially noticeable in the Reynolds stress (Figure 48b). While the other runs show slightly positive Reynolds stress values in zone I and II, Run 2 shows a slightly negative trend. In zone III and zone IV, the Reynolds stress near the water surface for Run 2 is again negative while the other runs show slightly positive Reynolds stresses. This error is assumed to be attributed to the slight variations caused by the seeding problem which was not completely solved by the de-wrapping program. This phenomena shows up again in the subsequent results and will be considered an error from which no conclusions are drawn.

Compared to the centerline results, the distribution of the Reynolds stress near the wall is not as affected by the length of zone IV (Figure 49). The peak cell looks similar in term of size and magnitude for all runs even though the pool length increases. The peak magnitude, however, is greater near the wall than compared to the channel centerline. At the end of the longer pools, there is a zone of relatively strong negative Reynolds stress near the water surface (Figure 49c,d).

The magnitude of Reynolds stress decreases near the end of zone IV as the pool length increases (Figure 50). When zone IV is short in length, the magnitude of Reynolds stress stays very similar throughout the entire length of the pool. When zone IV's length increases, the Reynolds stress decreases greatly by the end of zone IV. For Runs 1 and 2, the Reynolds peak extends almost the entire width of the channel at the end of the pool, while in Runs 3 and 4, the peak is near the wall.

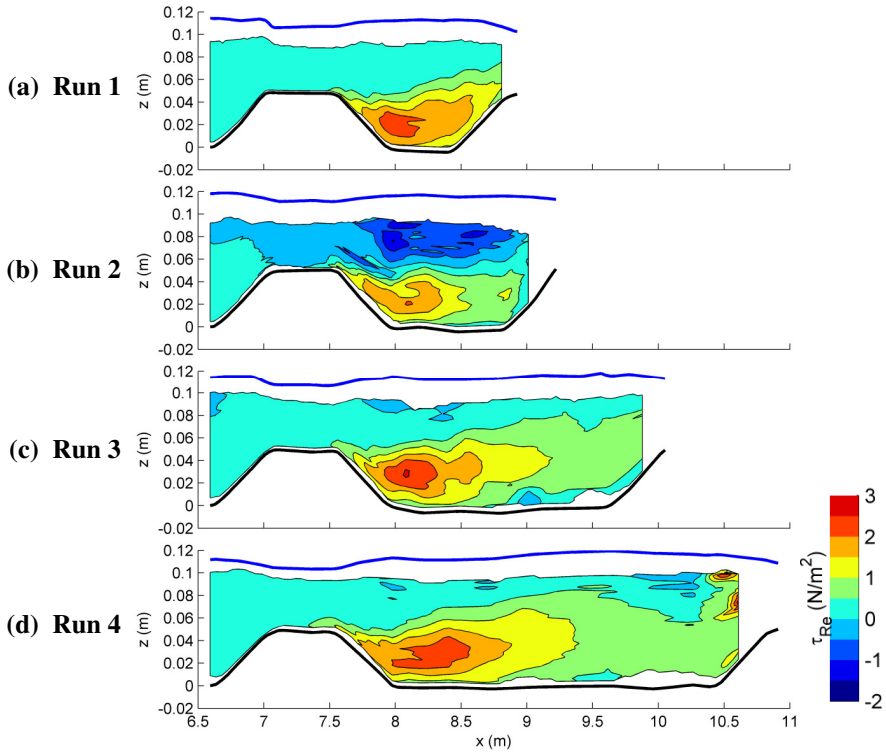

Figure 48. Reynolds stress (τ_{Re}) in the XZ plane at the channel centerline (y=0.30 m) for Runs 1 through 4.

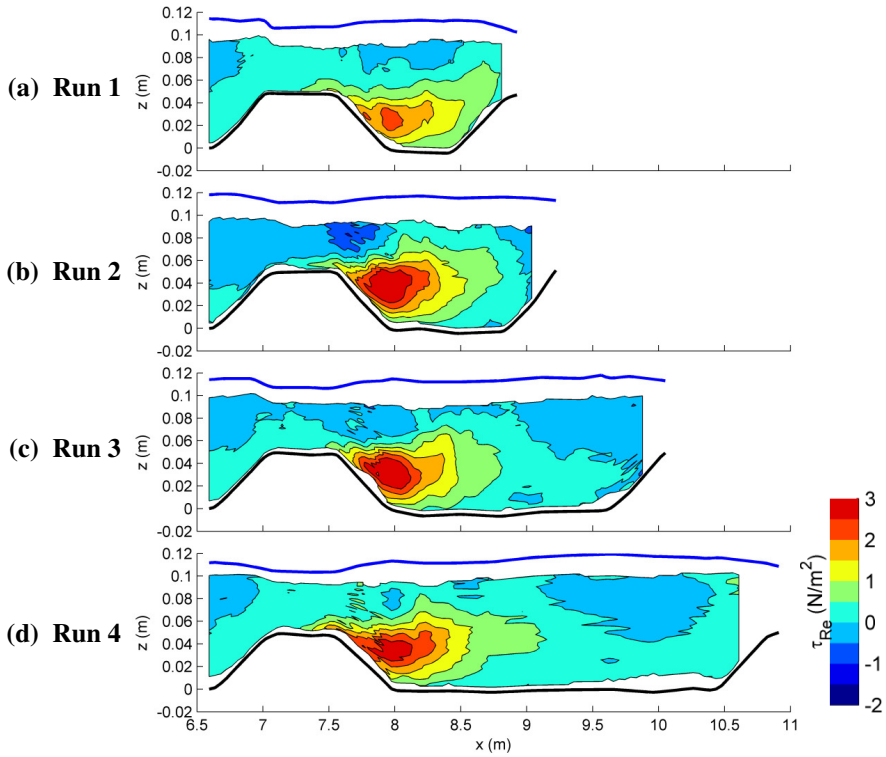

Figure 49. Reynolds stress (τ_{Re}) in the XZ plane near the channel wall (y=0.03 m) for Runs 1 through 4.

As zone IV's length increases, the peak in Reynolds stress shifts from the side wall to the center of the channel and also moves upwards (Figure 50). The location of the peak Reynolds stress shifts upward with increasing distance downstream in zone IV for Runs 2, 3 and 4, as at the peak is located in the lower third of the cross-section at the start of zone IV, and in the middle of the cross-section at the end of zone IV. The Reynolds stress changes from high values near the bed and very low values near the surface to a diagonal cross section as zone IV's length increases (Figure 50). This transition to the diagonally shaped profile of Reynolds stress is characteristic of uniform flow in an open channel (Nezu and Nakawaga, 1993).

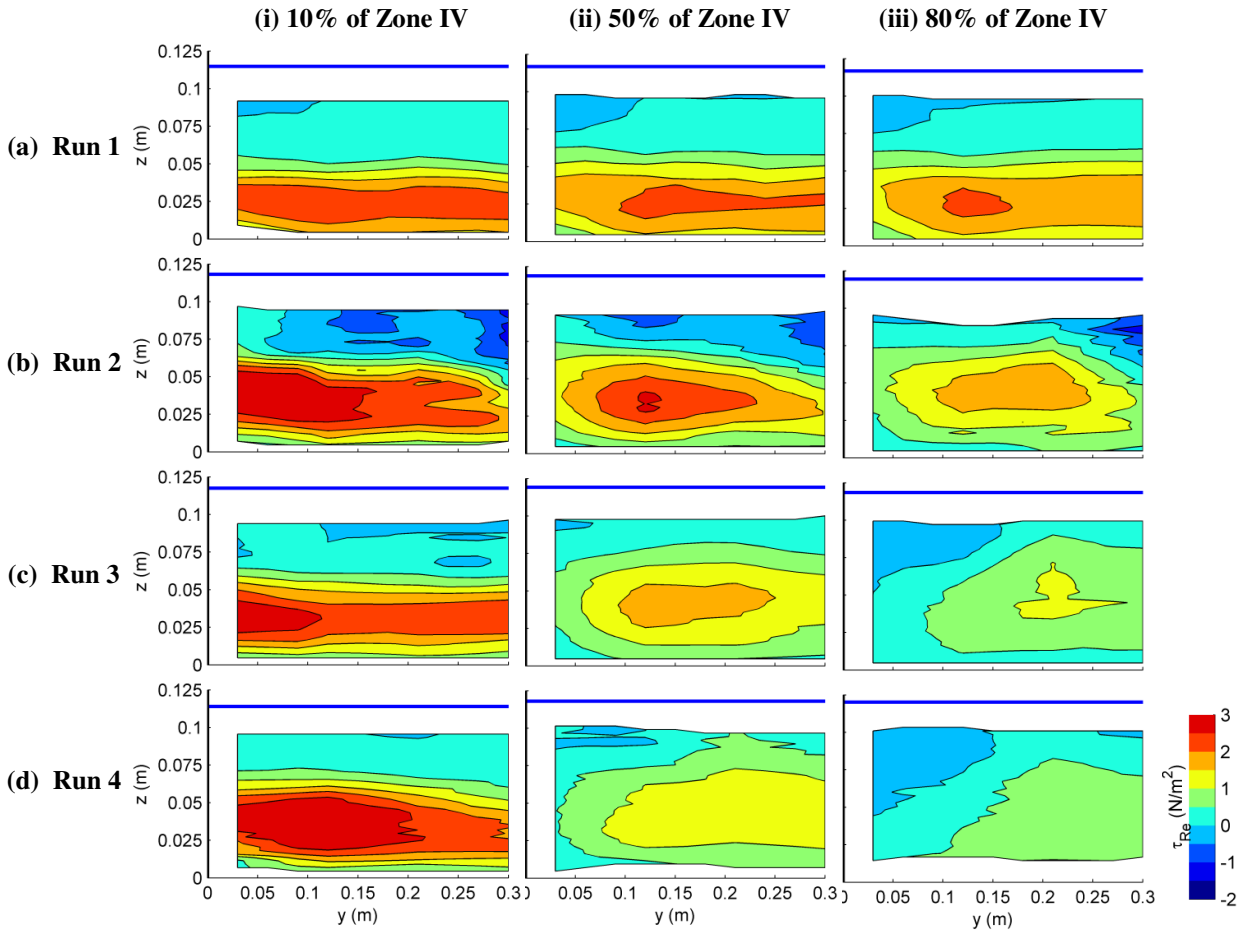

Figure 50. Reynolds stress (τ_{Re}) in the YZ plane for Runs 1 through 4 at 10%, 50%, and 80% of zone IV.

The Reynolds stress profile at the start of zone IV is high near the bed and low near the water surface (Figure 51i). This is due to the turbulence that is created near the bed and not at the water surface from the flow expansion. As the length of zone IV increases, the Reynolds stress decreases near the bed (Figure 51ii, iii). The Reynolds stress near the water surface at the end of zone IV has slightly negative

values near the wall (Figure 51biii). This is the same trend that was observed in the cross-sectional view where negative stress occurs near the water surface as the flow becomes uniform.

It should be noted that the Reynolds stress profile for Run 2 does not tend towards zero stress at the water surface like the other runs, which again indicates that there are errors associated with this run and that conclusions should not be based on the centerline data from Run 2.

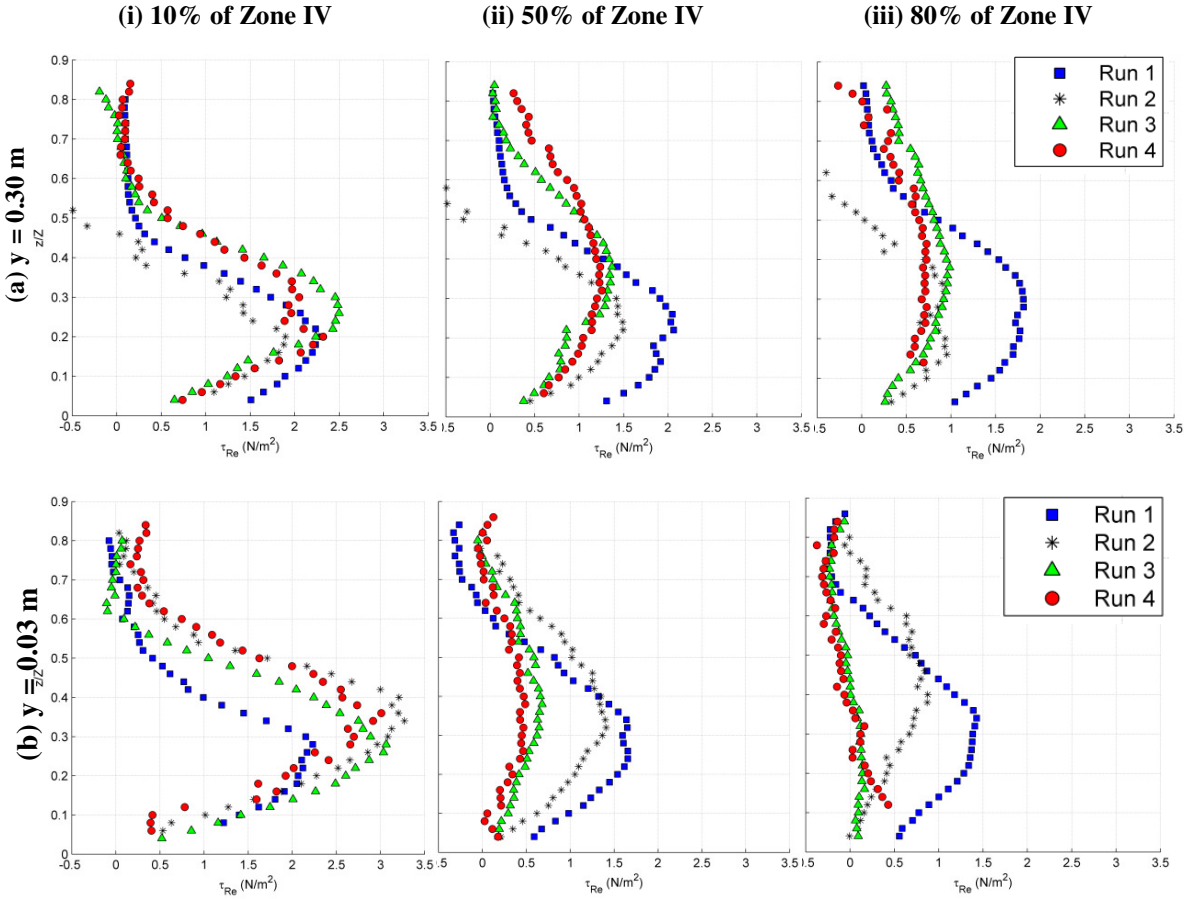

Figure 51. Reynolds stress (τ_{Re}) profiles for Runs 1 through 4 at 10%, 50% and 80% of zone IV at y = 0.30 m and 0.03 m.

The shear stress on the bed as estimated from the Reynolds stress profile (τ_r) peaks in zone III, especially near the channel wall, and decreases with increasing distance in zone IV (Figure 52). This peak corresponds to the increase in magnitude of the Reynolds stress observed in zone III. Elevated τ_r values extend through the entire length of zone IV for all runs with slightly lower values near the channel wall.

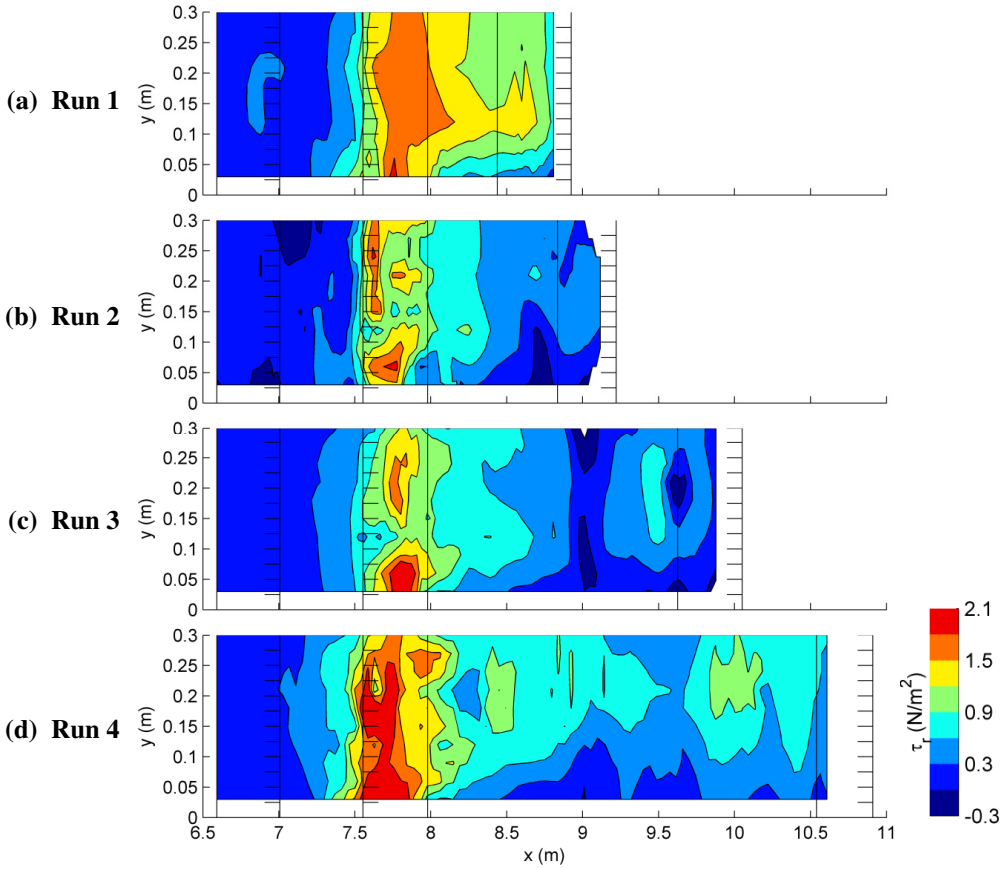

Figure 52. Shear stress estimated from the Reynolds stress profile (τ_r) in the XY plane for Runs 1 through 4.

The integral time scale (ITS) coherence shows that there is higher coherence in zone IV than in zone II (Figure 53). This increase in coherence occurs to a point in zone IV, then decreases in the longer pools. Overall, trends in the ITS are obscured by the variability observed at the channel centerline.

More consistent patterns in ITS coherence are observed near the wall, with a common peak in coherence near the bed surface at the transition from zone III to zone IV (Figure 54). This pocket of higher coherence may be related to the low streamwise velocities and low τ_u near the wall and bed in this transition area. The ITS coherence in zone II is very low (Figure 54), as the flow in this area is accelerating, and therefore, there is little coherence. In the downstream end of zone IV, the ITS decreases near the bed surface and increases near the water surface (Figure 54).

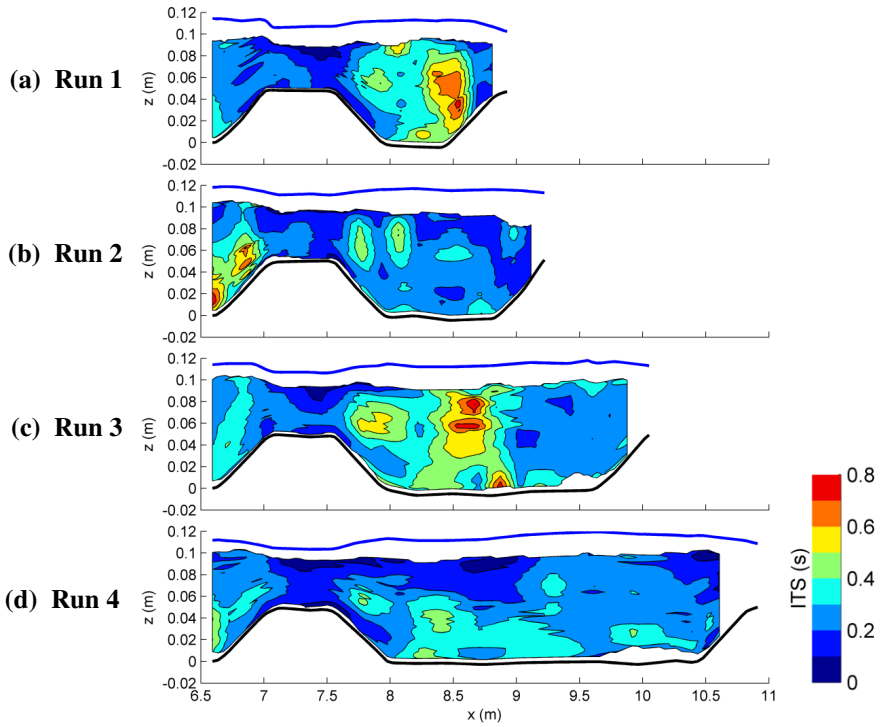

Figure 53. Integral time scale (ITS) in the XZ plane at the channel centerline (y=0.30 m) for Runs 1 through 4 using the US probe.

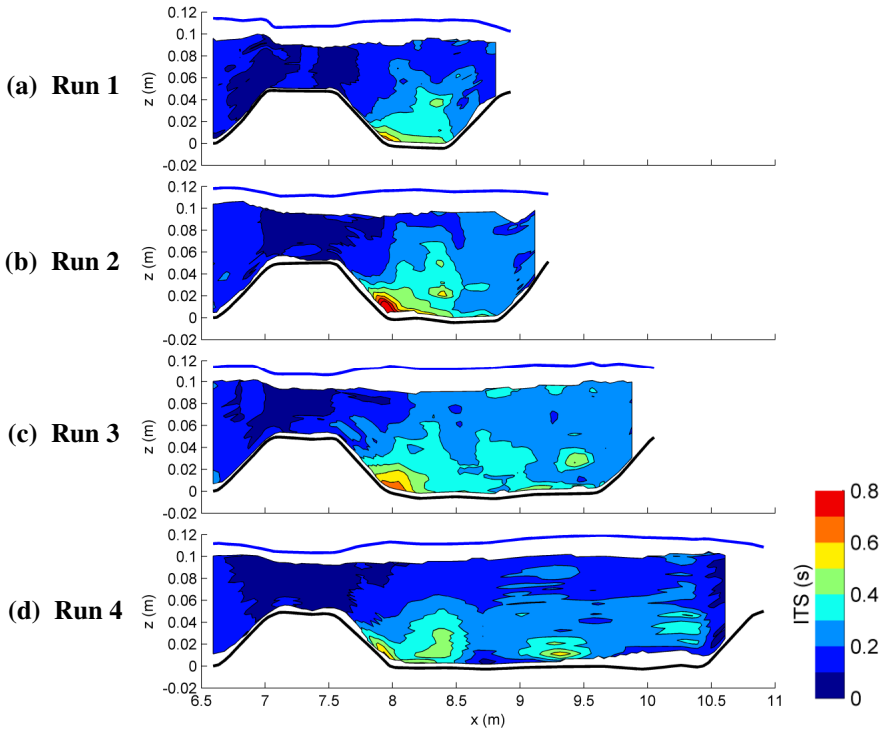

Figure 54. Integral time scale (ITS) in the XZ plane near the channel wall (y=0.03 m) for Runs 1 through 4 using the US probe.

High coherence in the integral length scale (ILS) is measured in the start of zone I (Figure 55). This area corresponds to uniform flow and low Reynolds stress. The measured ILS is low over zone II for all runs, as the flow in this area is accelerating. As the length of zone IV increases, the length of the measured coherence of the ILS increases with the highest peaks existing near the end of zone IV (Figure 55). The location of this peak corresponds with the downstream end of the zone of high Reynolds stress and Π parameter, as shown in Figure 44 and Figure 48.

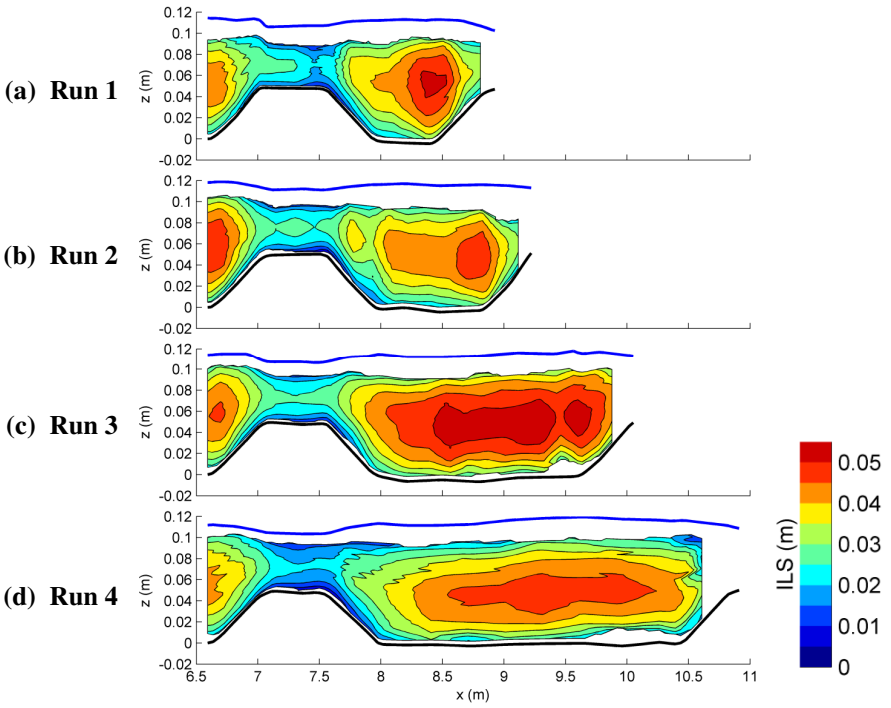

Figure 55. Integral length scale (ILS) in the XZ plane at the channel centerline (y=0.30 m) for Runs 1 through 4 using the US probe.

The magnitude of the ILS coherence is lower near the channel wall than compared to that in the middle of the channel (Figure 56). The overall shape of the contours is the same, with low coherence over zone II, and higher coherence in zone I and zone IV. The main difference from the centerline data is that the maximum values are much higher in zone IV when compared to zone I. Near the wall, the coherence tends to peak early in zone IV and decrease downstream.

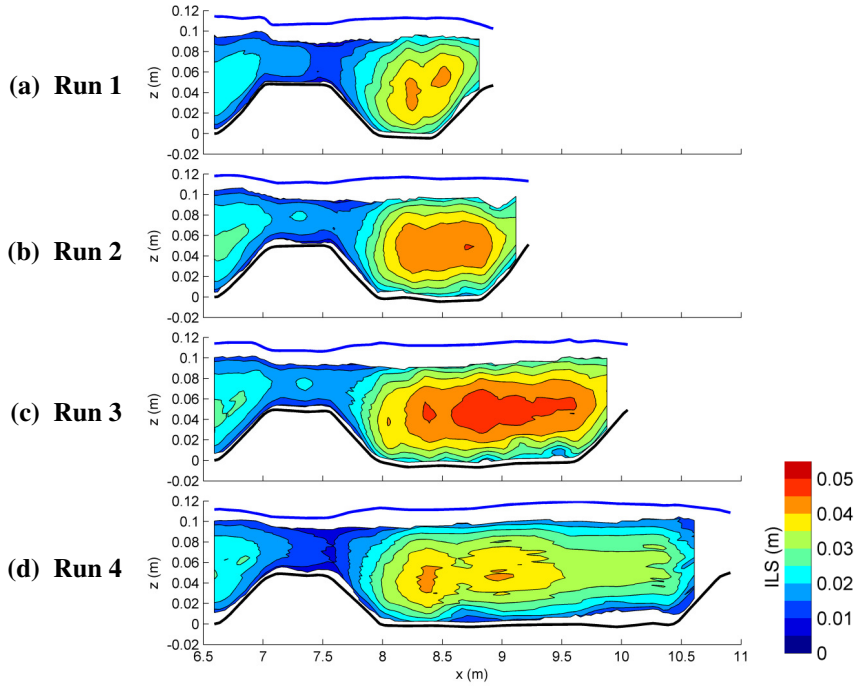

Figure 56. Integral length scale (ILS) in the XZ plane near the channel wall (y=0.03 m) for Runs 1 through 4 using the US probe.

4.2 Riffle Length

The second variable changed was the riffle length and how it affected the hydrodynamics within the flume. These results include the data collected from Runs 4 to Run 7 (Table 2). Overall, the riffle length data is largely consistent with the pool length tests. The results will concentrate on the differences from the results measured over the tests considering the change in pool length.

4.2.1 Distribution of Flow

The overall distribution of the flow is consistent with that observed in Runs 1 through 4, where the velocity gradient is decreasing in zone I, increasing in zone III, and decreasing in zone IV. The key difference is that the streamwise velocity over zone II increases in magnitude as zone II's length increases (Figure 57). Higher velocity magnitudes are observed at the end of zone II in Run 6 and even more so in Run 7, indicating that these increased lengths of zone II cause an acceleration of the flow at the centerline to higher velocities than previously observed. Higher velocities near the bed at the transition from zone II to zone III can also be seen in Runs 6 and 7. The streamwise velocity in zone IV increases along the water surface as zone II's length increases, however, the near-bed velocity stayed relatively similar (Figure 57). The increase in water surface velocity is related to the increase in velocity leaving zone II. The overall increase in velocity in Runs 6 and 7 creates steeper velocity gradients at the end of zone IV.

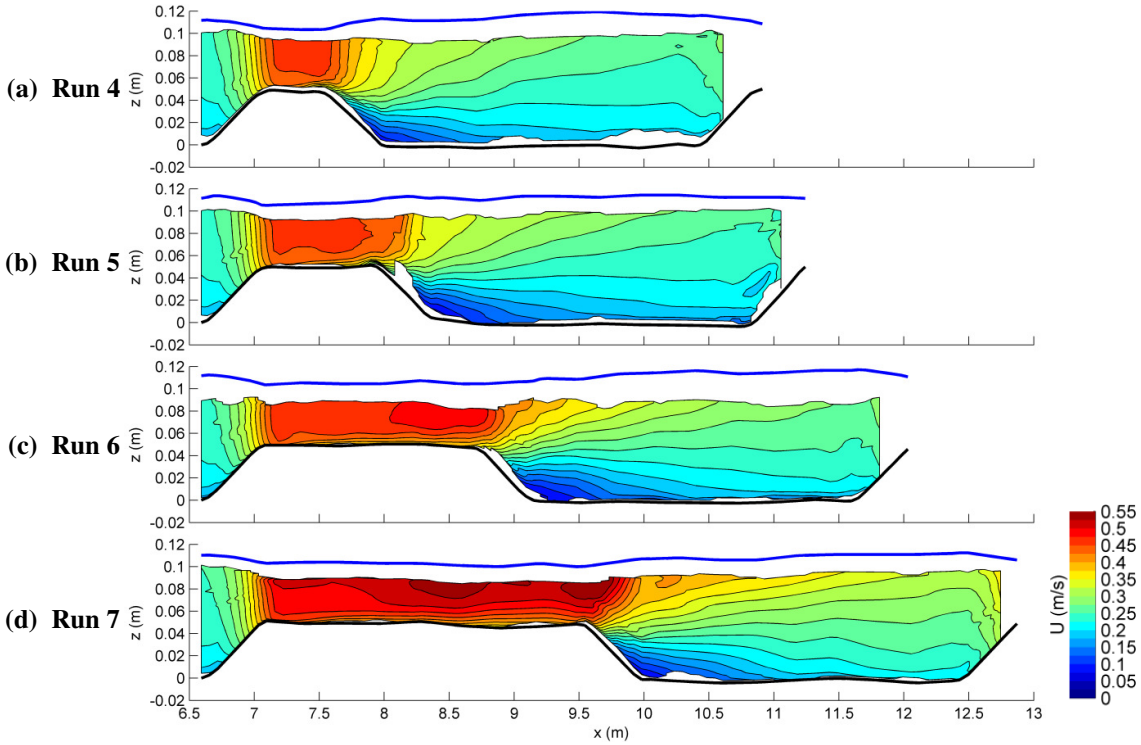

Figure 57. Mean streamwise velocity (U) in the XZ plane at the channel centerline (y=0.30 m) for Runs 4 through 7.

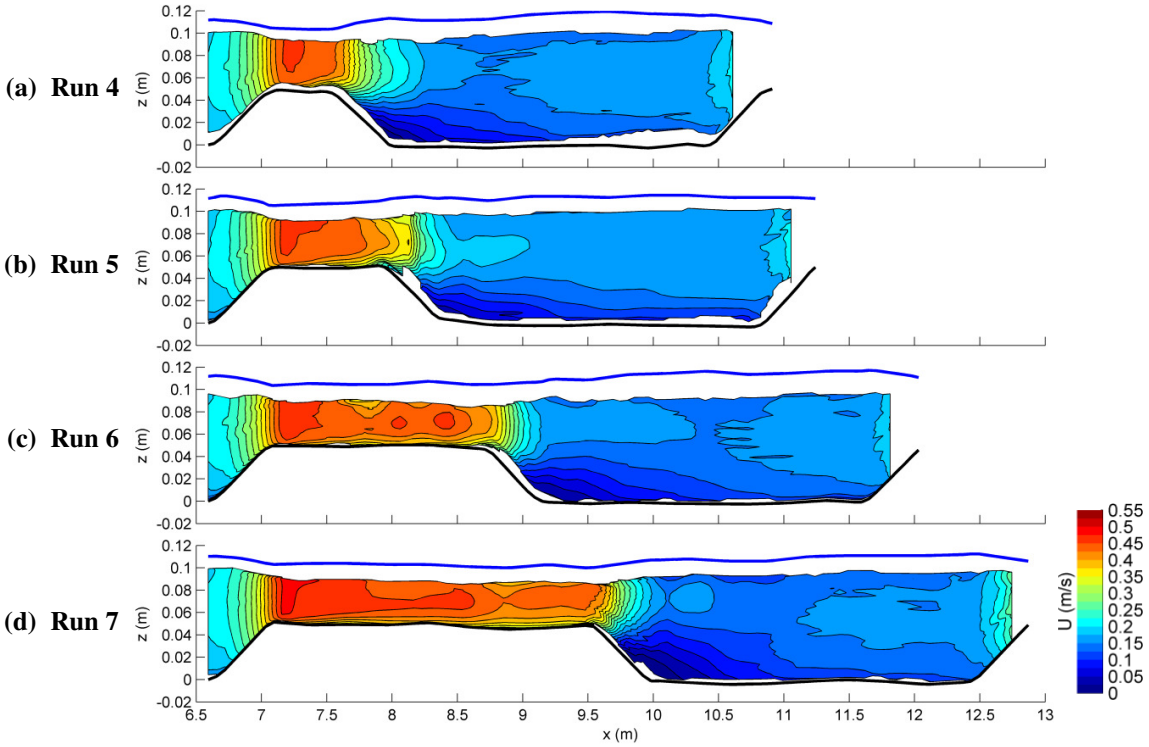

Figure 58. Mean streamwise velocity (U) in the XZ plane near the channel wall (y=0.03 m) for Runs 4 through 7.

Near the channel wall, the overall magnitude of the velocity in all zones is less than the velocity at the channel centerline (Figure 58). The velocity exiting zone II is very similar for all runs despite the change in riffle length. The velocity in zone IV has similar patterns to those observed in Figure 46.

When viewing the pool cross-section, the velocity contours in all runs are different at the start of zone IV (Figure 59). Run 6 and Run 7 have high velocity cores at the beginning of the pool, and very slow near-bed and near-wall velocities, while the other runs have a slower core and faster near-bed and near-wall velocities. As the flow moves toward a more uniform state, velocity gradients near the end of the pool show a more gradual change compared to at the beginning of the pool. Higher velocities near the water surface are still observed at the end of zone IV for Run 7. The velocity dip phenomenon is observed in Figure 59c,d, Figure 59ii, and Figure 59iii.

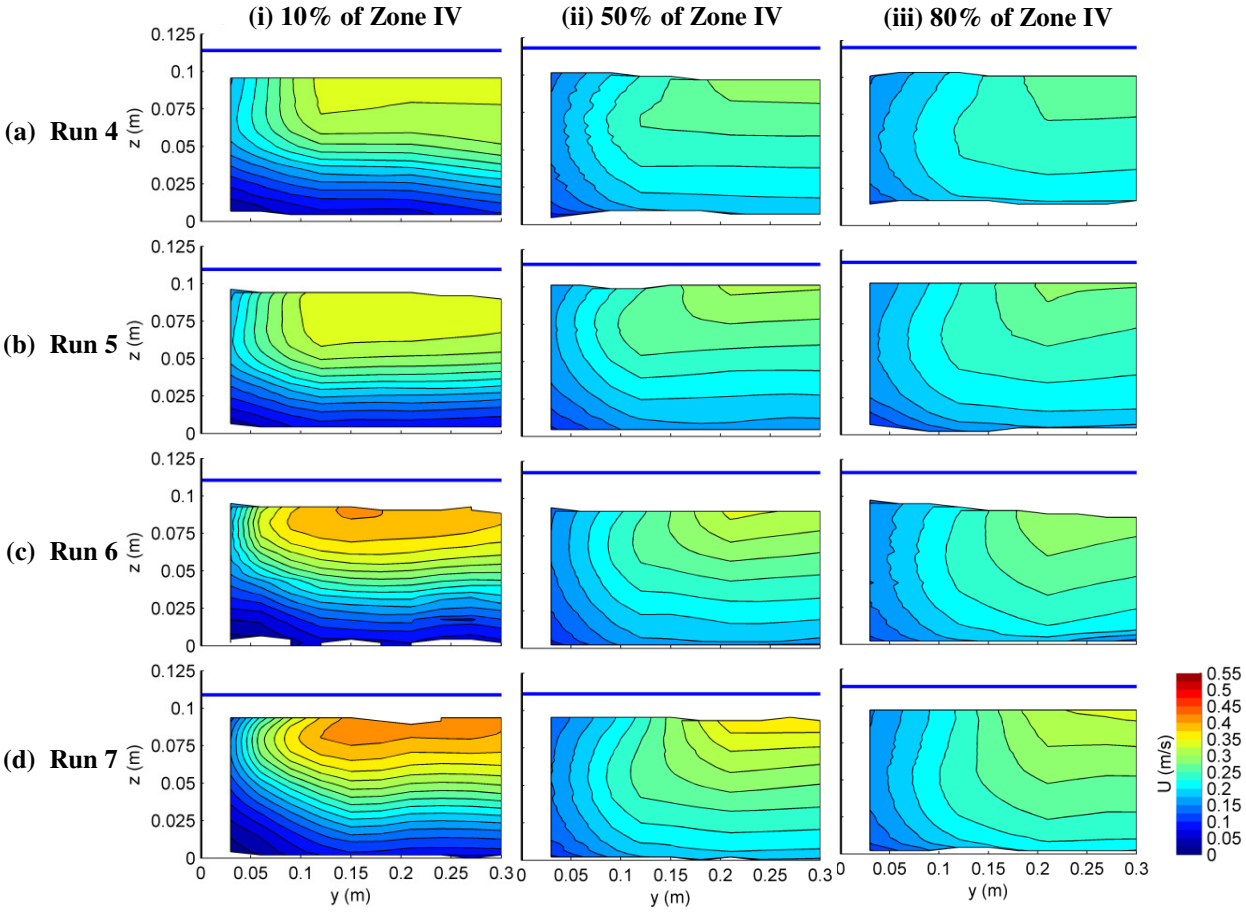

Figure 59. Mean streamwise velocity (U) in the YZ plane for Runs 4 through 7 at 10%, 50%, and 80% of zone IV.

Along the channel centerline at the start of the pool, the velocity profile near the bed is similar in all runs (Figure 60ai). The velocity profile near the water surface is different for each run as the velocity

exiting zone II increases with increasing zone II length. The transition from the similar profile to different profiles occurs at z/Z≈0.50. Near the channel wall, the velocity profiles at the start of the pool have similar profiles for all runs except Run 7 (Figure 60bi). Overall, Run 7 has a slower velocity over the entire water depth as compared to the other runs.

At the channel centerline near the middle and end of the pool, the velocity profile in each run is fairly constant (Figure 60ii and Figure 60iii). The shape of each run's velocity profile remains constant while the magnitude varies slightly between the different runs. These profiles show that the maximum velocity occurs at the water surface. At the channel wall, the velocity profile in all runs is very similar, as the flow moves downstream of the pool (Figure 60bii and Figure 60biii). These profiles show that the peak velocity is slightly below the surface near the wall in all runs.

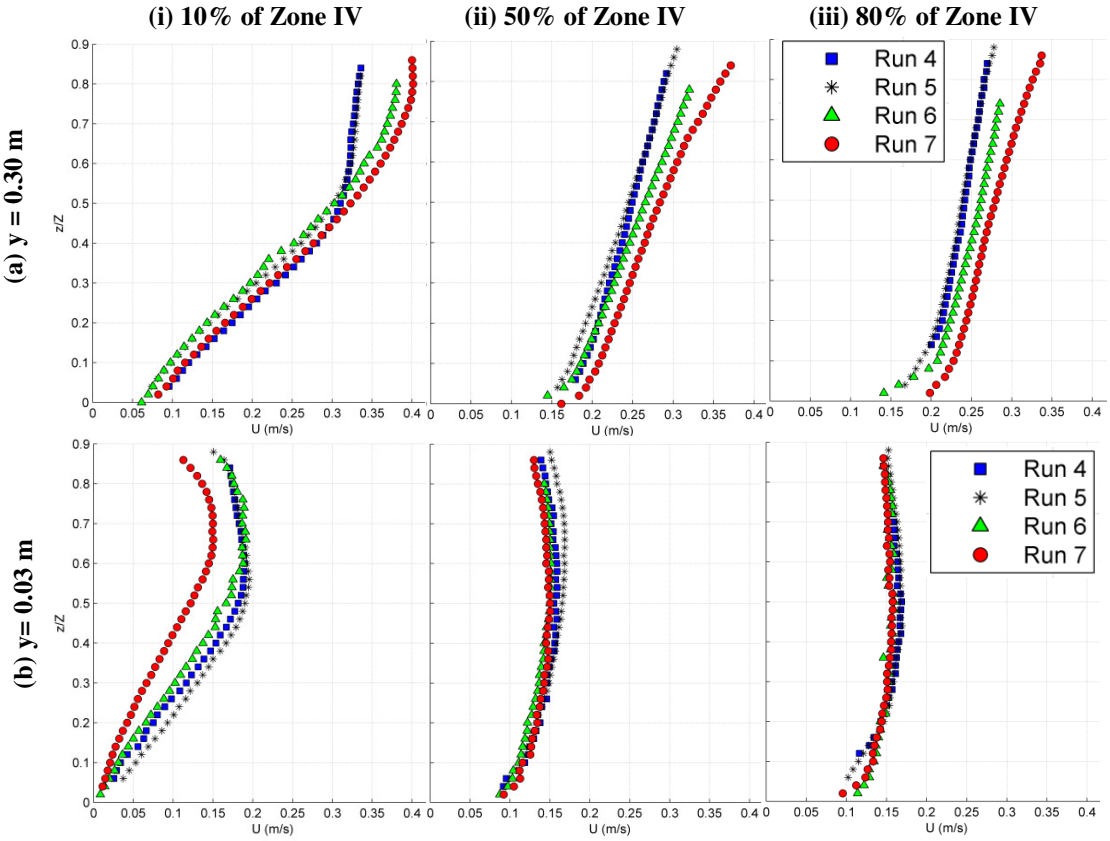

Figure 60. Velocity (U) profiles for Runs 4 through 7 at 10%, 50% and 80% of zone IV at y = 0.30 m and 0.03 m.

The shear stress estimated from the velocity profile increases as the length of zone II increases (Figure 61). This stress corresponds to the increase in velocity over zone II. The shear stress decreases through zone III, and is slightly elevated in the middle of zone IV, but stays near zero along the channel wall and at the start of zone IV (Figure 61). These results are similar to that seen for the results as the pool length increases.

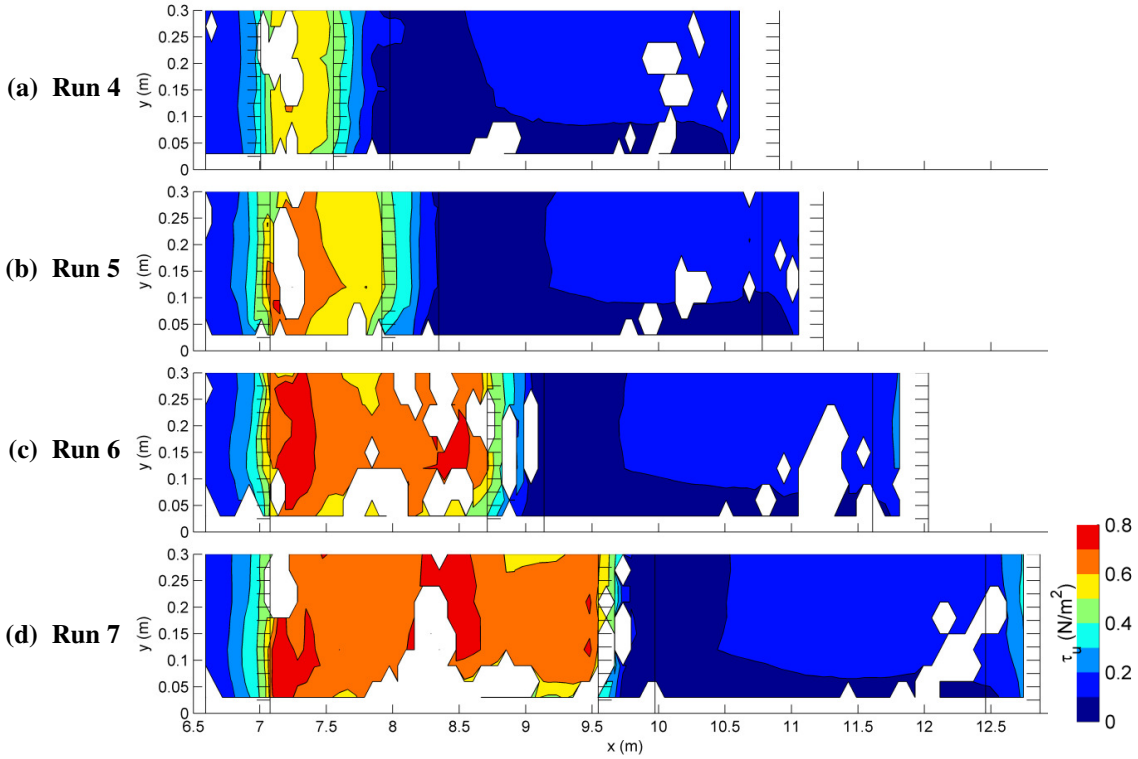

Figure 61. Shear stress based on the velocity profile slope (τ_u) in the XY plane for Runs 4 through 7.

The Π parameter increases in zone III and decreases in zone IV, with the length of zone II having an impact on the magnitude of the parameter (Figure 62). The peak is located near the side wall and its magnitude increases as the velocity exiting zone II increases. It should be noted that Run 5's peak magnitude of Π is thought to be low in Figure 62 as compared to the other runs due to an unknown error that was not resolved in the filtering process.

The Π parameter returns to near zero much quicker near the wall than compared to the centerline as the length of zone II increases (Figure 62). This indicates that although the increase in velocity leaving zone II did not correspond to an increase in magnitude of the wake strength at the centerline, it does correspond to an increase in distribution of elevated wake strength downstream. Overall, there in an increasing lateral gradient at the end of zone IV.

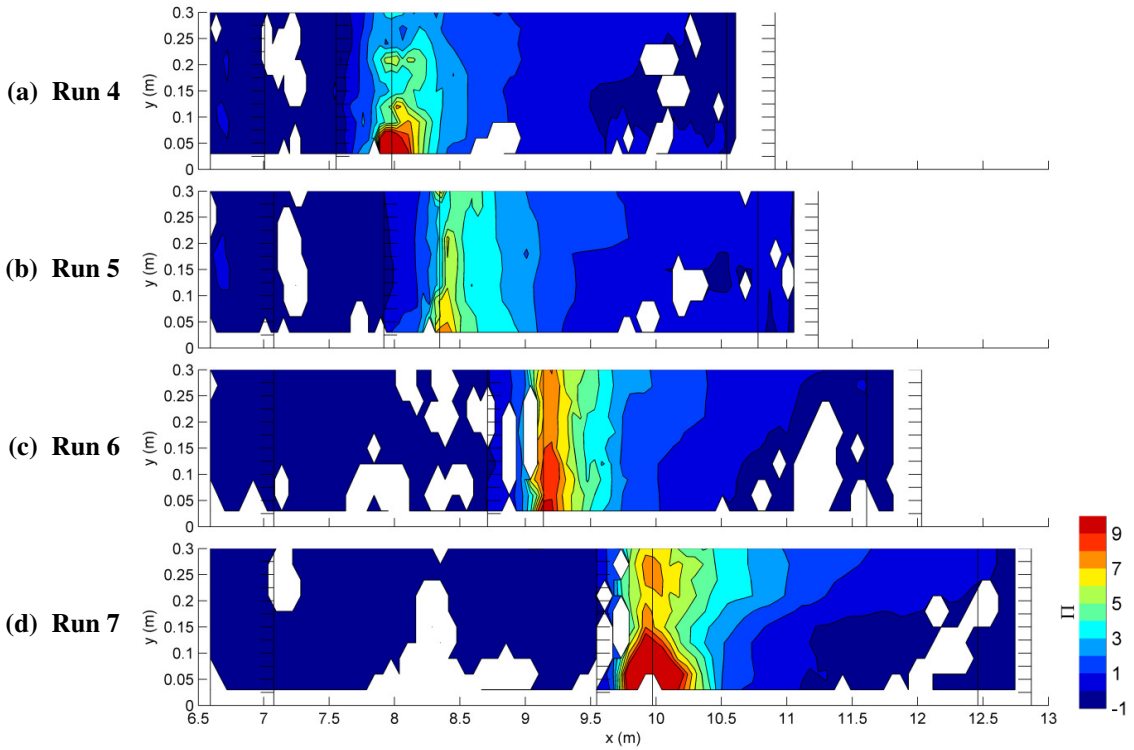

Figure 62. Coles' wake parameter (Π) in the XY plane for Runs 4 through 7.

4.2.2 Secondary Circulation

The vertical velocity measured as the riffle length increases show similar patterns as to those observed as the pool length increases. The vertical velocities are strongly positive in zone I and slightly negative in zone III (Figure 63). The key difference is that zone III's negative velocities are strong in Run 4, but as the length of zone II increases, the magnitude of the negative velocities decreases in zone III. The vertical velocity along the length of zone II indicates slightly positive velocities towards the end of zone II as the zone length increases. At the end of zone IV, the area of positive vertical velocity near the bed increases as the length of zone II increases.

The vertical velocity near the channel wall shows negative velocities in zone III (Figure 64), which is similar to the previous results. The vertical velocity profiles over zone II show slightly negative vertical movement as compared to the slightly positive movement at the channel centerline. The vertical velocity near the water surface in zone IV near the channel wall is consistently slightly positive, while near the bed the velocity is slightly negative (Figure 64), which is consistent with the previous results.

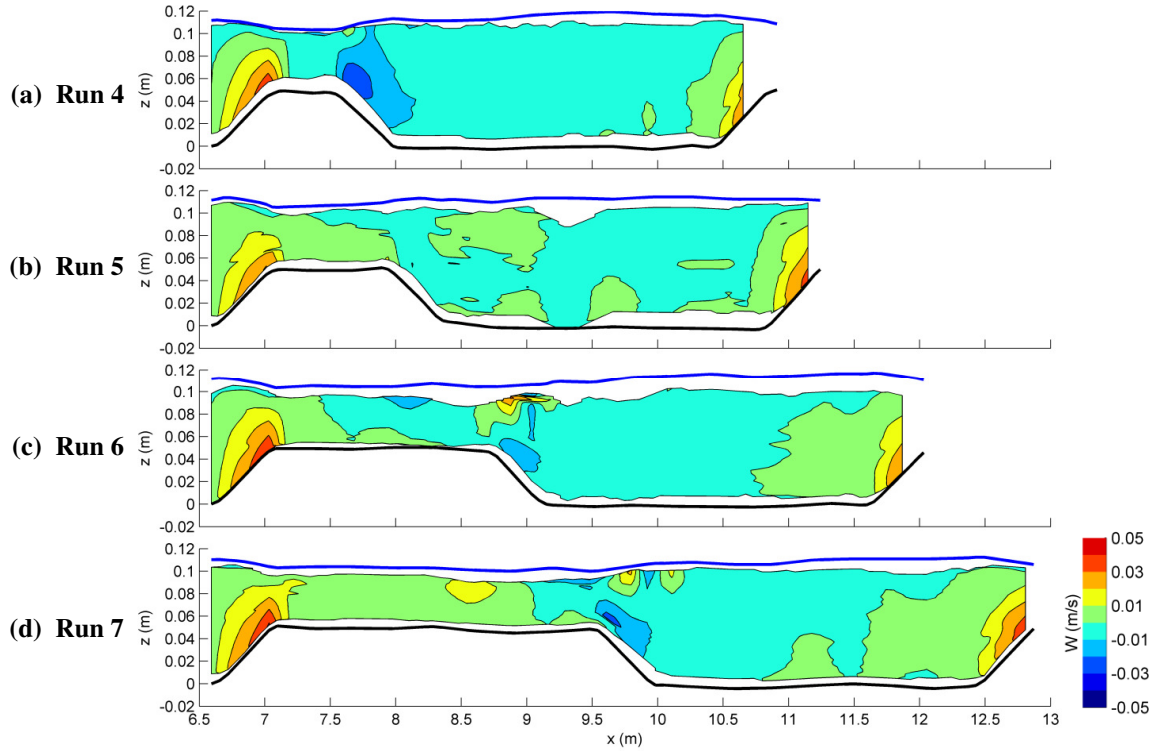

Figure 63. Mean vertical velocity (W) in the XZ plane at the channel centerline (y=0.30 m) for Runs 4 through 7.

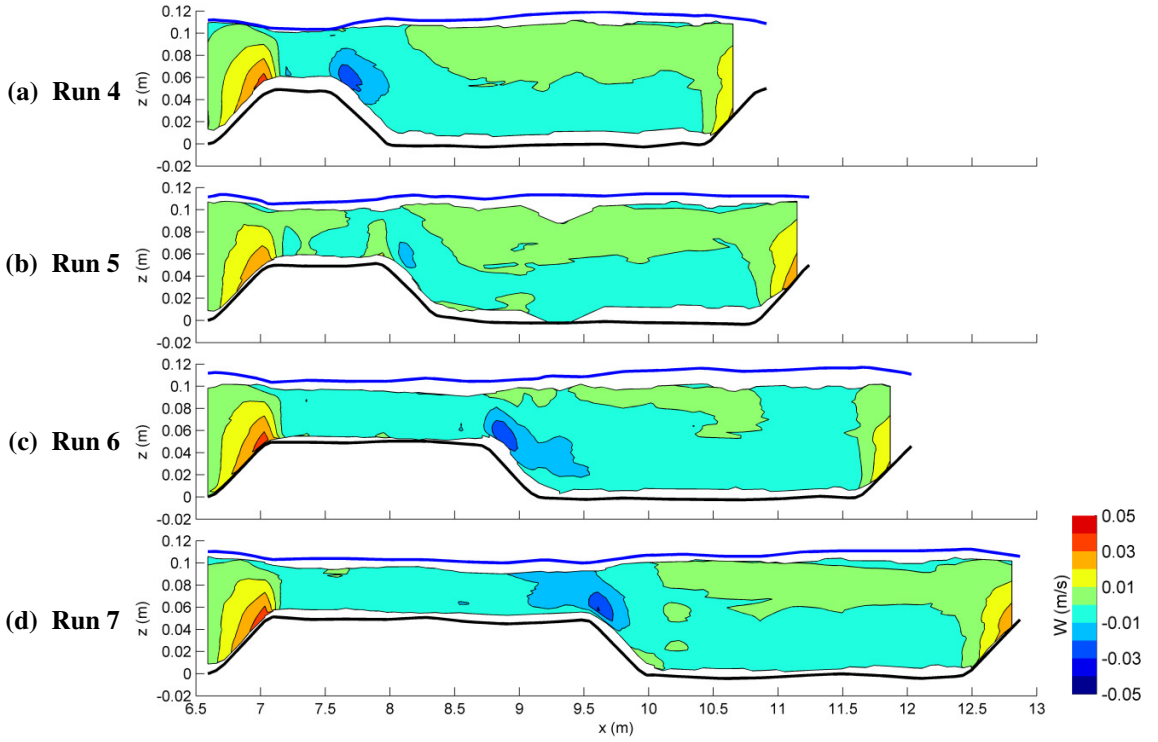

Figure 64. Mean vertical velocity (W) in the XZ plane near the channel wall (y=0.03 m) for Runs 4 through 7.

At the start of zone IV, the vertical velocity in all runs has an overall positive trend near the wall and centerline with a negative trend in between (Figure 65). At the middle and end of zone IV, the overall vertical trend is positive near the bed and side walls, with a negative trend sloping from the water surface near the channel centerline to the bed surface near the channel wall. The magnitude of the positive vertical velocity near the wall decreases as the length of zone II increases.

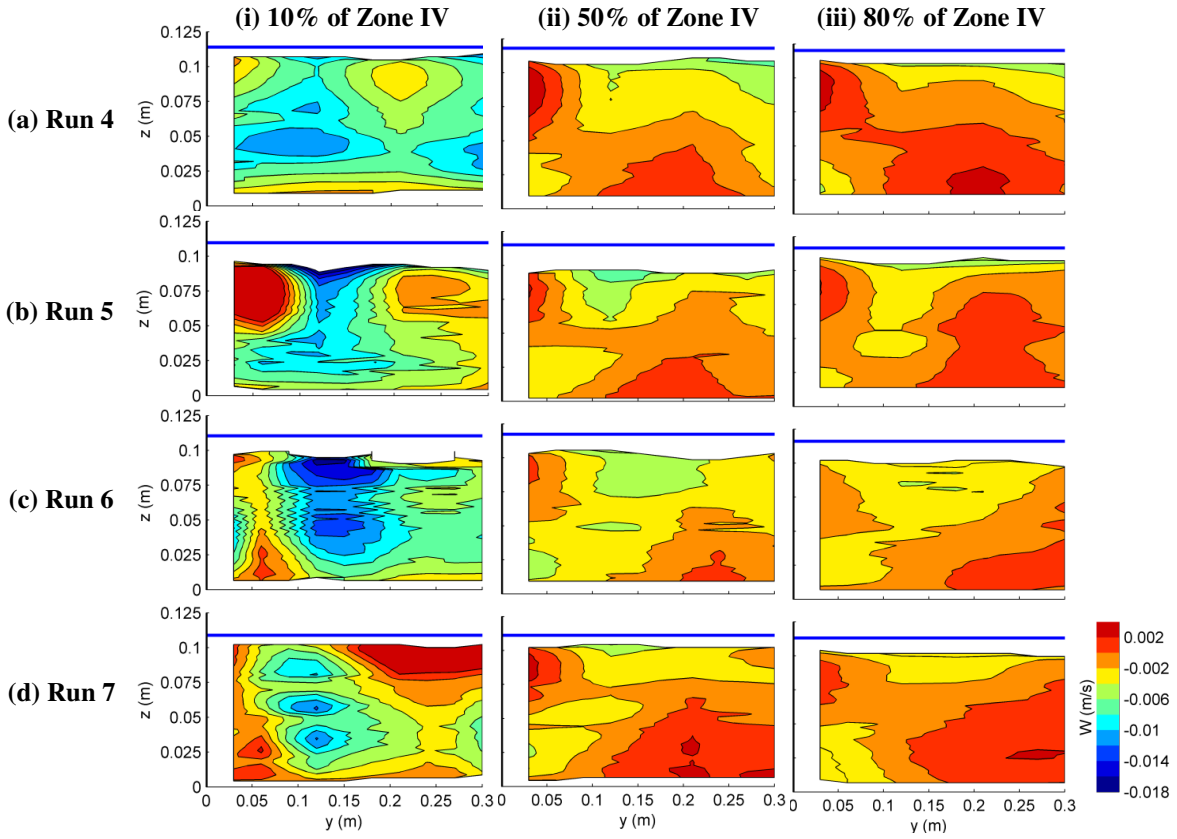

Figure 65. Mean vertical velocity (W) in the YZ plane for Runs 4 through 7 at 10%, 50%, and 80% of zone IV.

4.2.3 Distribution of Turbulence

Turbulence is generated at the flow expansion in zone III and along the length of the riffle near the bed (Figure 66). The Reynolds stress in zone II increases along the bed as the length of zone II increases, however, the stress near the water surface stays near zero in all runs. The extent of high Reynolds stress in zone IV increases to extend the entire length of zone IV as the length of zone II increases, however, the magnitude of this stress is similar in all runs.

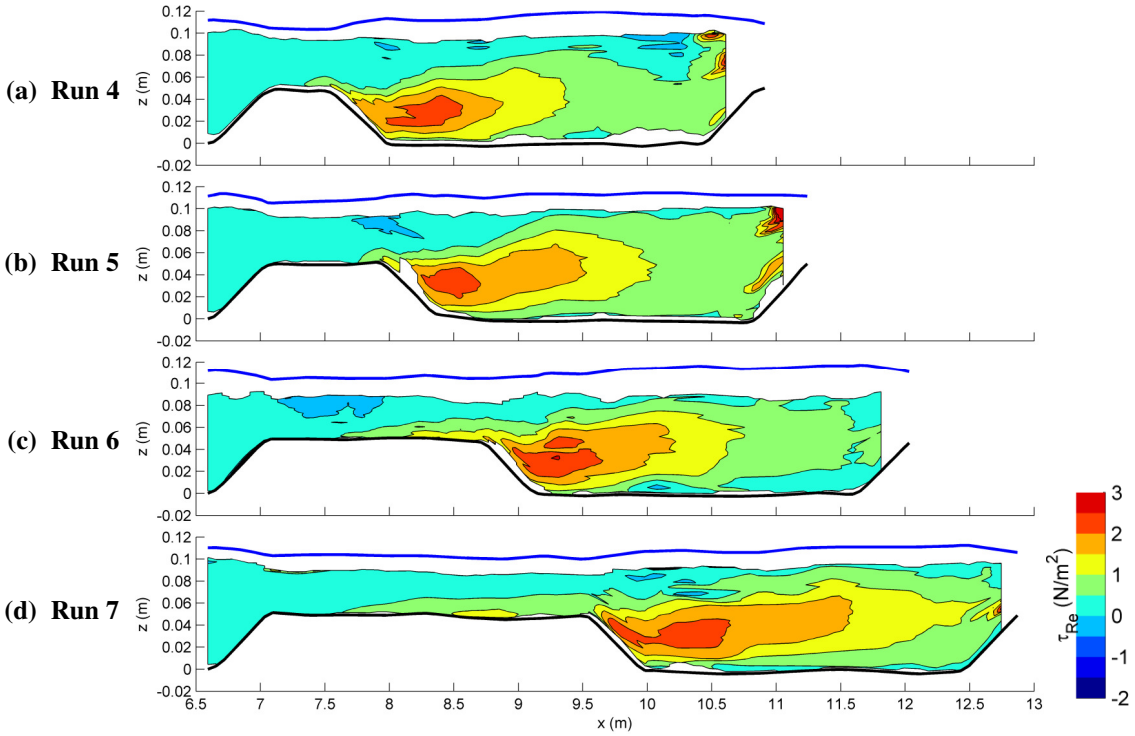

Figure 66. Reynolds stress (τ_{Re}) in the XZ plane at the channel centerline (y=0.30 m) for Runs 4 through 7.

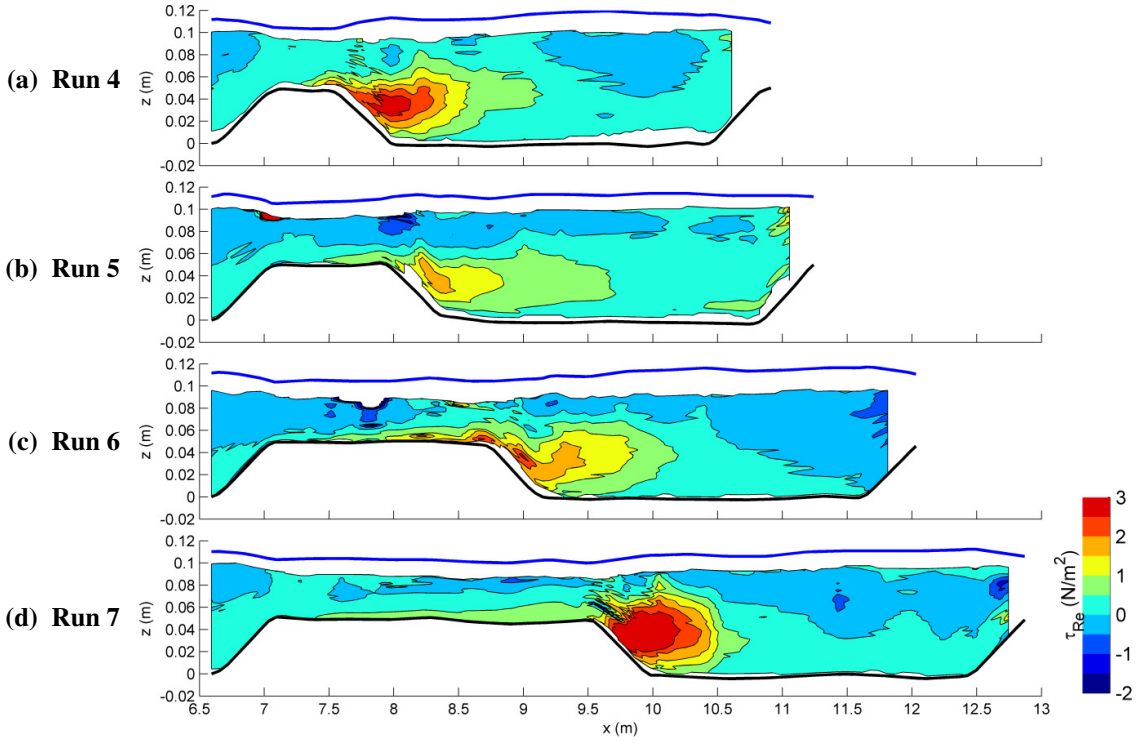

Figure 67. Reynolds stress (τ_{Re}) in the XZ plane near the channel wall (y=0.03 m) for Runs 4 through 7.

The extent of the distribution of the Reynolds stress into zone IV is less near the side wall than at the channel centerline (Figure 67). The distribution of stress near the wall is similar in all runs, even though the lengths of zone II are different. The magnitude of the Reynolds stress is greater near the side wall than at the channel centerline. The peak magnitude of Reynolds stress in Runs 5 and 6 are thought to be a low due to an unknown error. An area of negative Reynolds stress is observed at the end of zone IV in all runs.

At the beginning of the pool, the Reynolds stress is high at the near-bed surface in all runs (Figure 68). The peak magnitude decreases as the flow moves through zone IV and shifts towards the channel centerline. By the end of zone IV, all runs show the diagonal Reynolds stress cross-section, indicating that they have all reached a more uniform state (Nezu and Nakawaga, 1993). Runs 6 and 7 still show relatively high shear stress near the channel centerline than the other runs.

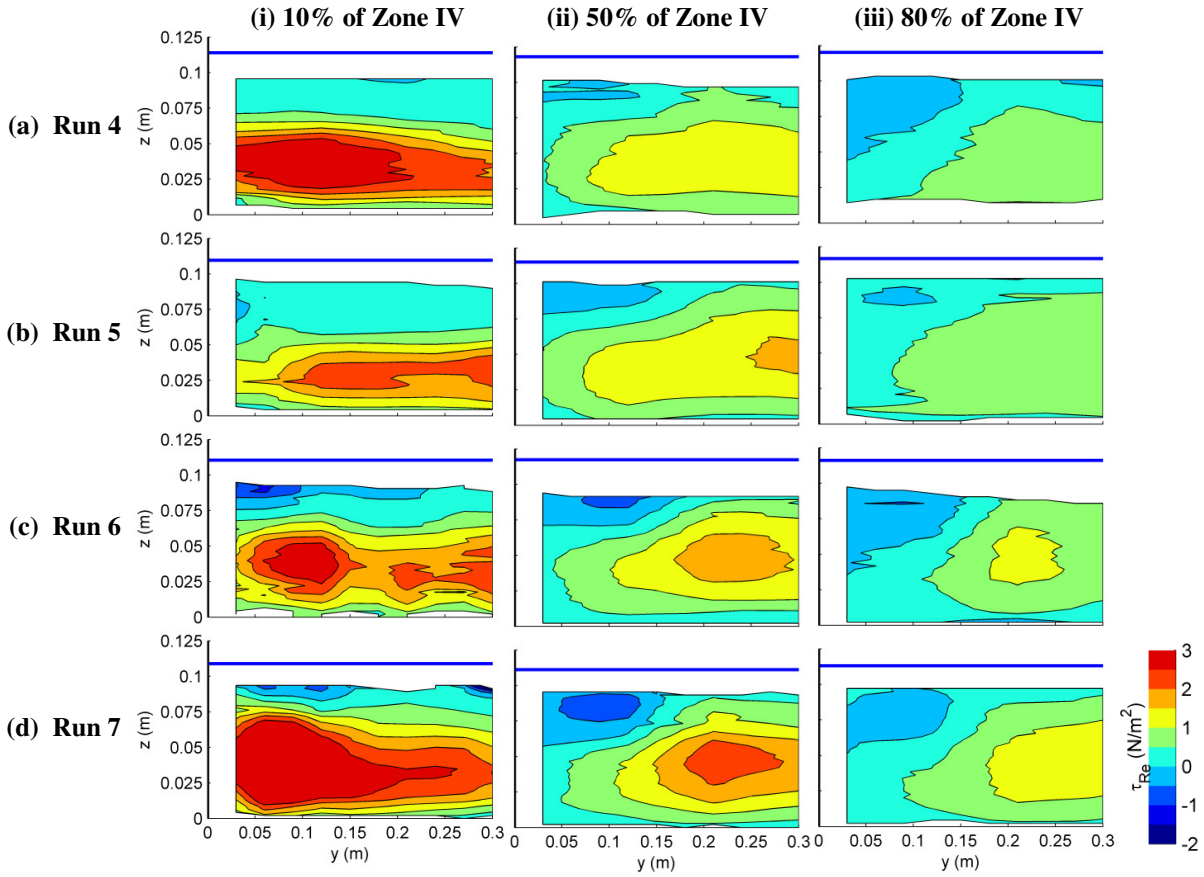

Figure 68. Reynolds stress (τ_{Re}) in the YZ plane for Runs 4 through 7 at 10%, 50%, and 80% of zone IV.

The Reynolds stress profile shows high values near the bed and low values near the water surface at the start of zone IV (Figure 69). Near the centerline, the Reynolds stress is similar in all runs, however,

near the channel wall, higher levels of Reynolds stress occur, particularly in Run 7. The irregularities of the Reynolds stress profile near the wall may be related to the lateral position of the high stress cells for the different channel geometries.

At the channel centerline, the Reynolds stress profiles at the end of zone IV are slight variations of convex shapes in all runs (Figure 69aiii). At this location, higher overall magnitudes of Reynolds stress are seen in Run 7, with the peak located at the vertical midpoint, while the other runs peak closer to the bed. This indicates that the flow in Run 7 is still decelerating while the flow in the other runs is closer to uniform flow. The Reynolds stress profile near the channel wall indicates a slightly negative profile near the water surface (Figure 69biii). This negative stress is attributed to the uniform flow cross-section of Reynolds stress observed in Figure 68iii.

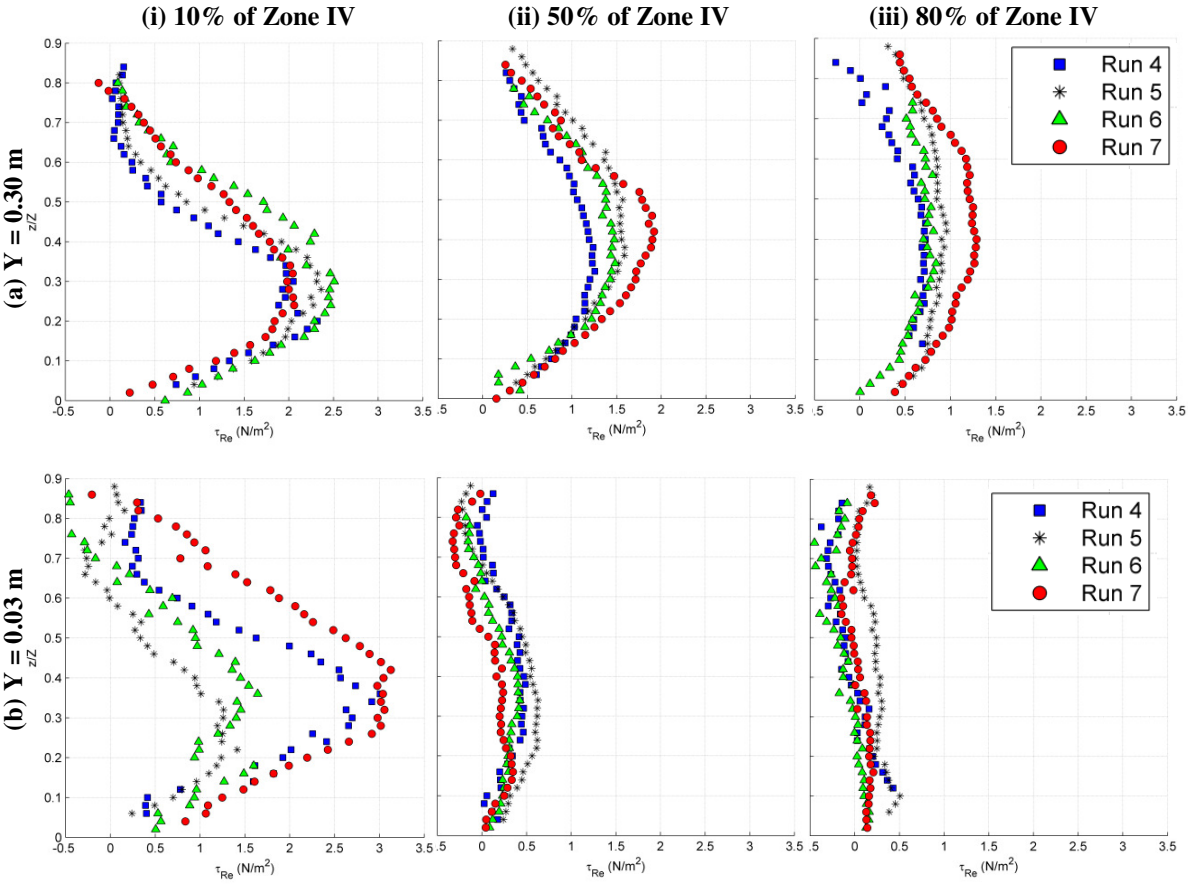

Figure 69. Reynolds stress (τ_{Re}) profiles for Runs 4 through 7 at 10%, 50% and 80% of zone IV at y = 0.30 m and 0.03 m.

The shear stress estimated from the Reynolds stress increases along zone II and III (Figure 70). The peak shear stress occurs in zone III, and corresponds to the peak in the Reynolds stress. The shear

stress in zone II is related to the increase in Reynolds stress observed near the bed. The Reynolds stress decreases in zone IV, but remains slightly elevated throughout the entire length of the zone. Overall, the Reynolds stress is low near the wall and high near the channel centerline in zone IV.

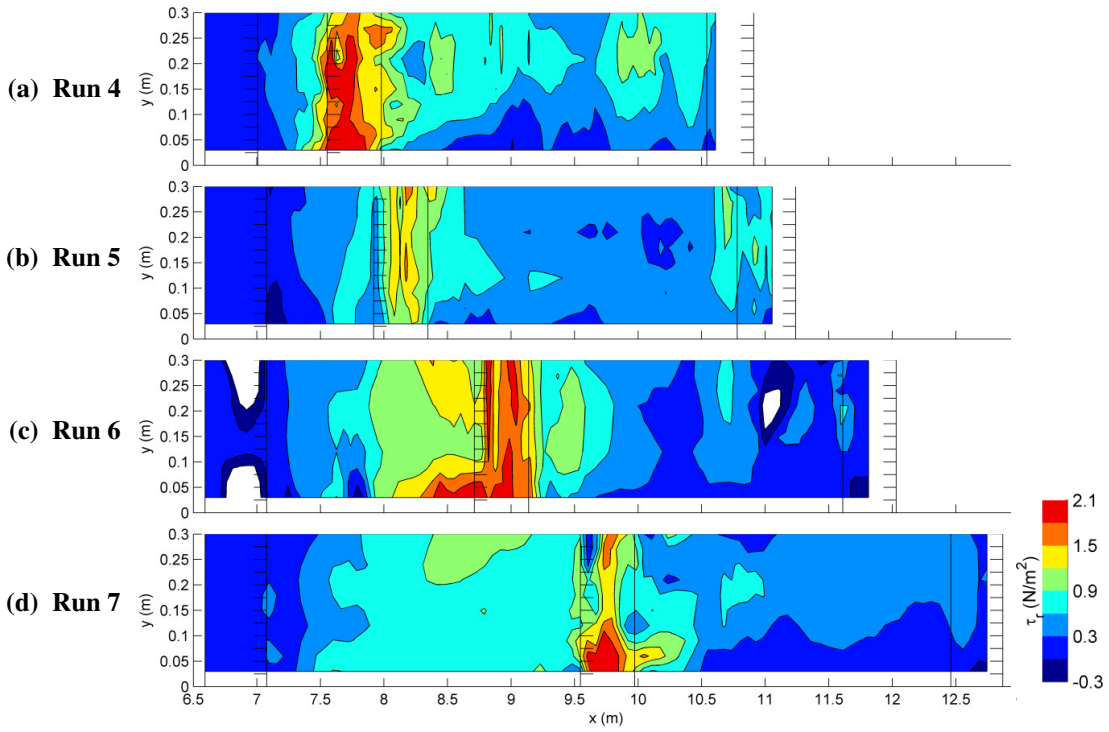

Figure 70. Shear stress estimated from the Reynolds stress profile (τ_r) in the XY plane for Runs 4 through 7.

Similar to the results from increasing the pool length, low ITS values are observed at the channel centerline in all runs, and are not shown in these results (see Appendix C). At the channel wall, an increasing trend of coherence as the riffle length increases is found in zone III (Figure 71). This increase is attributed to the slow moving bed velocities observed in zone III compared to the faster moving surface velocities. While the ITS coherence along zone II remains very low, higher ITS values are more common in zone IV as the length of zone II increases (Figure 71).

Similar ILS results are observed as the riffle length increases as compared to the results of the pool length increasing (Figure 72). Although the length of zone II increases, there is little difference in magnitude and shape of the elevated coherence in the different runs. The peak coherence in zone IV is generally located near the end of the section. Similar magnitudes of coherence are measured over the length of zone II for each run even though the length increases. The coherence near the side wall is very similar to that at the centerline, only with smaller magnitudes, and therefore is not shown in these results but can be found in Appendix C.

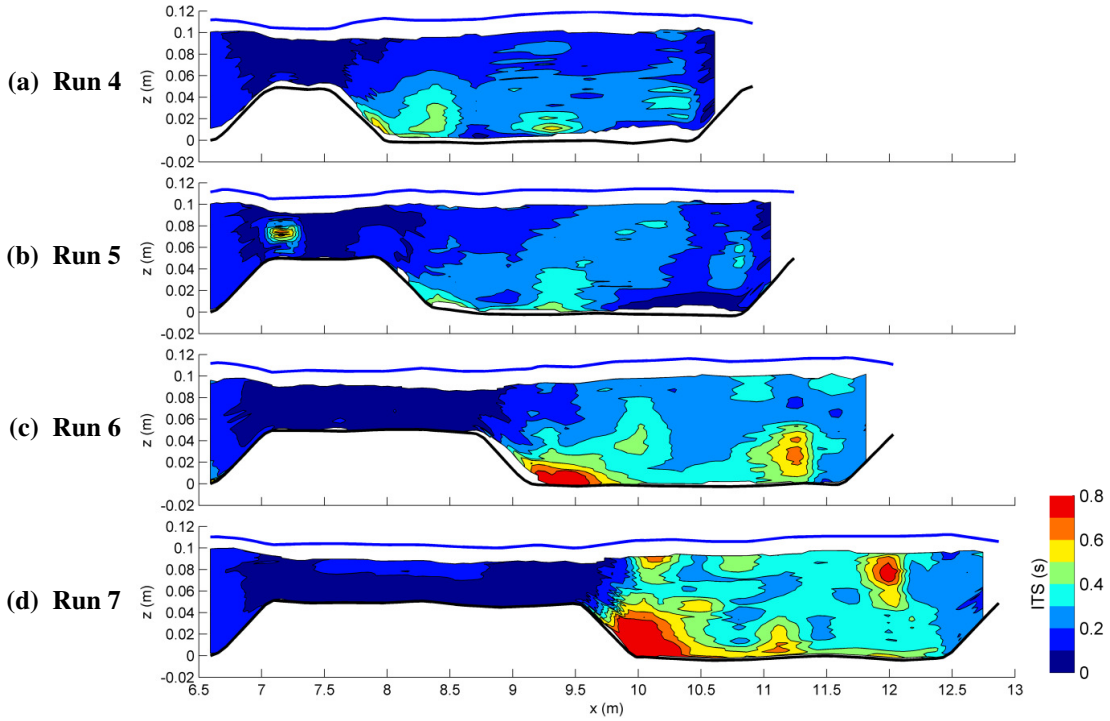

Figure 71. Integral time scale (ITS) in the XZ plane near the channel wall (y=0.03 m) for Runs 4 through 7 using the US probe.

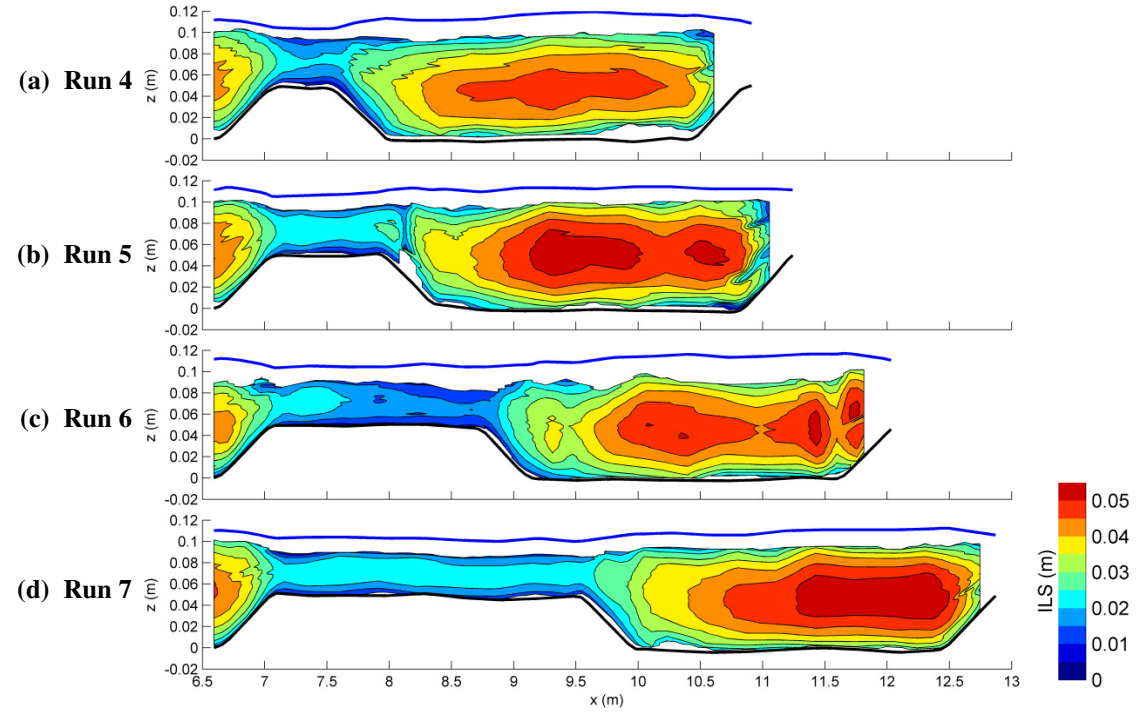

Figure 72. Integral length scale (ILS) in the XZ plane at the channel centerline (y=0.30 m) for Runs 4 through 7 using the US probe.

4.3 Other Results

To be thorough, two extra parameters were tested during the experimental phase, the effect of water depth and the effect of roughness. Complete details of these two testing methods and results can be found in Appendix D and Appendix E. In general, the results observed from these two parameters were expected, as they followed similar patterns as changing the pool and riffle length. There were some key differences, however, which are discussed below.

4.3.1 Results from Changing the Water Depth

Overall, the streamwise velocity and the Reynolds stress decreases as the water depth increases, which is expected. The first noticeable difference is observed in the turbulent coherence. At the channel centerline, the ILS increases significantly in zone II and zone IV as the water depth increases (Figure 73). These areas correspond to low Reynolds stress and slower velocities. Although the ILS coherence increases near the channel centerline, the coherence values remain low near the channel wall (Figure 74).

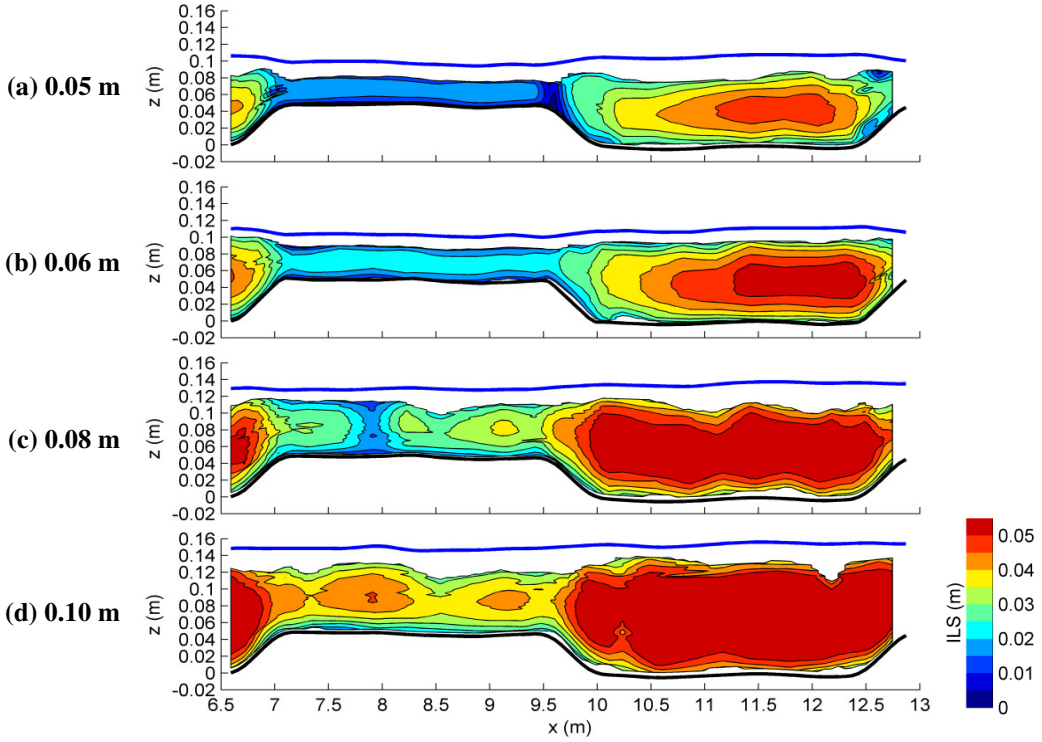

Figure 73. Integral length scale (ILS) in the XZ plane at the channel centerline (y=0.30 m) for four different depths using the US probe.

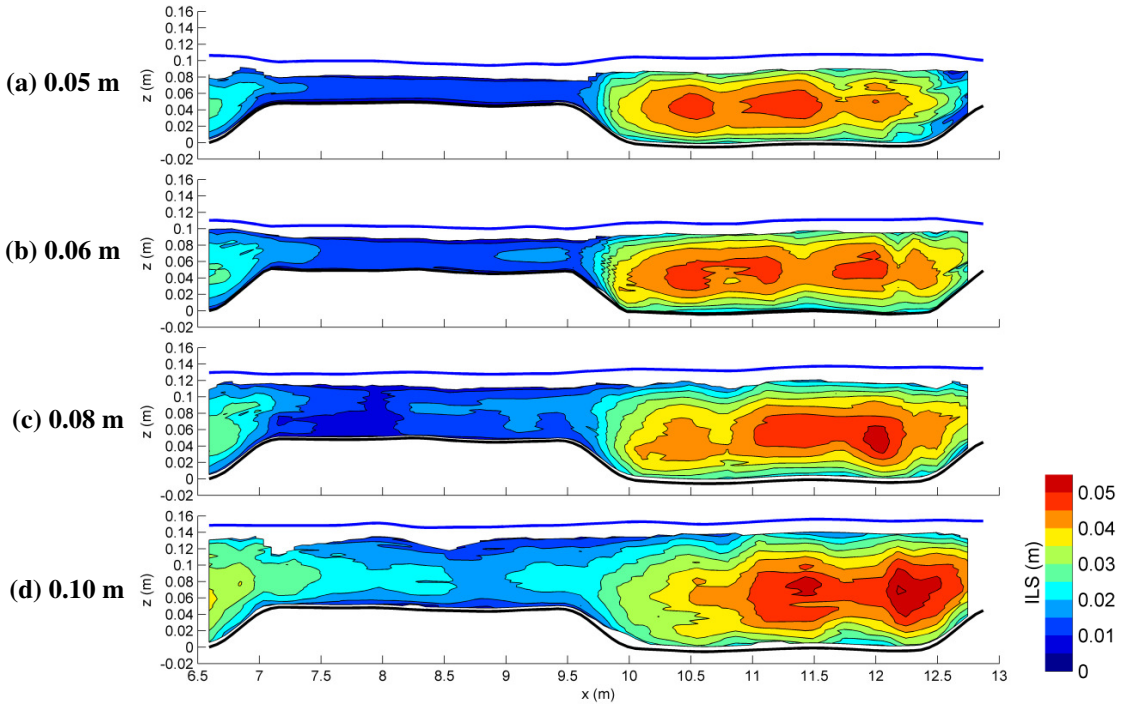

Figure 74. Integral length scale (ILS) in the XZ plane near the channel wall (y=0.03 m) for four different depths using the US probe.

At the channel centerline, the ITS becomes more coherent as the water depth increases, especally in zone IV (Figure 75). There are also some coherent trends observed in zone II. Both of these areas previously showed no consistent trend when changing the riffle or pool length.

Near the channel wall, the coherence trend near the bed in zone III decreases as the water depth increases (Figure 76). This pocket of coherence had previously increased in both the increase in riffle and increase in pool length. The overall ITS coherence seems to slightly increase over zone II and decrease in zone IV as the water depth increases.

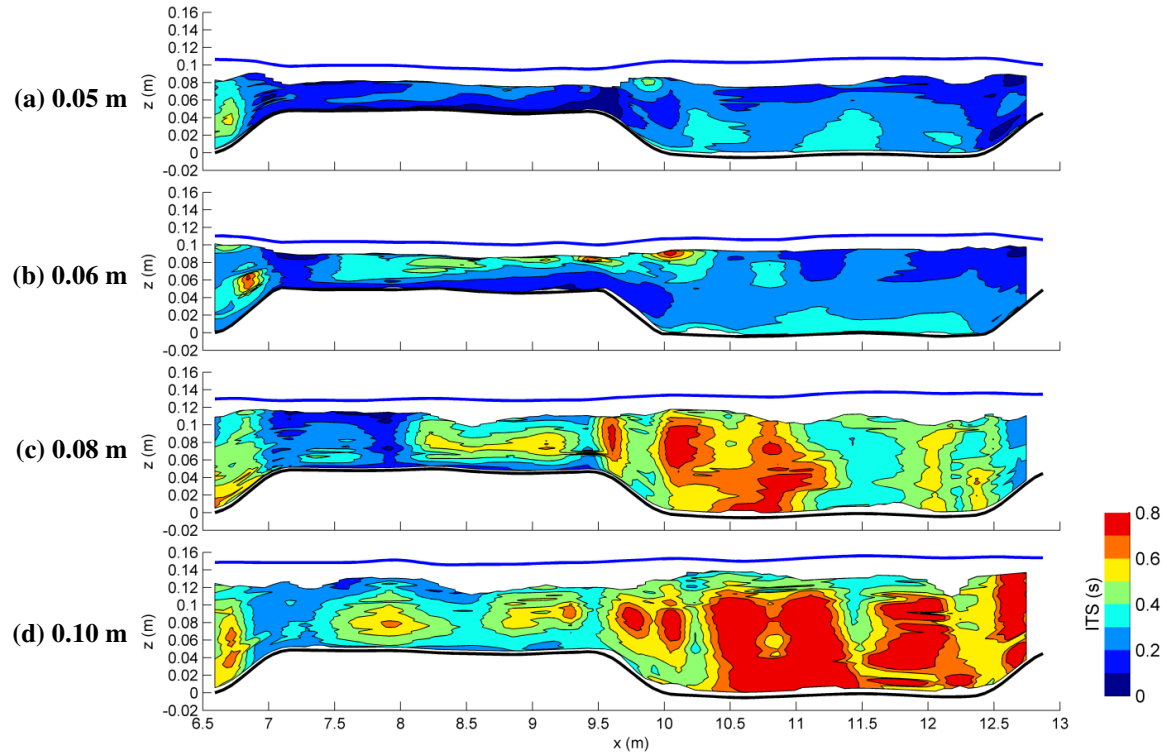

Figure 75. Integral time scale (ITS) in the XZ plane at the channel centerline (y=0.30 m) for four different depths the US probe.

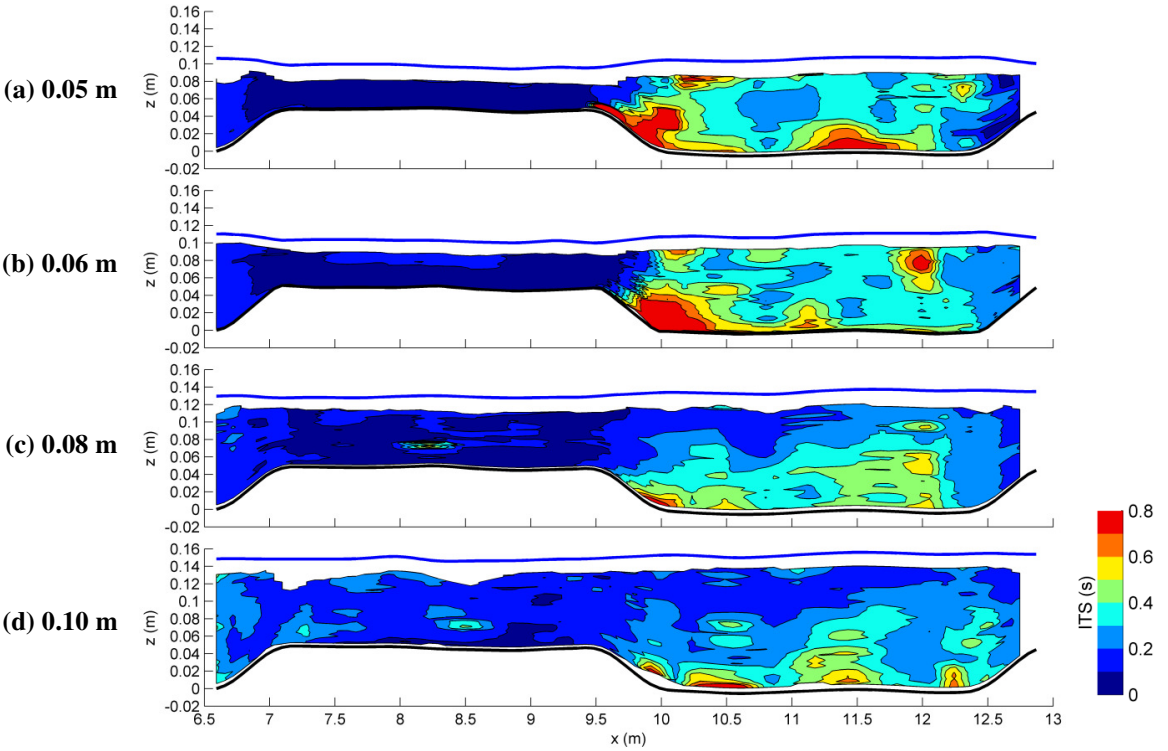

Figure 76. Integral time scale (ITS) in the XZ plane near the channel wall (y=0.03 m) for four different depths using the US probe.

4.3.2 Results from Changing the Wall and Bed Roughness

Overall, the streamwise velocity and Reynolds stress increase as the roughness factors increase. The shear stress estimated from the velocity profile slightly decreases in zone II as the roughness increases, and increases near the centerline in zone IV (Figure 106). Similar peaks in shear stress in zone II can be seen at the start of the riffle at x = 7 m and at x = 8 to 8.5 m.

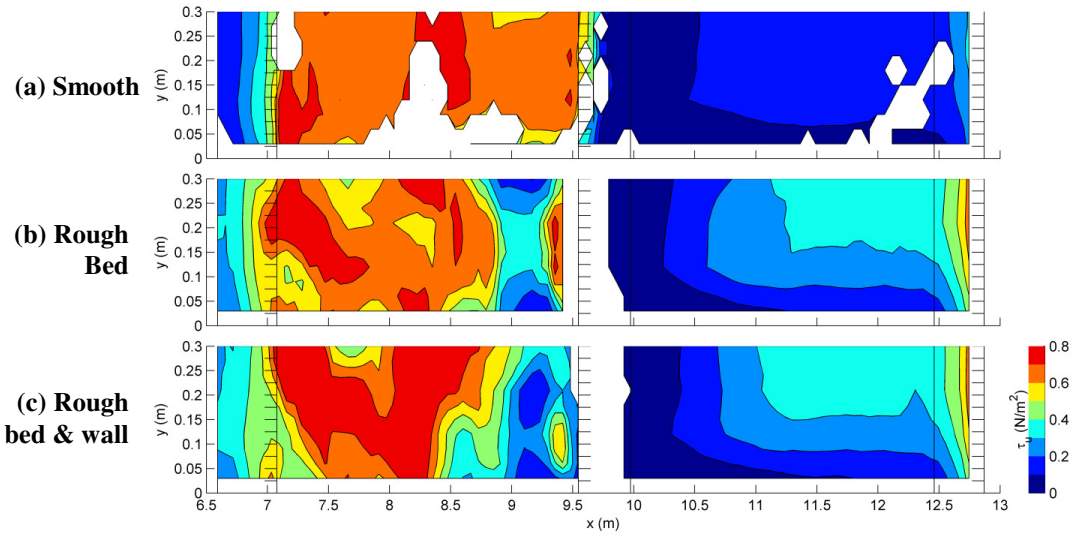

Figure 77. Shear stress estimated from the velocity profile (τ_u) in the XY plane for different roughness factors.

The Π parameter increases as the roughness factors increase (Figure 78). The peak Π value extends the entire width of the channel as the channel surfaces become more rough. This peak had previously been located near the wall in all of the smooth surface runs. The Π value increases in zone II, and in zone IV, the Π value does not return to near zero at the wall when both the wall and bed are rough.

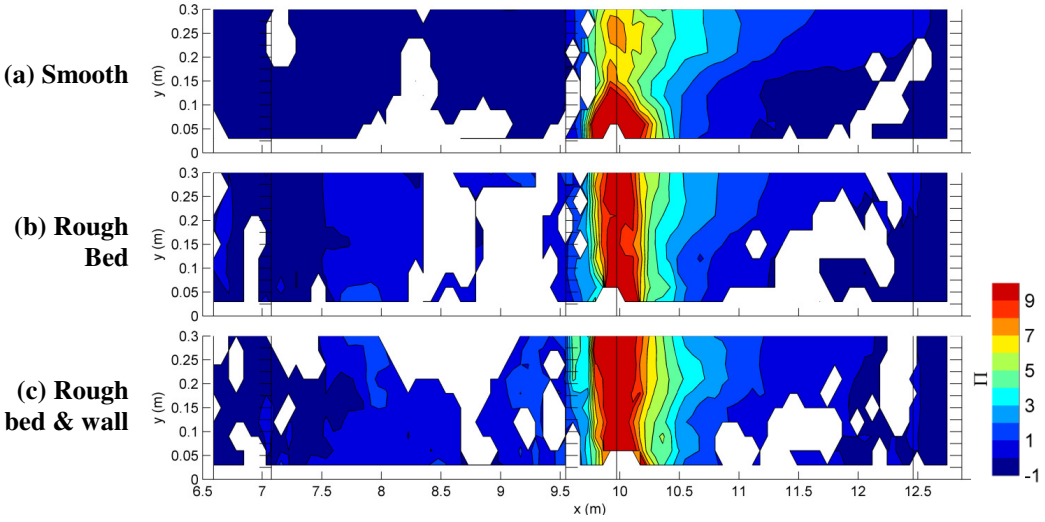

Figure 78. Coles' wake parameter (Π) in the XY plane for different roughness factors.

Chapter 5

DISCUSSION

This section discusses the suitability of the experiments in the flume for considering the effect that changing the pool and riffle lengths has on the hydrodynamics of the flow. The results of the experiment are then discussed in terms of how the bedform geometry can push the distribution of flow and turbulence both away from and towards what is expected in uniform flow. The effect that shear stress plays on the stability of the bedforms, as well as a discussion on the coherence of the turbulence in the system, are also presented. Previous field, laboratory, and numerical studies are compared to the results of this research. The overall fundamental control that scale has on hydrodynamics is outlined, and recommendations for future research due to the limitations of this study are discussed.

5.1 Suitability of the Experimental Apparatus

The results presented in the previous chapter have all been obtained from tests conducted in a laboratory flume. Conducting the research in a flume makes it possible to reduce the total number of system variables so that a more controlled experiment can be conducted, however, the appropriateness of the techniques and results must be considered. Looking at both the repeatability of the measured data upstream of the bedforms, as well as the effect of other more typical conditions has on the measurements can be used to consider the appropriateness of the techniques used in this thesis.

When only the pool length is varied (Runs 1 to 4), the upstream location includes both the initial contraction and the riffle, or zones I and II. In the side view orientations both in the center of the channel and near the wall, it was seen that both the streamwise and vertical velocities over these sections are very similar in Runs 1 through 4. As the riffle length is varied (Runs 4 to 7), the only consistent upstream location is the contraction section leading into the riffle. Once again, the streamwise and vertical velocities at the centerline and near the wall show that the flow is similar leading into the riffle in these four runs. The similarity of the upstream flow demonstrates the repeatability of the flume conditions, and the appropriateness of using the flume to examine the flow conditions of a pool-riffle in a straight channel with non-deformable boundaries.

The effects that depth and roughness have on the hydrodynamics of the flow were also considered. Overall, the depth and roughness introduced a new balance between stresses at the centerline and side

wall, as seen in the turbulence production, turbulent coherence, and deviation from uniform flow. These additional factors demonstrate the complexity of the underlying process of convective acceleration and deceleration in an open channel. Because of this complexity, experiments with geometries that would be more representative of the natural pool-riffle form would be difficult, it was concluded that the effect of bedform length on pool-riffle hydrodynamics is most clearly observed when it is isolated in an experimental flume with a smooth straight bedform configuration, as was used in this research.

5.2 Comparison to Previous Studies

The results from this research were compared to previous studies in order to determine if the flow conditions created in the flume were reasonable when compared to those conditions observed in the field and in previous laboratory and numerical modeling. The streamwise velocity results are similar to previous studies as it was found that at the pool head, the flow converged towards the centerline as previously observed (MacVicar and Roy, 2007a; Clifford and Richards, 1992; MacWilliams et al., 2006), and by the end of the pool the flow profile became fuller by extending similar velocities across the entire cross-section (MacVicar and Roy, 2007a).

The Π parameter agreed well with previous studies. The magnitude of the Π parameter near the centerline was within the range of $\Pi \approx 3$ to 7, which was similar to the results of MacVicar and Rennie (in review), where $\Pi \approx 4$, however, $\Pi = 0.41$ in the study by Kironoto and Graf (1995). The difference between the results of this research and that presented by Kironto and Graf (1995) can be explained as the latter used a much milder expansion section (slope > 1%). The magnitude of the Π parameter near the channel wall was slightly higher in this study, where $\Pi > 9$, as compared to the study completed by MacVicar and Rennie (in review) where $\Pi \approx 7$.

The profile of turbulence as expressed by the Reynolds stress followed that of previous research, as the peak turbulence occurred at the flow expansion, and decreases as it moves downstream. This initial area of high turbulence corresponds to previous studies (MacVicar and Roy, 2007a; Clifford 1993b; Clifford, 1996). The fact that as the flow decelerates in the pool, the Reynolds stress occurs at a distance away from the bed, has also been found in previous studies (Simpson, 1989; Yang and Chow, 2008; MacVicar and Rennie, in review).

The shear stress based on the velocity profile increases in accelerating flow and decreases in decelerating flow, which is consistent with previous results (MacVicar and Rennie, in review; Kironoto and Graf, 1995; Song and Chiew, 2001; Yang and Chow, 2008). The increase in shear stress through the middle of the pool with an increasing lateral gradient is similar to the results of MacVicar and

Rennie (in review). The results of the shear stress estimated from the Reynolds stress profile showed an increase during the flow expansion, which is consistent with previous results (MacVicar and Roy, 2007a; MacVicar and Rennie, in review).

The coherence structures measured in this study compared to those from previous experiments were similar for the ITS but different for the ILS. Similar to the ITS results presented in this thesis, MacVicar and Roy (2007b) found short random pockets of ITS coherence near the bed in the pool with no overall trend. However, they found negligible levels of ILS coherence through the pool, while in this research the pool was characterized by significant ILS coherence.

5.3 Adjustment to Uniform Flow

As the flow moves over the bedform, kinetic energy is first generated as the velocity increases over the riffle, and then dissipated as it expands and slows into the pool. During this increase and decrease of kinetic energy, non-uniform flow conditions are created. In order for the flow to recover to a uniform flow state, a sufficient pool length is required. Once the flow has reached uniform flow, the flow will remain in this state until a new non-uniform flow element (riffle) is introduced. In these experiments, a transition from non-uniform flow to uniform flow towards the end of the pool was clearly seen as the pool length increased, as shown in the streamwise velocity, Π, vertical velocity, and the Reynolds stress results.

When the flow transitions from the riffle to the pool, there is a high velocity core near the water surface and centerline in the channel. As the pool length increases, this high velocity core expands to a slower and fuller cross-section of flow. The fact that the velocity is nearly the same at all locations in the cross-section, even near the side walls and bed of the channel, suggests that the flow is adjusting to a more uniform state by the end of the pool at increased pool lengths.

As the pool length increases, the Π parameter in the pool decreases so that the value of Π in Run 4 at the end of the pool is near zero (Figure 79). Note that Π has been smoothed by a running average over the five nearest points and that the total length has been normalized by the different zones. When the pool length is short, the magnitude of Π is still elevated at the end of the pool, as in Run 1 where Π approximately equals 2 by the end of the pool. This indicates that the velocity profile in a short pool is still being influenced by the relatively high near surface velocities. As the pool length increases, the near water surface velocities decrease towards the end of the pool, allowing the velocity profile to become more logarithmic, and the Π value to return to near zero, like in Run 4. Overall, as the value of Π decreases the flow uniformity increases, as the Π value is a measure of the deviation of the flow away from the log-law of uniform flow.

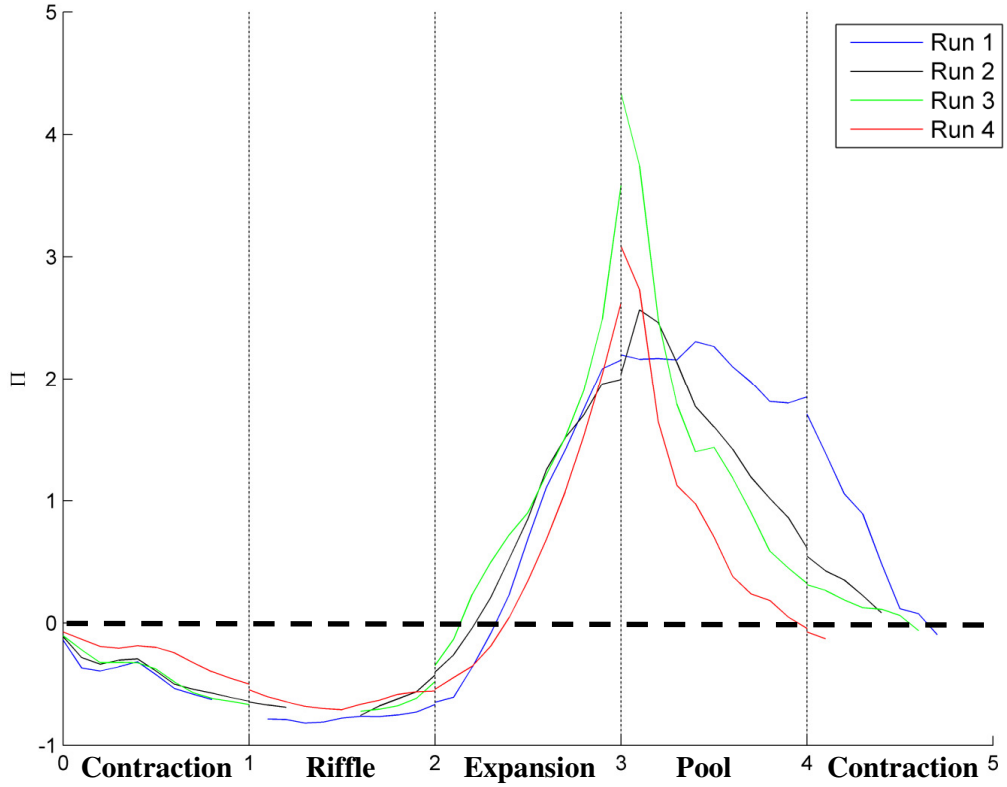

Figure 79. Comparison of the Coles' Wake Parameter (Π) at the channel centerline for Runs 1 through 4 with normalized zones.

As the pool length increases, the cross-sectional profile of secondary currents in the pool adjusts to an expected uniform cross-section in an open channel as measured by Nezu and Nakawaga (1993) (Figure 80). Note that the lateral directions have been assumed from the vertical velocities. In uniform flow, the vertical velocities have positive magnitudes in the pool near the bed and along the side wall. The adjustment to a uniform cross-section again indicates that the pool is sufficiently long enough in Run 3 and 4 to create uniform flow conditions.

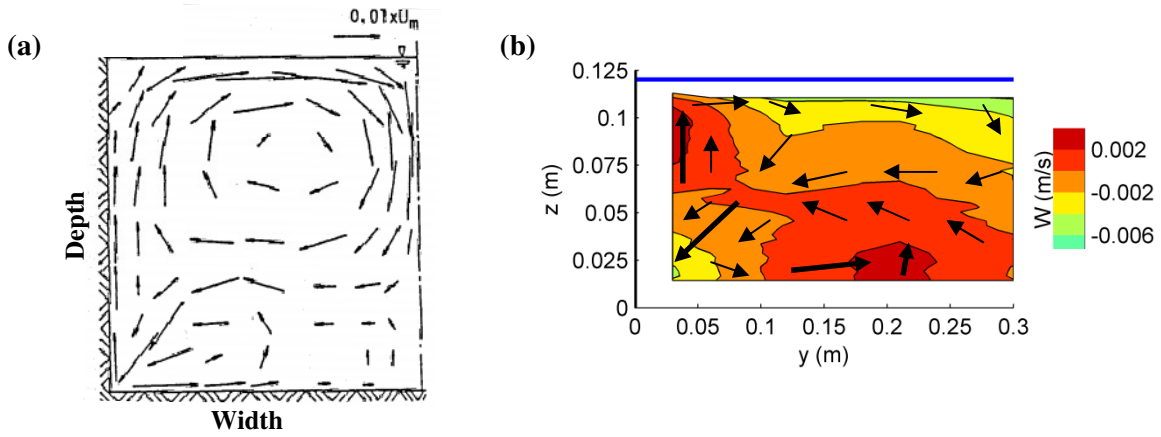

Figure 80. Secondary effects (a) numerically simulated by Nezu and Nakawaga (1993) with an aspect ratio of B/h = 2, and (b) measured at 80% of zone IV (pool) in Run 4.

As the pool length increases, the Reynolds stress cross-sectional profile adjusts to an expected uniform cross-section as measured by Nezu and Nakawaga (1993) (Figure 81). A uniform Reynolds stress has a diagonal transition between negative stress near the wall and surface and the positive stress at the bed. As the pool length increases, the flow adjusts from the high Reynolds stress near the bed to the diagonal shape expected in uniform flow.

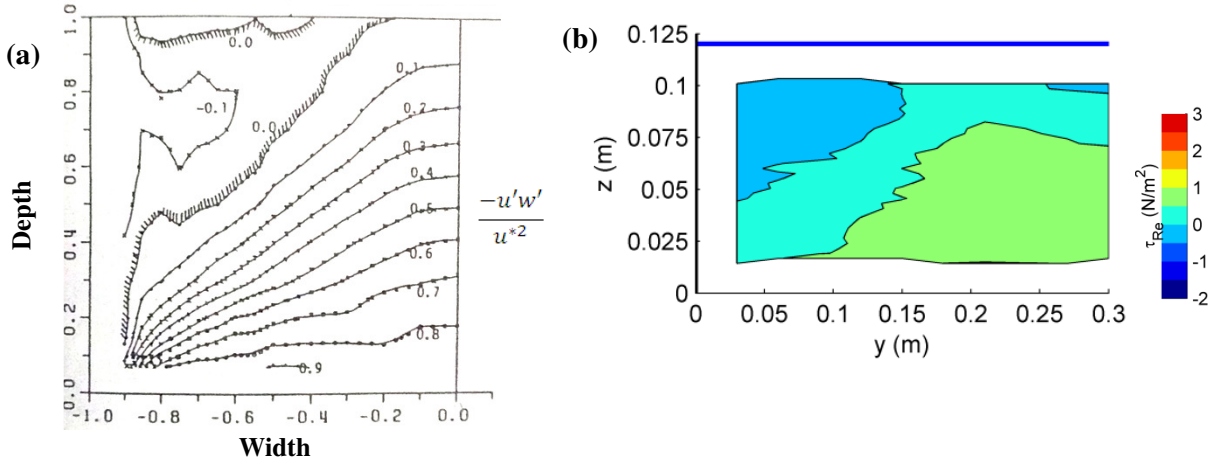

Figure 81. Reynolds stress (a) measured by Nezu and Nakawaga (1993), and (b) measured at 80% of zone IV (pool) in Run 4.

When considering the streamwise velocity, ∏ parameter, vertical velocity, and Reynolds stress towards the end of the pool as the pool length increases, it can be concluded that the flow returns to a uniform state towards the end of the pool if the pool length is long enough. Introducing the riffle causes non-uniform flow until a bedform length ratio (width to total bedform length) of 1:5.0 is reached and the flow is mostly uniform, or a ratio of 1:6.4 is reached where the flow is completely uniform. If the pool

length were to increase past this ratio, the flow would remain uniform, provided that the channel boundary and roughness remain uniform, until it reached some flow-changing element.

5.4 Adjustment Away from Uniform Flow

The riffle length was increased in order to assess how the same pool length dynamics changed with new upstream conditions. As the riffle length increased, the flow adjusted away from a uniform flow state at the end of the pool, which is shown in the results of the streamwise velocity, Π, and the Reynolds stress.

With an increase in riffle length, the streamwise velocity profile near the end of the pool adjusts from having a slow near surface velocity when the riffle is short, to having a faster velocity core near the water surface when the riffle is long. As discussed previously, an increased velocity core with flow occurring over less of the cross-sectional area suggests that the flow is adjusting to a less uniform state by the end of the pool as the riffle length increases. The velocity gradient across the channel width also changes, as there is a relatively rapid change in velocity across the entire cross-section when the riffle length is increased. The increase in velocity gradient again suggests the flow is transitioning to a less stable state.

The faster velocity core at the water surface leads to increasingly higher Π values observed at the end of the pool (Figure 82). This change indicates that the flow is moving from a uniform flow at the end of the pool, like in Run 4 where Π is approximately zero, to a flow with a non-uniform profile, like in Run 7 where Π is approximately 0.5. As mentioned above, a Π value near zero suggests uniform flow, whereas the flow becomes less uniform as Π increases, which is what is occurring as the riffle length increases. As the riffle length continues to increase, the Π values at the end of the pool are likely to keep increasing, and the flow will continue to move towards a more non-uniform flow, unless the pool length increases.

It is interesting to note that the riffle has reached a Π value of zero at the end of the riffle in Run 7, indicating uniform flow was established at this riffle length. This uniform flow that was achieved in the riffle is now more concentrated in a high velocity core and therefore farther away from the uniform flow conditions in the pool. This means that a longer distance is required for the flow to adjust from the uniform conditions of the riffle to the uniform conditions dictated by the pool.

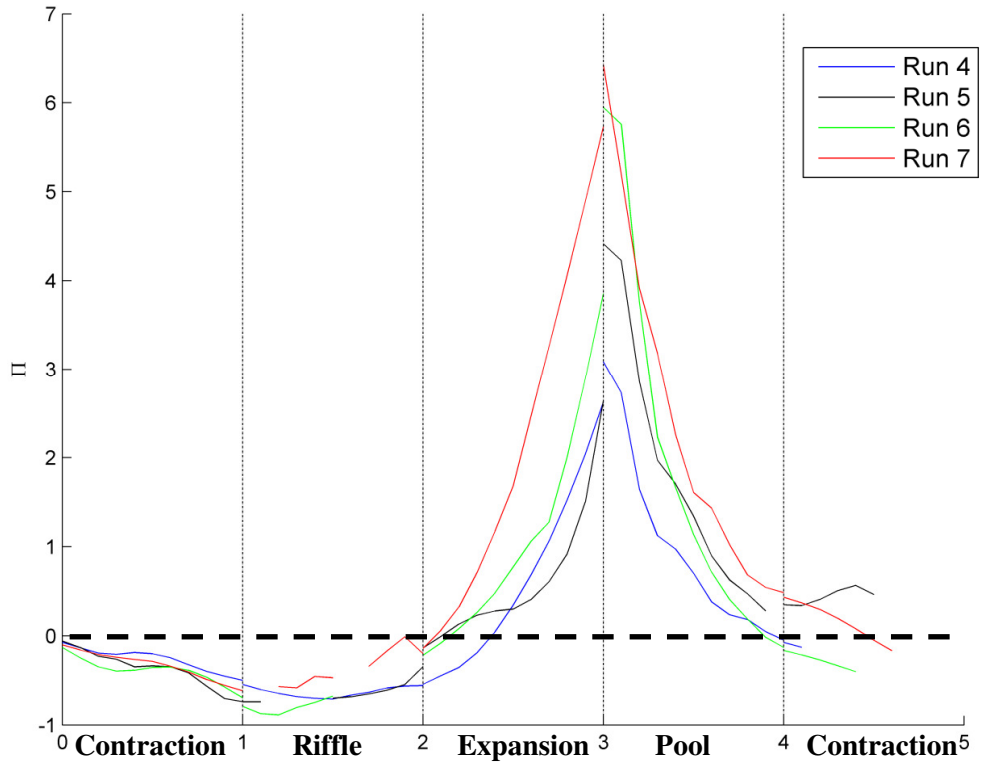

Figure 82. Comparison of the Coles' Wake Parameter (Π) at the channel centerline for Runs 4 through 7 with normalized zones.

As the riffle length increases, the area of elevated Reynolds stress extends farther into the pool. With this increase in elevated Reynolds stress at the end of the pool, the flow cannot transition to a uniform state as it could when the riffle length was shorter. The YZ orientation of the Reynolds stress shows the contours moving from the uniform low stress diagonal cross-section observed in Run 4, to a cross-section with a higher peak near the channel centerline, as in Run 7. This confirms that the flow is not uniform at the end of the pool in the tests with increased riffle length.

The results of the streamwise velocity, Π parameter, and Reynolds stress profiles near the end of the pool as the riffle length increases, as discussed above, suggest that uniform flow conditions will only exist in the long pool if the riffle length is short enough. Once the bedform length ratio is greater than 1:7.0, the flow tends towards a non-uniform state at this constant pool length.

5.5 Comparison of Different Shear Stresses

In uniform flow, the shear stress estimated from the velocity profile and from the Reynolds stress profile should theoretically give similar values (Wilcock, 1996). Different values indicate that the stresses are out of balance. Reynolds stress is normally generated at the wall, and is related to the

gradient of velocity near the wall in a classic boundary layer (Dingman, 2009). In decelerating flow, and in the adjustment of an accelerated flow (concentrated in a high velocity core) towards uniform flow, Reynolds stress is generated elsewhere in the section due to strong velocity gradients. In this case, the Reynolds stress peak occurs above the surface of the bed (Yang and Chow, 2008). The opposite occurs in accelerating flow, and in the adjustment of a decelerated flow (fuller velocity profile, nearly constant across the cross-section) towards uniform flow. Reynolds stress in the second case stays low, even as the near-bed velocity gradient increases, indicating that stress on the bed is very high. It takes some distance before the Reynolds stress can catch up to the shear stress due to velocity, which occurs when the Reynolds stress is generated at the bed and diffuses upwards, as occurs in uniform channels.

In these experiments, the shear stress estimated from the velocity profile increases over the contraction and riffle and decreases through the expansion and pool (Figure 83a). The shear stress estimated from the Reynolds stress profile remains low over the contraction and start of the riffle, increases over the end of the riffle and expansion, and decreases in the pool. Note that the shear stress has been smoothed by a running average over the five nearest points.

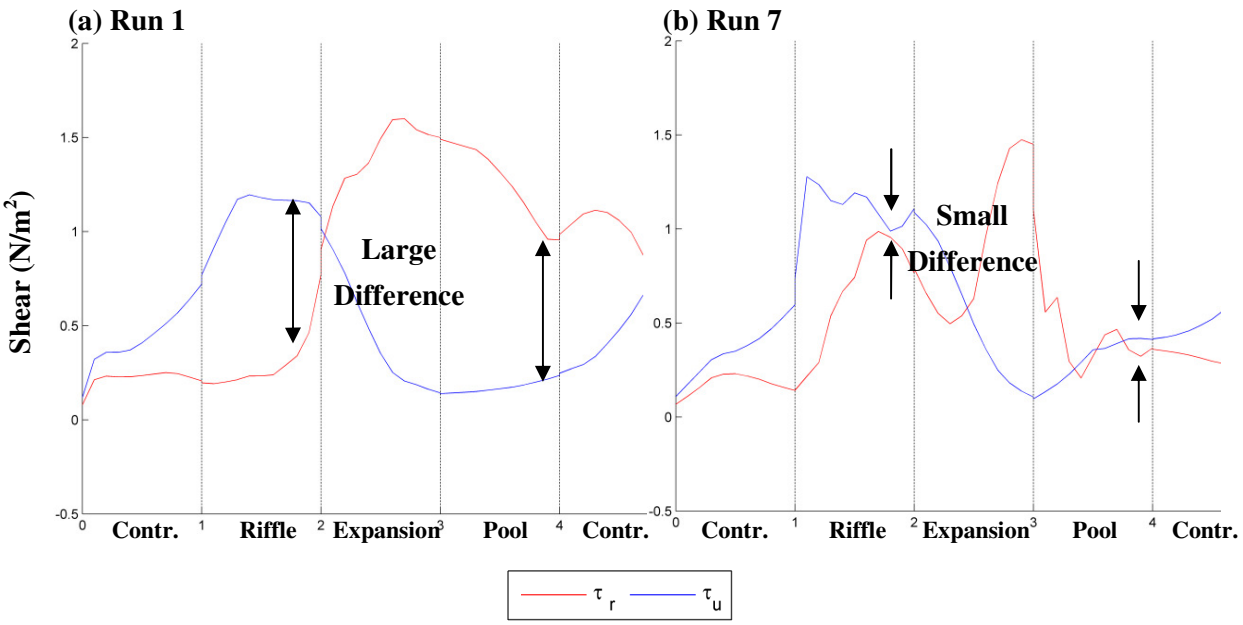

Figure 83. Comparison of τ_u and τ_r at the channel centerline (y=0.30 m) for Run 1 and Run 7.

In general, as the pool and riffle length increase, the difference in the two estimated shear stresses at the end of the riffle and pool decreases (Figure 83b). The decrease in the shear stress difference shows that the two shear stresses are converging to a common value, indicating that a new balance between the forces acting on the velocity and turbulence has been reached. In Runs 6 and 7, the riffle length was

long enough for a more uniform flow to develop, and a new balance between the two stresses developed leading to similar values in τ_r and τ_u. This same balance between the stresses occurs in the pool for all runs other than Run 1. As the pool length increases, a new balance of the shear stresses occurs, indicating that the flow is moving towards uniformity.

When comparing the total summation of τ_u and τ_r, the stress increases over the riffle and decreases over the pool, with the peak located in the expansion (Figure 84). This indicates that riffles can 'end' when a threshold is exceeded on the way up and scour occurs in the expansion. Pools will 'end' when a threshold is exceeded on the way down and sediment will deposit, forming the exit slope from the pool to the next riffle.

Overall, the level of total shear stress in Run 1 remains high throughout the entire pool length, indicating that erosion will be dominant in this configuration. All other runs show smaller total shear stress levels at the end of the pool, indicating that sediment may deposit in the end of these relatively stable areas. The difference between the incoming shear stress observed in zone I and the exiting shear stress observed in zone V, is due to the fact that the approach section consisted of a flat bed with no bedforms, and therefore, had very little shear stress associated to it.

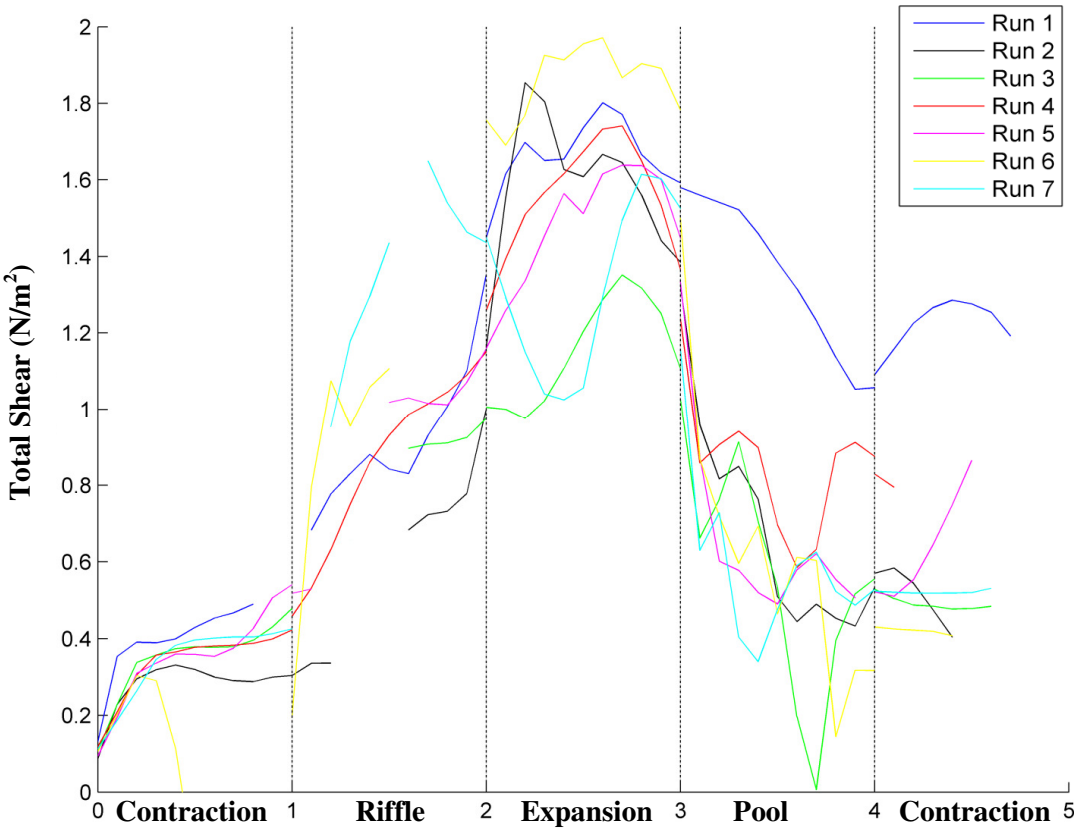

Figure 84. Summation of τ_u and τ_r at the channel centerline (y=0.30 m) for Runs 1 through 7.

5.6 Fundamental Control on Hydrodynamics

Overall, the length of riffles and pools exert a fundamental control on the distribution of flow and turbulence within a channel. In the pool, energy is dissipated both through turbulence and as the flow is redistributed to match uniform flow. In the riffle, kinetic energy is generated as the flow velocity increases, which redistributes the flow towards its own unique uniform conditions.

In general, as the pool length increases, the flow in the pool-riffle unit becomes more uniform. This is confirmed as the flow returns to a more uniform state by the end of the pool in the longer pools, as observed with the streamwise velocity, vertical velocity, and Π parameter. The Reynolds stress also decreases as the pool length increases, causing an increase in turbulent coherence downstream of the high Reynolds stress. At the downstream end of the pool, both shear stresses estimated from the velocity profile and Reynolds stress profile decrease to their lowest values. From these results, it can be concluded that uniform flow conditions exist at the end of the pool when the bedform length ratio is greater than approximately 1:5.0 when the riffle length was held constant.

In general, as the riffle length increases, the flow in the pool became more non-uniform. This is evident from the increasing lateral gradients in streamwise velocity, Π, and Reynolds stress. As the riffle length increases, a faster and more turbulent core is generated at the channel centerline, leading to less uniform flow throughout the entire pool length. As the riffle length increases, the generated turbulence increases, leading to non-uniform flow cross-section at the end of the pool. From these results, it can be concluded that uniform flow conditions are no longer observed at the end of the pool when the bedform length ratio exceeds 1:7.0 when the pool length was held constant.

Due to the fact that the bedforms were not deformable and therefore do not fully represent natural bedforms, the use of these results in pool-riffle design is highly speculative and more research must be completed. However, comparing the results found in this thesis to the summarized hypotheses in Section 2.6, multiple mechanisms are observed that could influence pool-riffle maintenance. For instance, increased turbulence at the pool head supports the idea that it may be important for pool scour, and the results support previous observations of flow convergence in pools. Using the suggested bedform scaling range for design is speculative as well, but turbulence eventually decreases in the pool, which suggests that it may limit the length of the pool, as the material would eventually start to deposit and a riffle would form. Along with the pool-riffle scales considered in this thesis, more research must be conducted at the internal scaling parameters, i.e. the relative length of the pool and riffle within one bedform length, as these scaling relations will also impact the hydrodynamics within a pool-riffle unit, and will change the results found in this thesis.

5.7 Recommendations for Future Research

The results show the hydrodynamic effects of convective acceleration and deceleration over different bedform lengths of a smooth, low-slope bedform in a wall-bounded open channel. The main limitation of this study is that it was conducted over simplified bedforms that lacked sediment transport, realistic three-dimensional topography (sinuosity), and repeating bedforms. Although these parameters were removed in order to reduce the complexity of the experiment and results, these factors must be considered to determine the role they play in the process of pool formation and maintenance in natural and restored channels.

Another limitation of this study is the complexity of pool-riffle scaling. Pool-riffle sequences are known to scale at a width to total bedform length of 1:5-7. It was this definition of bedform scaling that these experiments were based upon. However, the scale between the length of the pool and the length of the riffle is not explicitly stated in this definition. The literature states that the ratio of pool to riffle length is generally around 1:0.9-1.9 in channels with less than 2% slope (Carling and Orr, 2000; Wohl et al., 1993). In these experiments, the pool to riffle ratio varied between each test, with a 1:1 ratio in Runs 1 and 7, to a maximum ratio of 1:6 in Run 4. This scaling parameter may play a vital role in pool-riffle maintenance, and should be considered in future research.

The turbulent structures were measured in this research, with some coherence observed in the integral time scale and the integral length scale. The data showed interesting results, however, the overall trend in the data was not clear through these findings. Turbulent structures may reveal important trends in coherence in flow over bedforms and should be pursued in future research.

The results found in this thesis should be compared to future pool-riffle studies to determine if these findings on the flow hydrodynamics are applicable over a wide range of field sites. All future experiments should measure velocity in high spatial distributions to observe the three-dimensional effects that occur throughout the convective acceleration and deceleration processes. The experiments should also categorize the results based upon the different bed slopes so that the flow in different zones can be easily compared.

Chapter 6

CONCLUSIONS

Pool-riffle sequences are used in current river restoration practices but their hydrodynamics are still not fully understood, which can lead to unstable restoration designs. Using Ultrasonic Velocity Profilers over movable, simplified bedforms, the effects of flow and turbulence were measured over seven different pool-riffle bedform lengths. The described experiments demonstrate that the length of the pool and riffle exert a fundamental control on the distribution of the flow and turbulence in a channel. These experiments are unique in the literature and indicate that simplified experiments can be used to understand the hydrodynamics of convective acceleration and deceleration found in natural pool-riffle bedforms. Other parameters tested show the complexity of the hydrodynamics and confirm the need for isolating the key parameters, as was completed in this thesis, as a means to unlocking the reasons behind persistent scaling relation between width and bedform length.

Overall, the length of riffles and pools exert a fundamental control on the distribution of flow and turbulence within a channel. In the pool, energy is dissipated both through turbulence and as the flow is redistributed to uniform flow conditions. In the riffle, kinetic energy increases as the flow velocity increases, and as the length increases, the flow moves towards a new uniform flow condition. Therefore, when the flow reaches the pool, the distribution of flow is farther from the uniform flow conditions in the pool. This means that longer distances are required to redistribute the flow in the pool to uniform conditions when the riffle length is long. It can be concluded from these results that uniform flow conditions exist at the end of the pool when the bedform length ratio is greater than approximately 1:5.0 when the riffle length is held constant, and that uniform flow conditions are no longer observed at the end of the pool when the bedform length ratio exceeds 1:7.0 when the pool length is held constant.

These results should be used only as a preliminary understanding in restoration design. Multiple controls are responsible for stable pool-riffle sequences, and more information is needed to fully understand pool-riffle hydrodynamics. Future research should concentrate on extending the results to include three-dimensional pool-riffle configurations, repeating bedform configurations, internal scaling parameters, and sediment transport. Ultimately, as the hydrodynamics of pool-riffle sequences are better understood, better bedform designs can be implemented in restoration projects.

REFERENCES

Afzalimehr, H. and C. D. Rennie, 2009. "Determination of bed shear stress in gravel-bed rivers using boundary-layer parameters." *Hydrological Sciences Journal-Journal Des Sciences Hydrologiques* **54**(1): 147-159.

Alfrink, B. J. and L. C. Van Rijn, 1983. "Two-equation turbulence model for flow in trenches." *Journal of Hydraulic Engineering – ASCE* **109**(7): 941-958.

Barrie, R., 2009. Personal communication, Customer Support Technologist Specialist, EMS-CHEMIE, Sumter, SC, USA.

Best, J. and R. A. Kostachuck, 2002. "An experimental study of turbulent flow over a low-angle dune." *Journal of Geophysical Research* **107**(C9): 3135.

Bhowmik, N. G. and M. Demissie, 1982. "Bed material sorting in pools and riffles." *Journal of the Hydraulic Division* **108**: 1227-1231.

Blanckaert, K., 2009. "Saturation of curvature-induced secondary flow, energy losses, and turbulence in sharp open-channel bends: laboratory experiments, analysis, and modeling." *Journal of Geophysical Research* **114**: F03015.

Booker, D. J., D. A. Sear, and A. J. Payne, 2001. "Modelling three-dimensional flow structures and patterns of boundary shear stress in a natural pool-riffle sequence." *Earth Surface Processes and Landforms* **26**(5): 553-576.

Boulton, A. J., and P.S. Lake, 1992. "The ecology of two intermittent streams in Victoria, Australia. II. Comparisons of faunal composition between habitats, rivers and years." *Freshwater Biology* **27**: 99-121.

Brown, A. V, and K. B. Brown, 1984. "Distribution of insects within riffles of streams." *Freshwater Invertebrate Biology* **3**(1): 2-11.

Buffin-Bélanger, T., A. G. Roy, and A. D. Kirkbride, 2000. "On large-scale flow structures in a gravel-bed river." *Geomorphology* **32**(3-4): 417-435.

Butman, C., and R. Chapman, 1989. The 17-Meter Flume at the Coastal Research Laboratory. Part I: Description and User's Manual. Woods Hole Oceanographic Institution. Woods Hole, MA, USA.

Caamaño, D., P. Goodwin, P.E. M.ASCE, J. C. P. Liou, and S. Daley-Laursen, 2009. "Unifying Criterion for the Velocity Reversal Hypothesis in Gravel-Bed Rivers." *Journal of Hydraulic Engineering* **135**(1): 66-70.

Carling, P., 1991. "An appraisal of the velocity-reversal hypothesis for stable pool-riffle sequences in the River Severn, England." *Earth Surface Processes and Landforms* **16**: 19-31.

Carling, P. A. and H. G. Orr, 2000. "Morphology of riffle-pool sequences in the River Severn, England." Earth *Surface Processes and Landforms* **25**: 369-384.

Carling, P. A., J. J. Williams, E. Gölz, and A.D. Kelsey, 2000. "The morphodynamics of fluvial sand dunes in the River Rhine, near Mainz, Germany. II. Hydrodynamics and sediment transport." *Sedimentology* **47**(1): 253-278.

Christian, C. D. and P. A. Corney, 2004. "Three dimensional model of flow over a shallow trench." Modèle tridimensionnel de l'écoulement au-dessus d'un fossé peu profound. *Journal of Hydraulic Research* **42**(1): 71-80.

Church, M. and D. Jones, 1982. Channel bars in gravel-bed rivers. Gravel-bed Rivers. R. D. Hey, J. C. Bathurst and C. R. Thorne. Chicester, UK, Wiley**:** 291-338.

Clarke, S. J., L. Bruce-Burgess, and G. Wharton, 2003. "Linking form and function: towards an eco-hydromorphic approach to sustainable river restoration." *Aquatic Conservation-Marine and Freshwater Ecosystems* **13**(5): 439-450.

Clifford, N. J., 1993a. "Differential bed sedimentology and the maintenance of riffle-pool sequences." *Catena* **20**: 447-468.

Clifford, N. J., 1993b. "Formation of riffle-pool sequences: field evidence for an autogenetic process." *Sedimentary Geology* **85**: 39-51.

Clifford, N. J., 1996. Morphology and stage-dependent flow structure in a gravel-bed river. Coherent Flow Structures in Open Channels. P. J. Ashworth, S. J. Bennett, J. L. Best and S. J. McLelland. Wallingford, U.K., Wiley**:** 545-566.

Clifford, N. J., O. P. Harmar, G. Harvey, and G. E. Petts, 2006. "Physical habitat, eco-hydraulics and river design: a review and re-evaluation of some popular concepts and methods." *Aquatic Conservation-Marine and Freshwater Ecosystems* **16**(4): 389-408.

Clifford, N. J. and K. S. Richards, 1992. The reversal hypothesis and the maintenance of riffle-pool sequences: a review and field appraisal. Lowland Floodplain Rivers: Geomorphological Perspectives. P. Carling and G. E. Petts. Chichester, UK, Wiley**:** 43-70.

Coles, D., 1956. "The law of the wake in the turbulent boundary layer." *Journal of Fluid Mechanics* **1**: 191-226.

Dingman, S. L., 2009. Fluvial Hydraulics. Oxford University Press, New York, NY, USA.

Emery, J. C., A. M. Gurnell, N. J. Clifford, G. E. Petts, I. P. Morrissey, and P.J. Soar, 2003. "Classifying the hydraulic performance of riffle-pool bedforms for habitat assessment and river rehabilitation design." *River Research and Applications* **19**(5-6): 533-549.

Figliola, R.S. and D.E. Beasley, 2006. Theory and Design for Mechanical Measurements, Fourth Edition. John Wiley & Sons, Inc. Hoboken, NJ, USA.

Goring, D. G. and V. I. Nikora, 2002. "Despiking acoustic Doppler velocimeter data." *Journal of Hydraulic Engineering* **128**(1): 117-126.

Gorman, O. T., and J.R. Karr, 1978. "Habitat structure and stream fish communities." *Ecology* **59**(3): 507-515.

Harper, D., M. Ebrahimnezhad, and F. C. I. Cot, 1998. "Artificial riffles in river rehabilitation: setting the goals and measuring the successes." *Aquatic Conservation-Marine and Freshwater Ecosystems* **8**(1): 5-16.

Harrison, L. R. and E. A. Keller, 2007. "Modeling forced pool–riffle hydraulics in a boulder-bed stream, southern California." *Geomorpholgy* **83**(3-4): 232-248.

Hassan, M. and R. D. Woodsmith, 2004. "Bedload transport in an obstruction-formed pool in a forest gravelbed stream." *Geomorphology* **58**: 203-221.

Heaton, M.G., J.G. Imhof, R. Grillmayer, 2002. Ontario Stream Manual Development: Ontario's Stream Rehabilitation Manual. Ontario Ministry of Natural Resources and Environment Canada's Great Lakes 2000 Cleanup Fund. Ontario Streams, Belfountain, ON, Canada.

Heggberget, T.G., T. Haukebot, and B. Veie-Rosvoll, 1986. "An aerial method of assessing spawning activity of Atlantic salmon, *Salmo salar* L., and brown trout, *Salmo trutta* L., in Norwegian streams." *Journal of Fisheries and Biology* **28**: 335-342.

Holtschlag, D.J., and Hoard, C.J., 2009. Detection of conveyance changes in St. Clair River using historical water-level and flow data with inverse one-dimensional hydrodynamic modeling. U.S. Geological Survey Scientific Investigations Report 2009–5080. U.S Geological Survey, Reston, VA, USA.

Jackson, R. G., 1976. "Sedimentological and fluid-dynamic implications of the turbulent bursting phenomenon in geophysical flows." *Journal of Fluid Mechanics* **77**: 531-560.

Julien, P.Y., 2002. River Mechanics. Cambridge University Press, Cambridge, UK.

Keller, E. A., 1971. "Areal sorting of bed material: the hypothesis of velocity reversal." *Geological Society of America Bulletin* **82**: 753-756.

Keller, E. A., 1978. "Pools, riffles, and channelization." *Environmental Geology* **2**(2): 119-127.

Keller, E. A. and W. N. Melhorn, 1978. "Rhythmic spacing and origin of pools and riffles." *Geological Society of America Bulletin* **89**: 723-730.

Kironoto, B. A. and W. H. Graf, 1995. "Turbulence characteristics in rough non-uniform open-channel flow." *Proceedings of the Institution of Civil Engineers-Water Maritime and Energy* **112**(4): 336-348.

Esterly, E., 2010. Personal communication, Operations Manager of Koffler Sales LLC, Lake Zurich, IL, USA.

Leopold, L. B. and M. G. Wolman, 1957. River channel patterns: braided, meandering, and straight. Geological Survey Professional Paper 282-B. United Sates Government Printing Office, WA, USA.

Leopold, L. B., M. G. Wolman, J. P. Miller, 1964. Fluvial Processes in Geomorphology. Dover Publications Inc., New York, NY. USA.

Lhermitte, R. and U. Lemmin, 1994. "Open-channel flow and turbulence measurement by high-resolution Doppler sonar." *Journal of Atmospheric and Oceanic Technology* **11**(5): 1295-1308.

Lhermitte, R., and R. Serafin, 1984. "Pulse-to-pulse coherent Doppler sonar signal processing techniques." *Journal of Atmospheric and Oceanic Technology* **1**(4): 293-308.

Lisle, T. E., 1982. "Effects of aggradation and degradation on riffle-pool morphology in natural gravel channels, northwestern California." *Water Resources Research* **18**: 1643-1651.

Lisle, T. E., 1986. "Stabilization of a gravel channel by large streamside obstructions and bedrock bends, Jacoby Creek, northwest California." *Geological Society of America Bulletin* **97**: 999-1011.

Lofthouse, C., and A. Robert, 2008. "Riffle-pool sequences and meander morphology." *Geomorphology* **99**: 214-223.

Logan, P. and M. P. Brooker, 1983. "The macroinvertebrate faunas of riffles and pools." *Water Research* **17**(3): 263-270.

Lubbers, J. and R. Graaff, 1998. "A simple and accurate formula for the sound velocity in water." *Ultrasound in Medicine and Biology* **24**(7): 1065-1068.

MacVicar, B. J. and C. D. Rennie, in review. "Secondary currents, shear stress and turbulence in a straight artificial pool." *Water Resources Research*.

MacVicar, B. J., C. D. Rennie, and A. G. Roy, 2010, "Discussion of 'Unifying Criterion for the Velocity Reversal Hypothesis in Gravel-Bed Rivers' by D. Caamano, P. Goodwin, J. M. Buffington, J. C. P. Liou, and S. Daley-Laursen." *Journal of Hydraulic Engineering-ASCE*, **136**: 550-552.

MacVicar, B. J. and A. G. Roy, 2007a. "Hydrodynamics of a forced riffle pool in a gravel bed river: 1. Mean velocity and turbulence intensity." *Water Resources Research* **43**(12): W12401.

MacVicar, B. J. and A. G. Roy, 2007b. "Hydrodynamics of a forced riffle pool in a gravel bed river: 2. Scale and structure of coherent turbulent events." *Water Resources Research* **43**(12): W12402.

MacWilliams, M. L. J., J. M. Wheaton, G. B. Pasternack, R. L. Street, and P. K. Kitanidis, 2006. "Flow convergence routing hypothesis for pool-riffle maintenance in alluvial rivers." *Water Resources Research* **42**: W10427.

Madej, M. A., 1999. "Temporal and spatial variability in thalweg profiles of a gravel-bed river." *Earth Surface Processes and Landforms* **24**(12): 1153-1169.

McCrometer Inc., 2011. Specification and Design Features of the Ultra Mag. McCrometer Inc., Hemet, CA, USA. http://www.mccrometer.com/products/product_ultramag.asp#. May, 2011.

Met-Flow, 2002. UVP Monitor Model UVP-DUO with Sofware Version 3.0, User's Guide. Lausanne Switzerland. http://www.met-flow.com. May, 2011

Moir, H. J., C. N. Gibbins, C.Soulsby, and J. Webb, 2004. "Linking channel geomorphic characteristics to spatial patterns of spawning activity and discharge use by Atlantic salmon (*Salmo salar* L.)." *Geomorphology* **60**(1-2): 21-35.

Montgomery, D. R. and J. M. Buffington, 1997. "Channel reach morphology in mountain drainage basins." *Geological Society of America Bulletin* **109**(5): 596-611.

Montgomery, D. R., J. M. Buffington, R. D. Smith, K. M. Schmidt, and G. Pess, 1995. "Pool spacing in forest channels." *Water Resources Research* **31**(4): 1097-1105.

Nelson, J. M., R. L. Shreve, S. R. McLean, and T. G. Drake, 1995. "Role of near-bed turbulence structure in bed load transport and bed form mechanics." *Water Resources Research* **31**: 2071-2086.

Newbury, R. and M. Gaboury, 1993. "Exploration and rehabilitation of hydraulic habitats in streams using principles of fluvial behaviour." *Freshwater Biology* **29**: 195-210.

Nezu, I. and H. Nakagawa, 1993. Turbulence in Open-channel Flows. A.A. Balkema, Rotterdam, Netherlands.

National River Restoration Science Synthesis (NRRSS), 2006. National River Restoration Science Synthesis Statistics Page for All Node Areas. Center for Biological Informatics of the U.S. Geological Survey. http://nrrss.nbii.gov/info/statistics.html. Accessed on May, 2011.

O'Neill, P.L., D. Nicolaides, D. Honnery, and J. Soria, 2004. "Autocorrelation functions and the determination of integral length with reference to experimental and numerical data." *15th Australasian Fluid Mechanics Conference*. The University of Sydney, Sydney Australia, 13-17 December 2004.

Onitsuka, K., J. Akiyama, and S. Matsuoka, 2009. "Prediction of velocity profiles and Reynolds stress distributions in turbulent open-channel flows with adverse pressure gradient." *Journal of Hydraulic Research* **47**(1): 58-65.

Pasternack, G. B., M. K. Bounrisavong, and K. K. Parikh, 2008. "Backwater control on riffle-pool hydraulics, fish habitat quality, and sediment transport regime in gravel-bed rivers." *Journal of Hydrology* **357**(1-2): 125-139.

Pedocchi, F., and M. H. Garcia, 2009. Application of an ultrasonic velocity profiler for velocity and suspended sediment measurements in an oscillatory boundary layer. Civil Engineering Studies, Hydraulic Series No. 83. Coastal Geosciences Program U.S. Office of Naval Research; Ven Te Chow Hydrosystems Laboratory, Department of Civil and Environmental Engineering, University of Illinois at Urbana-Champaign, Urbana, IL, USA.

Pyrce, R. S. and P. E. Ashmore, 2005. "Bedload path length and point bar development in gravel-bed river models." *Sedimentology* **52**(4): 839-857.

Richards, K. S., 1976. "Channel width and the riffle-pool sequence." *Geological Society of America Bulletin* **87**: 883-890.

Richards, K. S., 1978. "Simulation of flow geometry in a riffle-pool stream." *Earth Surface Processes and Landforms* **3**: 345-354.

Ross, R. M., T. W. H. Backman, and R. M. Bennett, 1993. Evaluation of habitat suitability index models for riverine life stages of American Shad, with proposed models for premigratory juveniles. Biological Report 14. Fish and Wildlife Service, U.S. Department of the Interior, WA, D.C., USA.

Roy, A. G., P. M. Biron, and M. F. Lapointe, 1997. "Implications of low-pass filtering on power spectra and autocorrelation functions of turbulent velocity signals." *Mathematical Geology* **29**(5): 653-668.

Roy, A. G., T. Buffin-Bélanger, H. Lamarre, and A. D. Kirkbride, 2004. "Size, shape and dynamics of large-scale turbulent flow structures in a gravel-bed river." *Journal of Fluid Mechanics* **500**: 1-27.

Sear, D. A., 1996. "Sediment transport processes in pool-riffle sequences." *Earth Surface Processes and Landforms* **21**: 241-262.

Simpson, R. L., 1989. "Turbulent boundary-layer separation." *Annual Review of Fluid Mechanics* **21**: 205-234.

Song, T. and Y. M. Chiew, 2001. "Turbulence measurement in nonuniform open-channel flow using acoustic Doppler velocimeter (ADV)." *Journal of Engineering Mechanics* **127**(3): 219-231.

Stansby, P. K. and J. G. Zhou, 1998. "Shallow-water flow solver with non-hydrostatic pressure: 2D vertical plane problems." *International Journal for Numerical Methods in Fluids* **28**(3): 541-563.

Stuart, T. A., 1953. "Spawning migration, reproduction and young stages of loch trout." *Freshwater Salmon Fisheries Restoration* **5**: 1-39.

Sumer, B. M., L. H. C. Chua, N. S. Cheng, and J. Fredsoe, 2003. "Influence of turbulence on bed load sediment transport." *Journal of Hydraulic Engineering* **129**(8): 585-596.

Teleki, P. G., 1972. "Areal sorting of bedload material: the hypothesis of velocity reversal, discussion." *Geologic Society of America Bulletin* **83**: 911-914.

Thompson, D. M., 2002. "Geometric adjustment of pools to changes in slope and discharge: a flume experiment." *Geomorphology* **46**: 257-265.

Thompson, D. M., 2004. "The influence of pool length on local turbulence production and energy slope: a flume experiment." *Earth Surface Processes and Landforms* **29**: 1341-1358.

Thompson, D. M., 2006. "The role of vortex shedding in the scour of pools." *Advances in Water Resources* **29**(2): 121-129.

Thompson, D. M., 2007. "The characteristics of turbulence in a shear zone downstream of a channel constriction in a coarse-grained forced pool." *Geomorphology* **83**(3-4): 199-214.

Thompson, D. M., J. M. Nelson, and E. E. Wohl, 1998. "Interactions between pool geometry and hydraulics." *Water Resources Research* **34**(12): 3763-3681.

Thompson, D. M. and E. E. Wohl, 2009. "The linkage between velocity patterns and sediment entrainment in a forced-pool and riffle unit." *Earth Surface Processes and Landforms* **34**: 177-192.

Thompson, D. M., E. E. Wohl, and R. D. Jarrett, 1996. "A revised velocity-reversal and sediment-sorting model for a high-gradient, pool-riffle stream." *Physical Geography* **17**: 142-156.

Thompson, D. M., E. E. Wohl, and R. D. Jarrett, 1999. "Velocity reversals and sediment sorting in pools and riffles controlled by channel constrictions." *Geomorphology* **27**: 229-241.

Uijttewaal, W.S.J., and J. Tukker, 1998. "Development of quasi two-dimensional structures in a shallow free-surface mixing layer." *Experiments in Fluids* **24**: 192-200.

Van Balen, W., W. S. J. Uijttewaal, and K. Blanckaert, 2009. "Large-eddy simulation of a mildly curved open-channel flow." *Journal of Fluid Mechanics* **630**: 413-442.

Walker, D. R., R. G. Millar, and R. W. Newbury, 2004. "Energy profiles across constructed riffles." *Journal of Hydraulic Engineering* **130**(3): 199-207.

Wei, T., R. Schmidt, and P. McMurtry, 2005. "Comment on the Clauser chart method for determining the friction velocity." *Experiments in Fluids* **38**: 695-699.

Wilcock, P. R., 1996. "Estimating local bed shear stress from velocity observations." *Water Resources Research* **32**(11): 3361-3366.

Wilkinson, S. N., R. J. Keller, and I. D. Rutherfurd, 2004. "Phase-shifts in shear stress as an explanation for the maintenance of pool-riffle sequences." *Earth Surface Processes and Landforms* **29**(6): 737-753.

Wohl, E. E., J. R. Vincent, and D. J. Merritts, 1993. "Pool and riffle characteristics in relation to channel gradient." *Geomorphology* **16**: 99-110.

Yalin, M. S., 1971. "On the formation of dunes and meanders." *Proceedings of the 14th International Conference of the Hydraulic Research Association* **C13**: 1-8.

Yang, C. T., 1971. "Formation of riffles and pools." *Water Resources Research* **7**: 1567-1574.

Yang, S. Q. and A. T. Chow, 2008. "Turbulence structures in non-uniform flows." *Advances in Water Resources* **31**(10): 1344-1351.

Appendix A – Froude Number

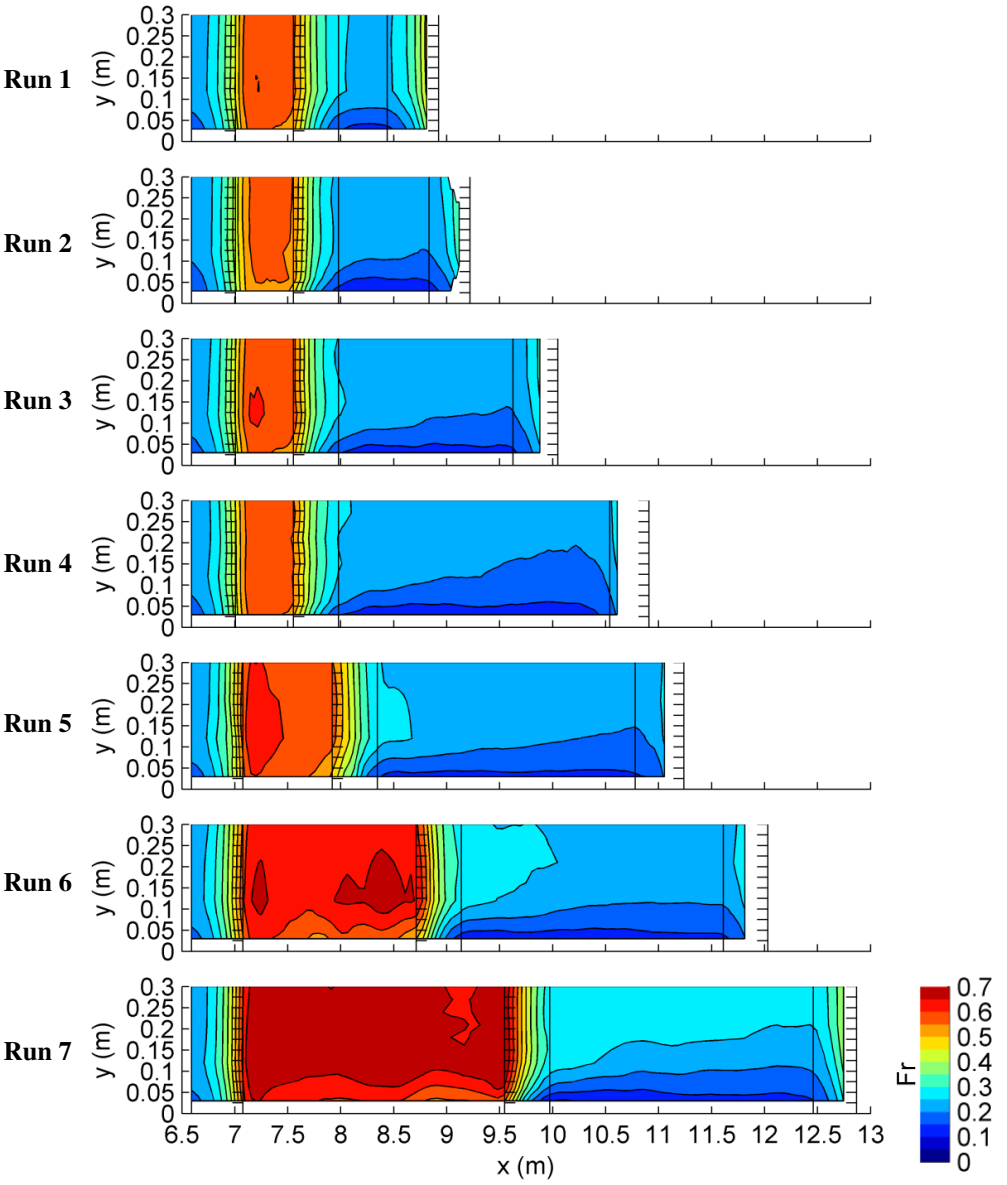

Figure 85. Froude number (Fr) in the XY plane for all runs.

Appendix B – Reynolds Number

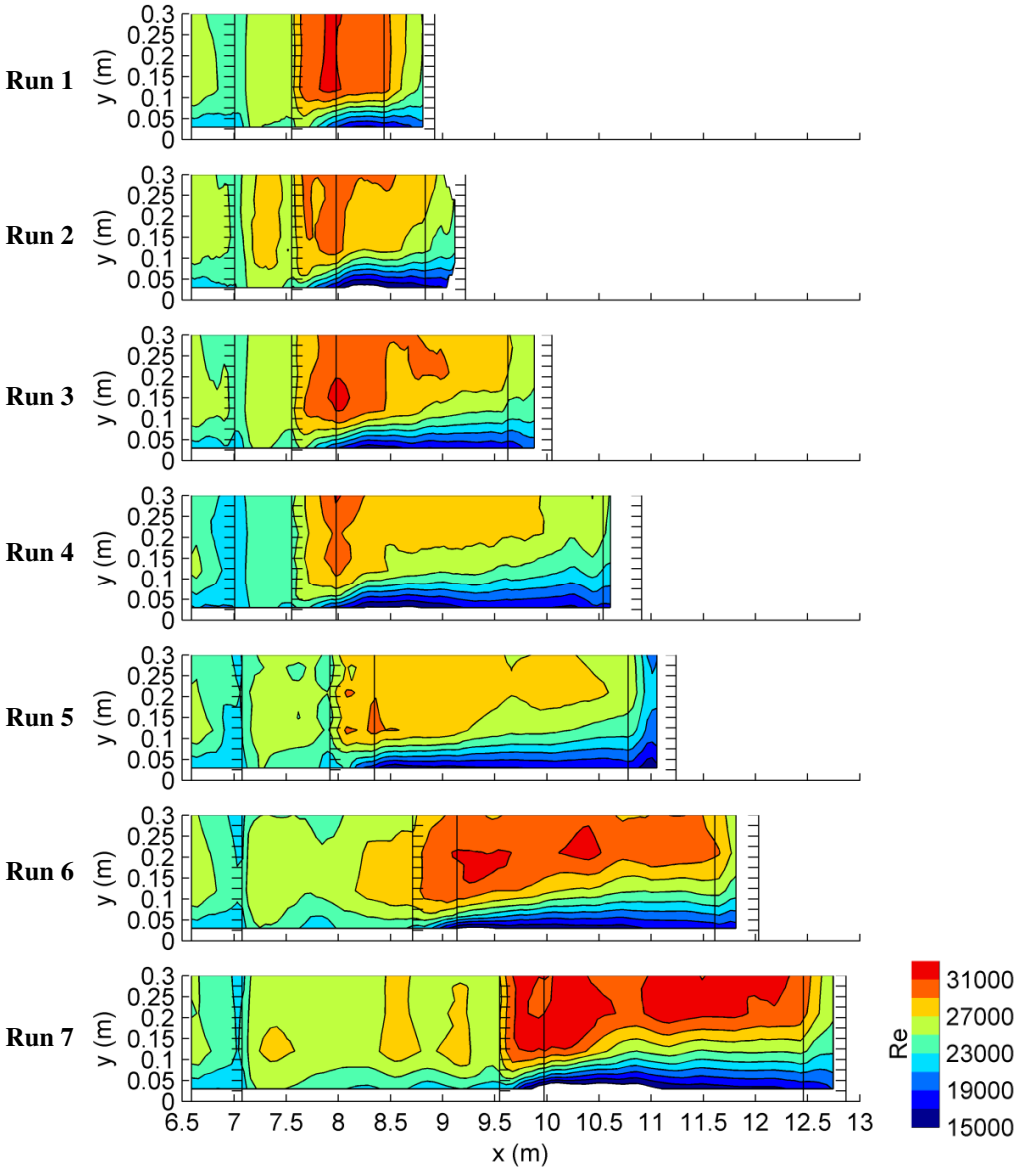

Figure 86. Reynolds number (Re) in the XY plane for the different runs.

Appendix C – Extra Riffle Length Results

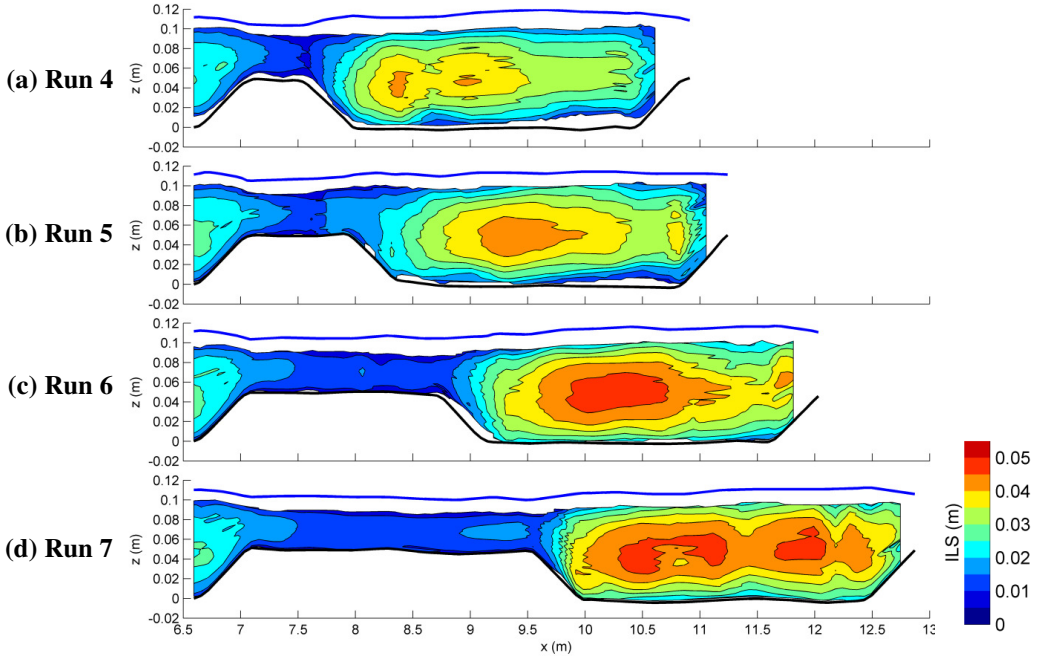

Figure 87. Integral length scale (ILS) in the XZ plane near the channel wall (y=0.03 m) for Runs 4 through 7 using the US probe.

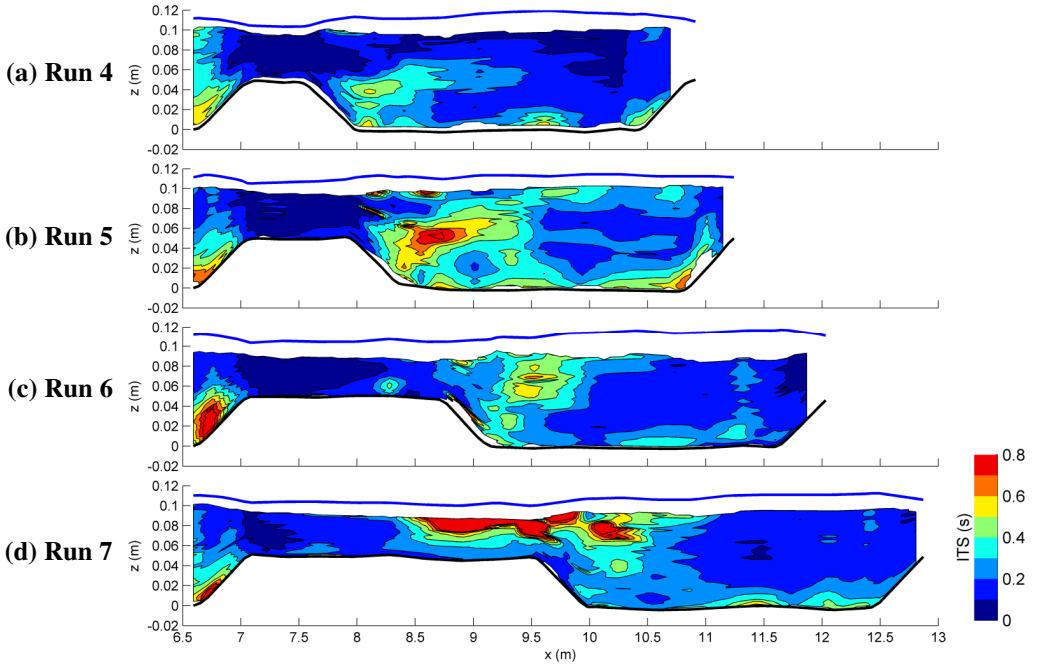

Figure 88. Integral time scale (ITS) in the XZ plane at the channel centerline (y=0.30 m) for Runs 4 through 7 using the US probe.

Appendix D –Experimental Results for Different Depths

As a part of the experimental phase of this thesis, different water depths were tested to determine the effect the water depth had on the hydrodynamics through the pool-riffle sequence. The depths that were tested were 0.05, 0.06, 0.08, and 0.10 m over zone II (original depth tested was 0.06 m). The bedform configuration used was the same as Run 7 (Table 2). In order to keep the bulk velocity upstream of the bedforms at a constant 0.21 m/s, the flow rate was changed in each test at different depths (Table 6). The bulk velocity over the riffle was different each run, however. The change in flow rate did affect the Fr and Re numbers slightly, however, they remained in an acceptable range for the flow to be considered in the same regime.

Table 6. Different flow rates, Froude and Reynolds numbers for the different depths tested.

Depth of Riffle (m)	Flow Rate (L/s)	Max Fr	Max Re ($x10^4$)
0.05	14.9	0.84	3.5
0.06	15.4	0.72	3.3
0.08	18.0	0.44	3.5
0.10	20.6	0.35	3.8

The following figures show the results collected from the different water depths. The results follow the same format as those in the body of the thesis, and include streamwise velocity, Π, τ_u, vertical velocity, $\tau_{Re,}$ τ_r, ILS, and ITS. These results are not explained in detail and are simply here for the viewing interest of the reader. No conclusions were made based on these results in the body of the thesis. It should be noted that testing was difficult at the 0.05 m depth as the velocities were very high, waves were starting to form in zone IV (Figure 89), and multiple air bubbles were formed on the UVP probe, especially in zone III. It is for these reasons that the results from this depth has many errors associated with it.

(a)  **(b)** 

Figure 89. (a)Top view and (b) side view of the wave formation in zone IV during 0.05 m testing.

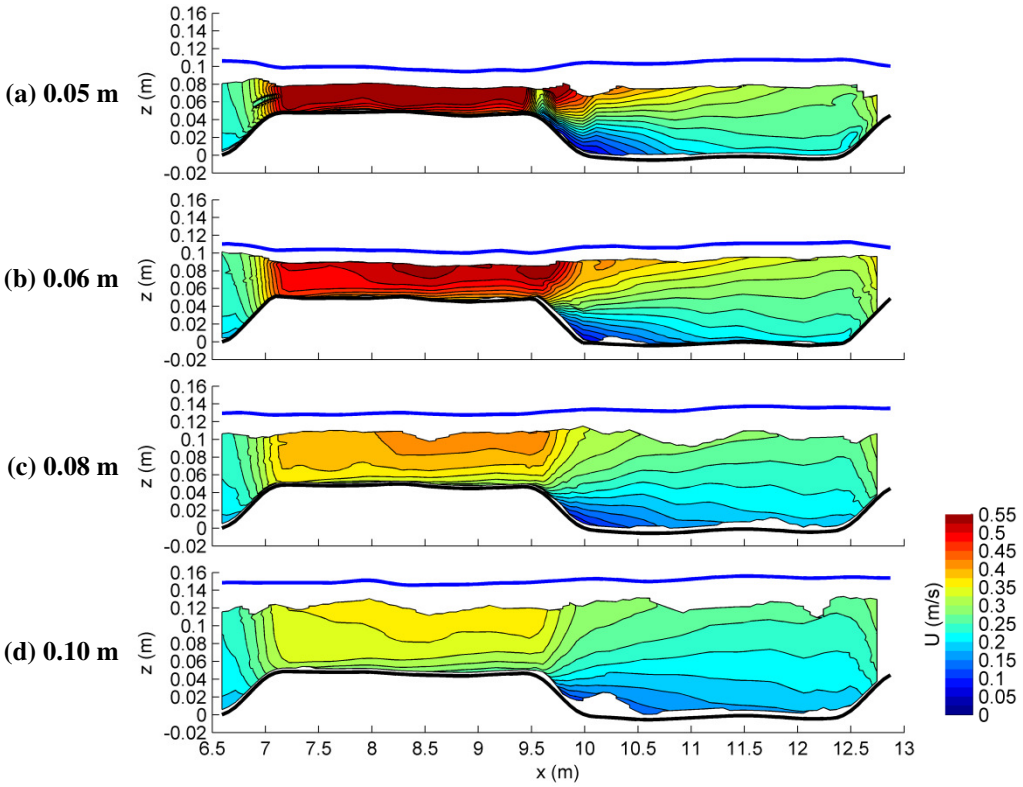

Figure 90. Mean streamwise velocity (U) in the XZ plane at the channel centerline (y=0.30 m) for four different depths.

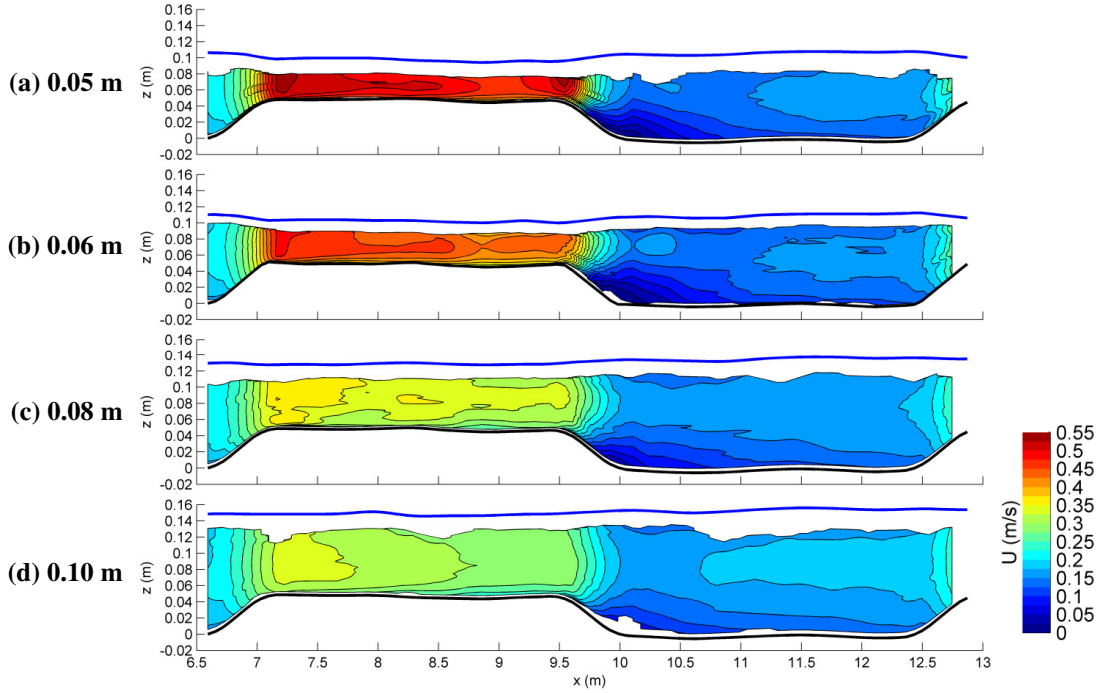

Figure 91. Mean streamwise velocity (U) in the XZ plane near the channel wall (y=0.03 m) for four different depths.

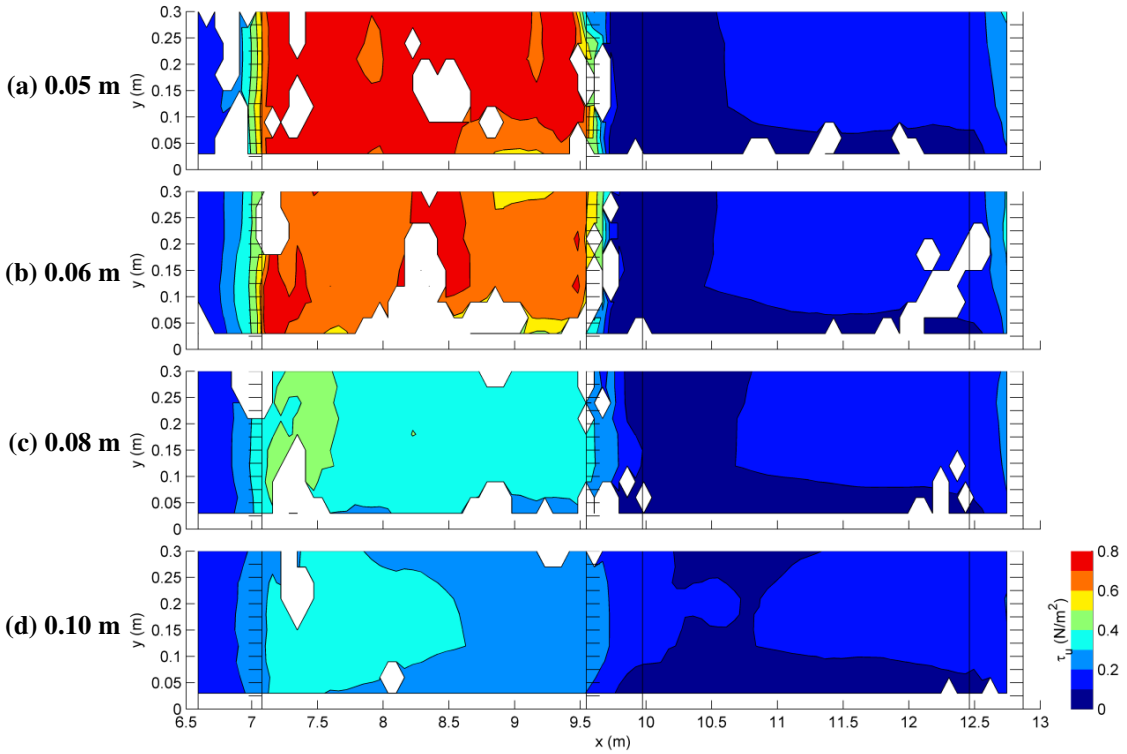

Figure 92. Shear stress estimated from the velocity profile (τ_u) in the XY plane for four different depths.

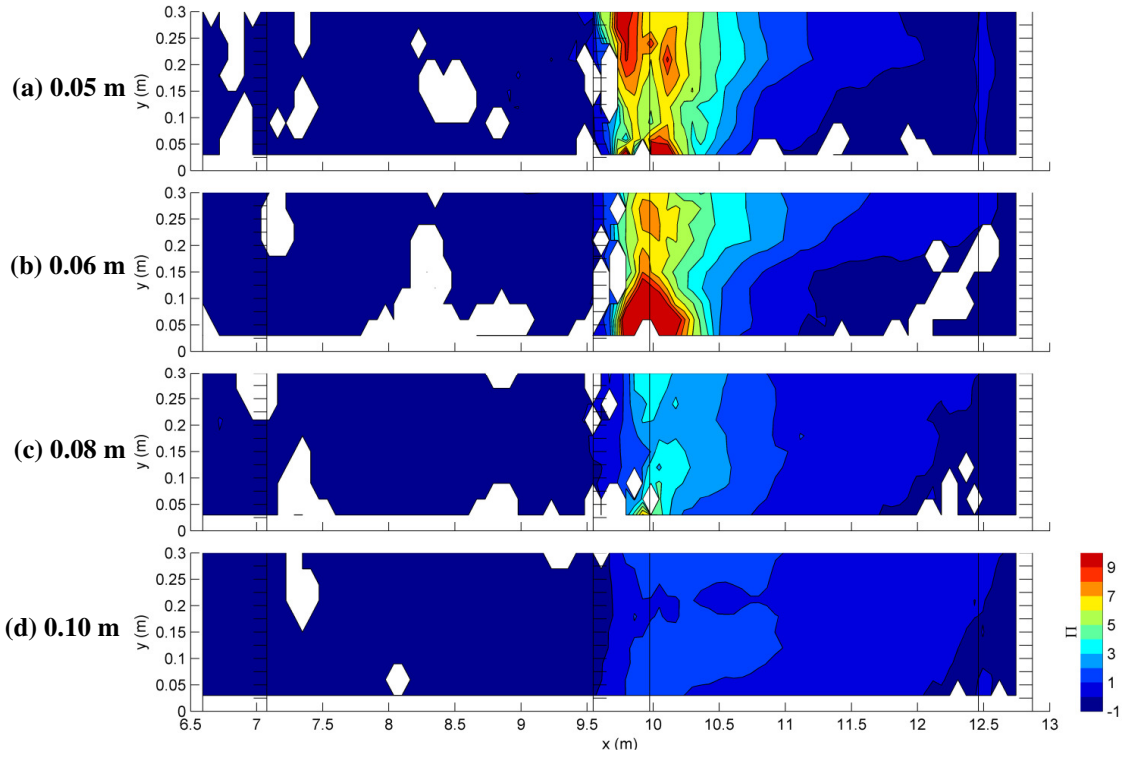

Figure 93. Coles' wake parameter (Π) in the XY plane for four different depths.

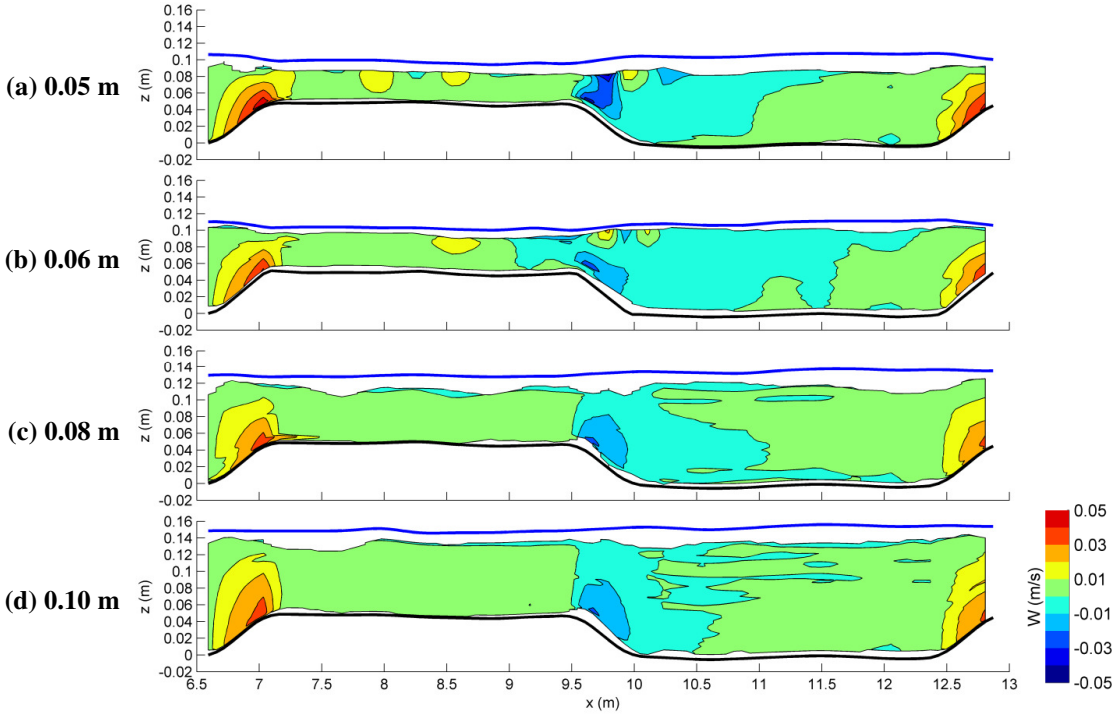

Figure 94. Mean vertical velocity (W) in the XZ plane at the channel centerline (y=0.30 m) for four different depths.

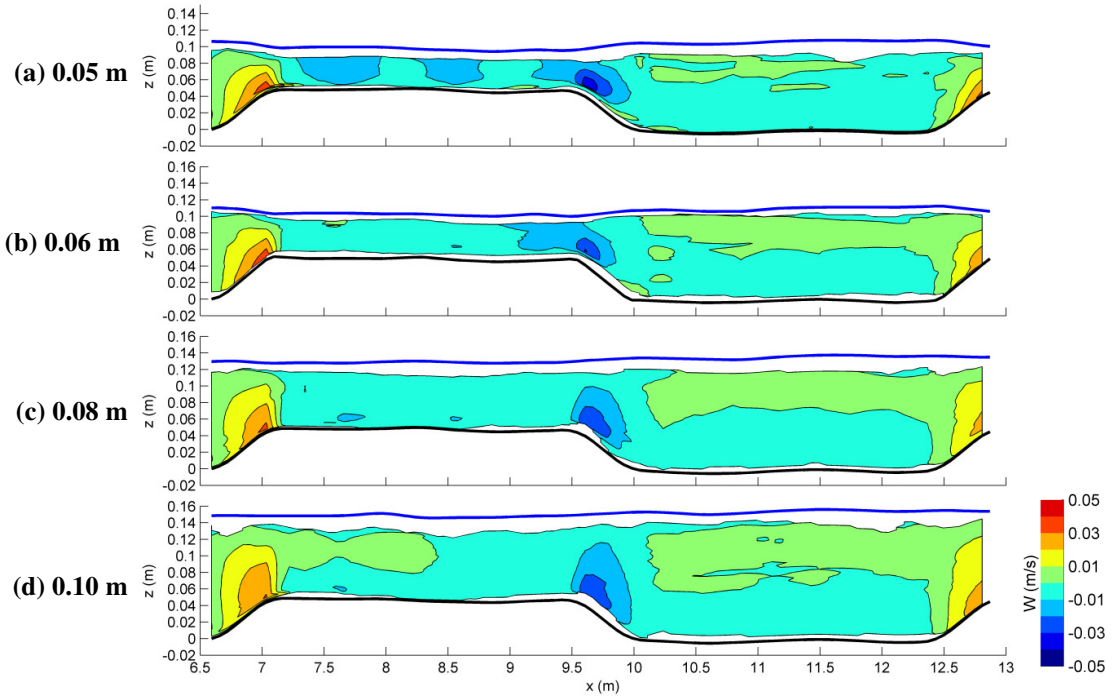

Figure 95. Mean vertical velocity (W) in the XZ plane near the channel wall (y=0.03 m) for four different depths.

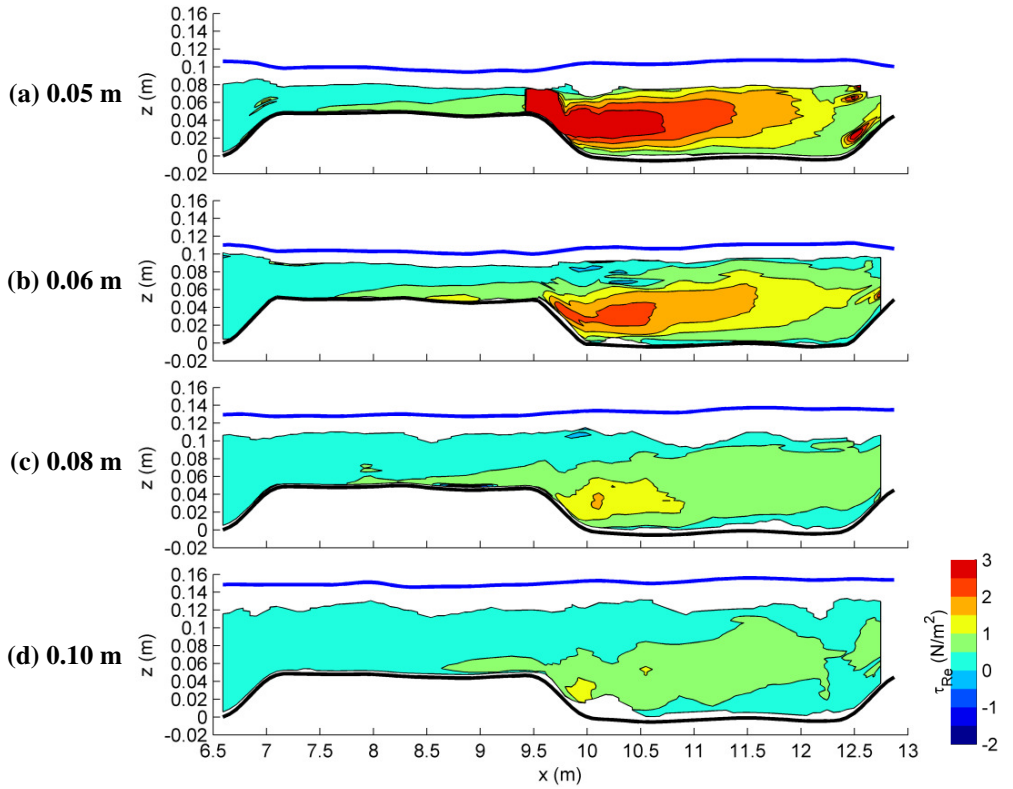

Figure 96. Reynolds stress (τ_{Re}) in the XZ plane at the channel centerline (y=0.30 m) for four different depths.

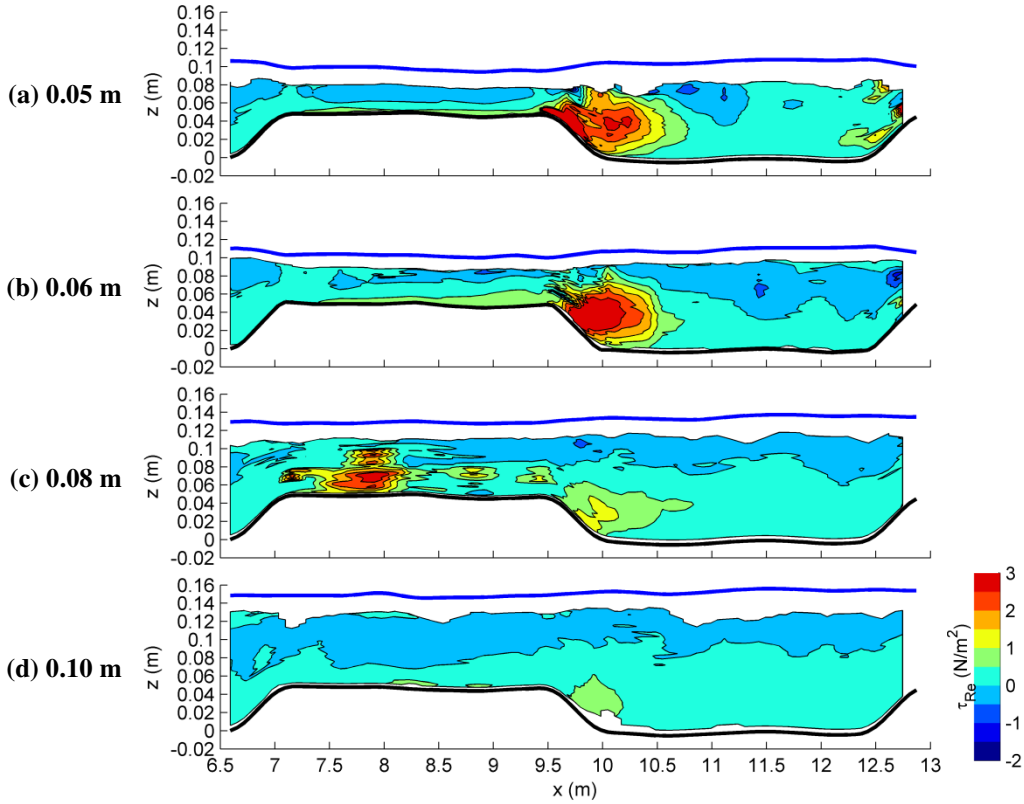

Figure 97. Reynolds stress (τ_{Re}) in the XZ plane near the channel wall (y=0.60 m) for four different depths.

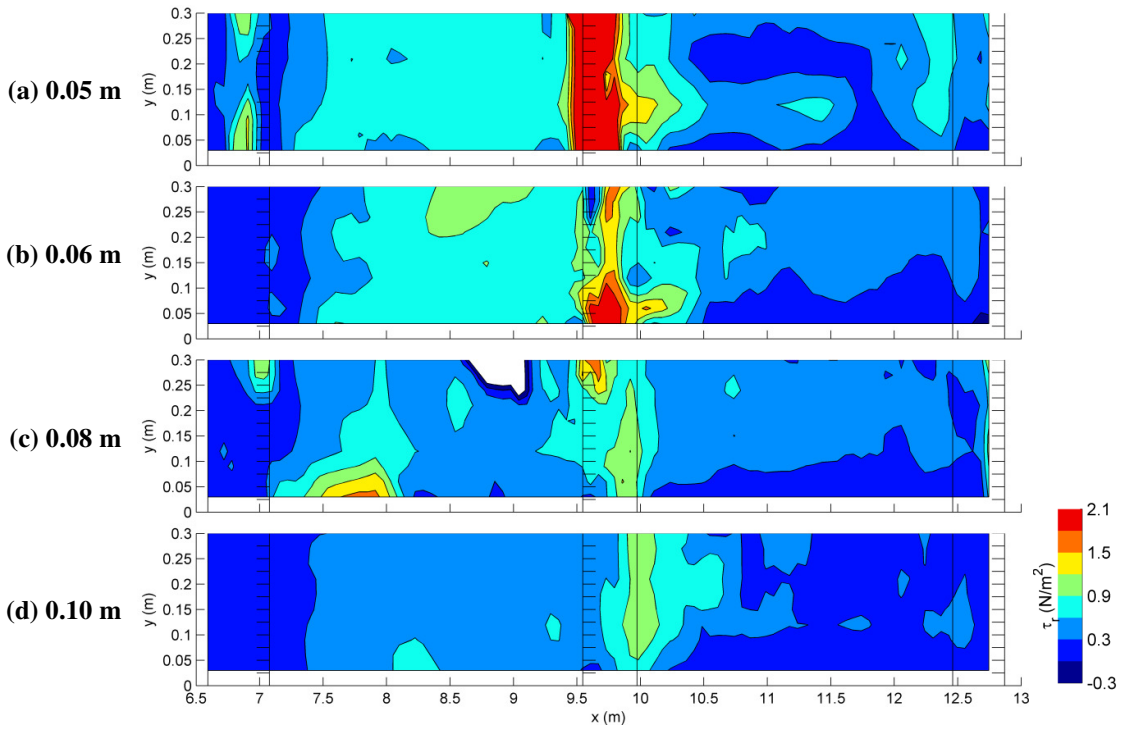

Figure 98. Shear stress estimated from the Reynolds stress profile (τ_r) in the XY plane for four different depths.

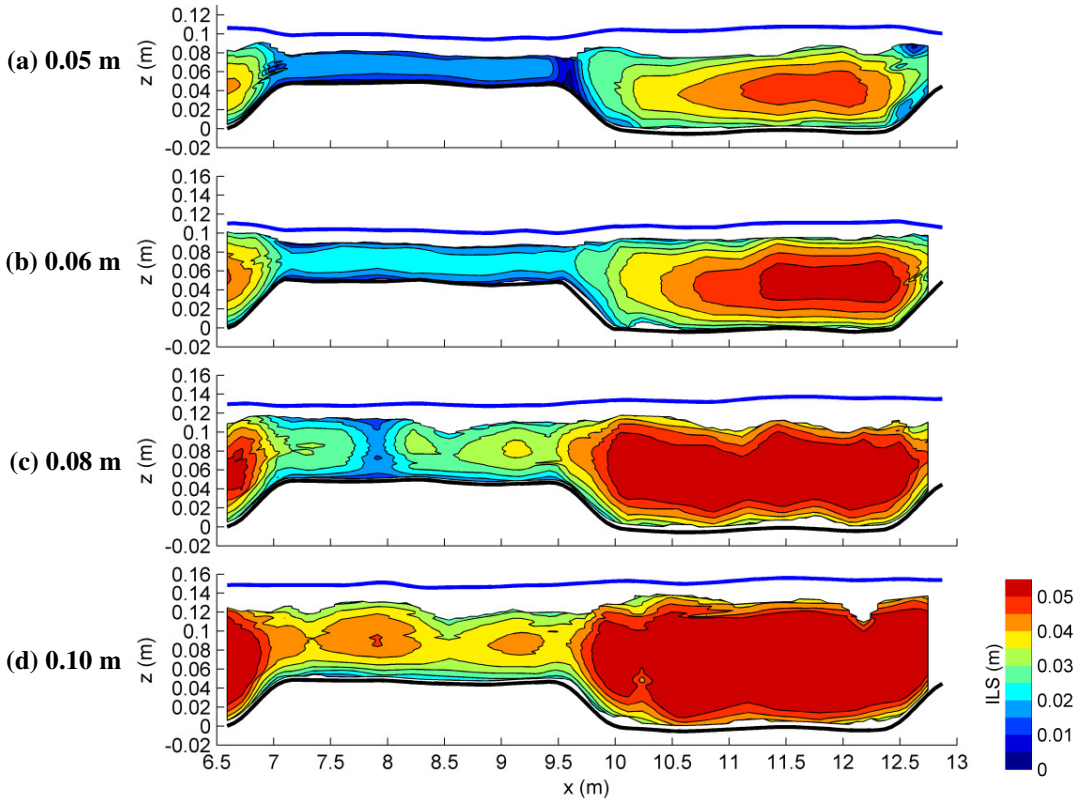

Figure 99. Integral length scale (ILS) in the XZ plane at the channel centerline (y=0.30 m) for four different depths using the US probe.

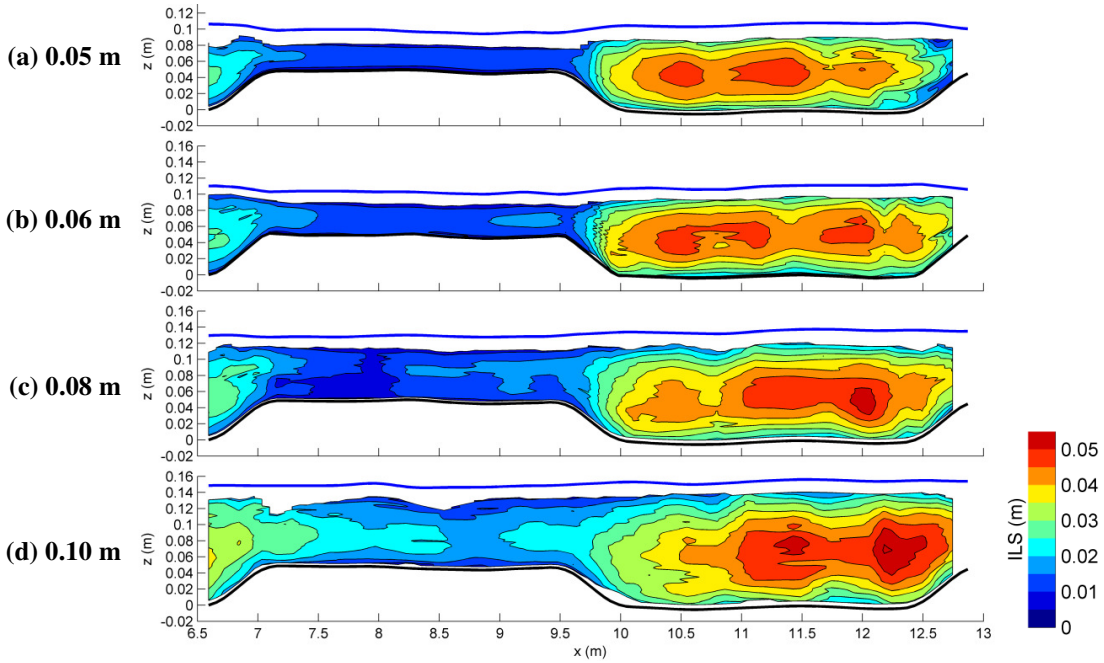

Figure 100. Integral length scale (ILS) in the XZ plane near the channel wall (y=0.03 m) for four different depths using the US probe.

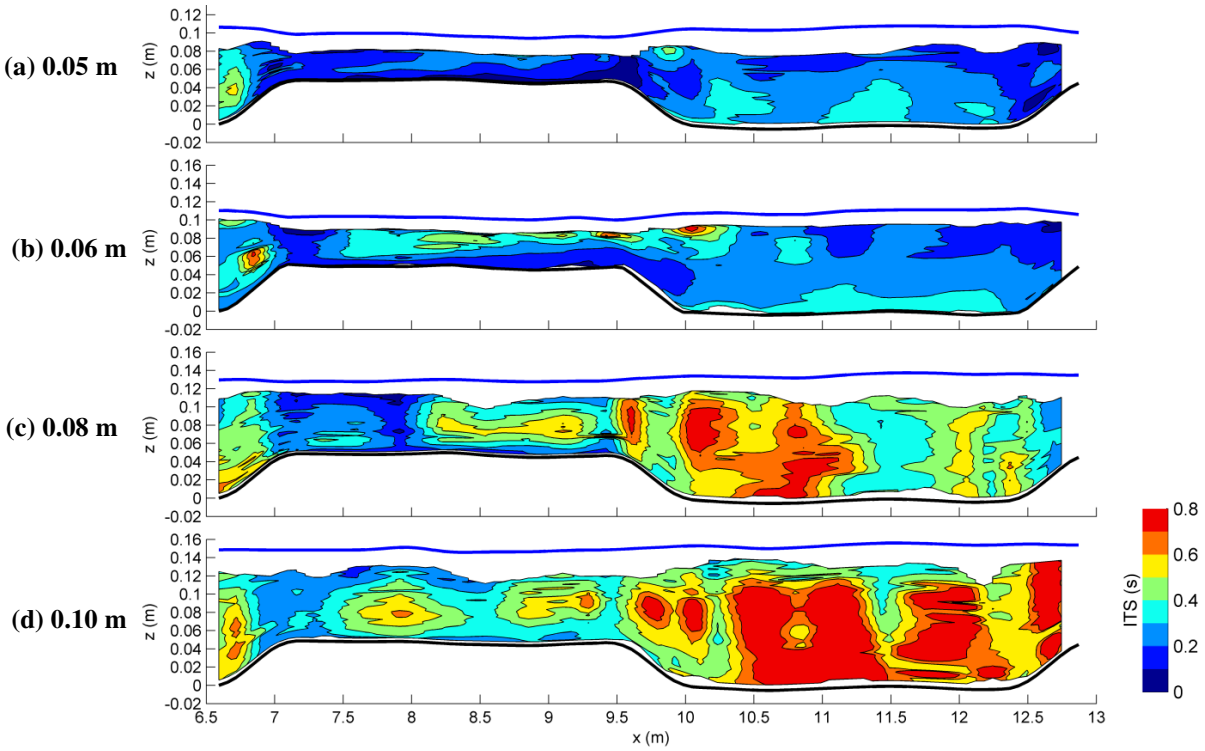

Figure 101. Integral time scale (ITS) in the XZ plane at the channel centerline (y=0.30 m) for four different depths the US probe.

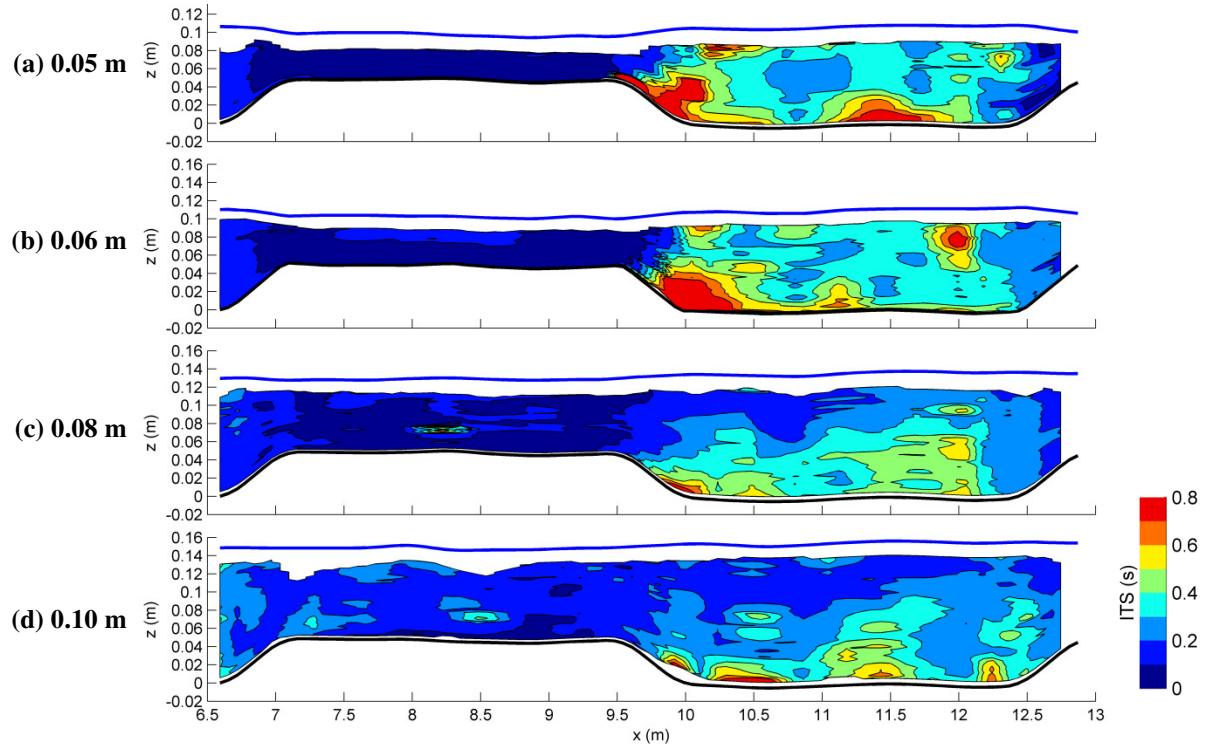

Figure 102. Integral time scale (ITS) in the XZ plane near the channel wall (y=0.03 m) for four different depths using the US probe.

Appendix E – Experimental Results for Roughness Factors

As a part of the experiment phase of this thesis, different roughness factors were tested to determine the effect channel roughness had on the hydrodynamics through the pool-riffle sequence. Three different trials were conducted using different roughness factors. The first was a smooth PVC bed and smooth side walls. The second trial used an abrasive tape material along the length of the bed surface, with the side walls remaining smooth. The third trial used this same rough material along the side walls as well as along the bed surface (Figure 103).

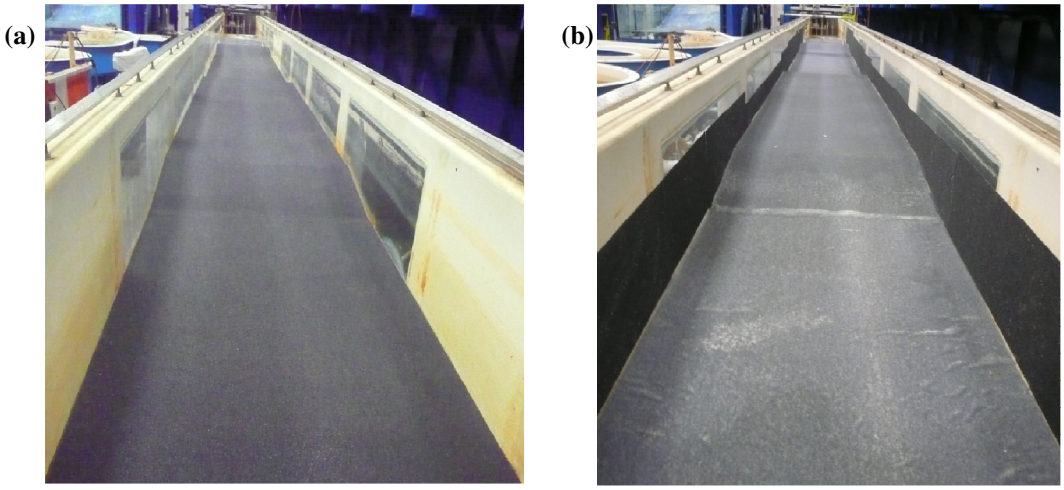

Figure 103. Pictures of the (a) bed roughness, and (b) bed and wall roughness in the flume.

The abrasive tape was classified as 46 grit on the roughness scale (Esterly, 2010). The bedform geometry was the same as that of Run7 (Table 2). The maximum Fr and Re values were in an acceptable range for the flow to be considered in the same regime as previous results (Table 7).

Table 7. Maximum Fr and Re values for the different roughness factors.

Roughness Factor	Max Fr	Max Re ($x10^4$)
Smooth	0.72	3.3
Rough Bed	0.71	3.0
Rough Bed and Wall	0.70	3.2

The following figures are the results collected from these different depths. The results follow the same format as the results in the body of the thesis, and include streamwise velocity, Π, τ_u, vertical velocity, τ_{Re}, τ_r, ILS, and ITS.

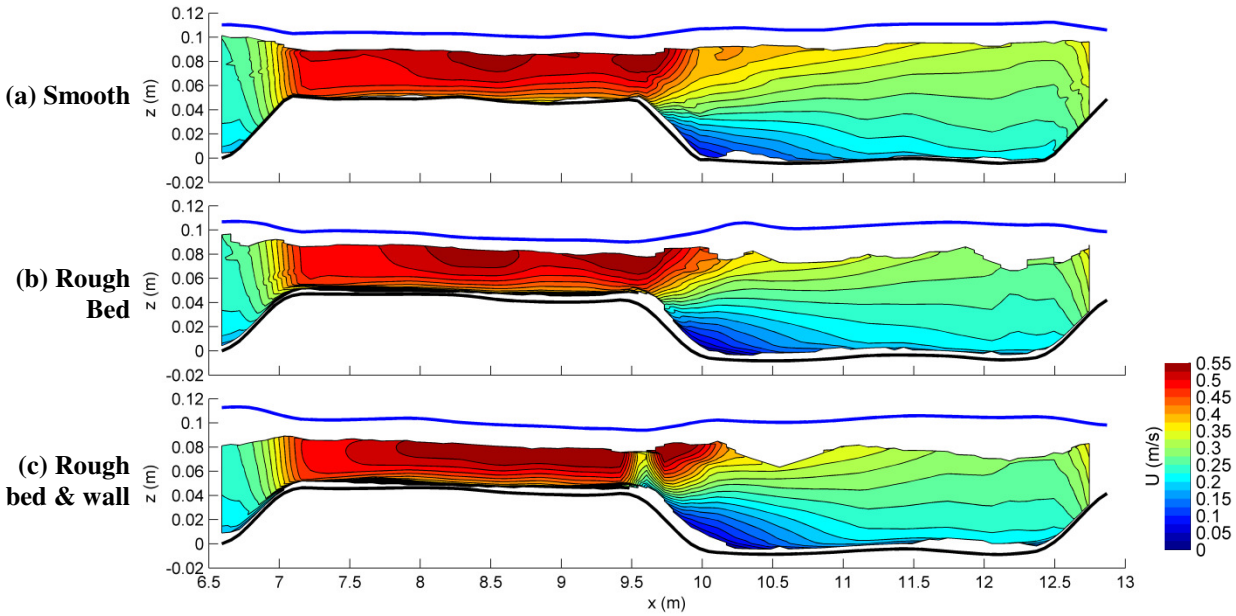

Figure 104. Mean streamwise velocity (U) in the XZ plane at the channel centerline (y=0.30 m) for different roughness factors.

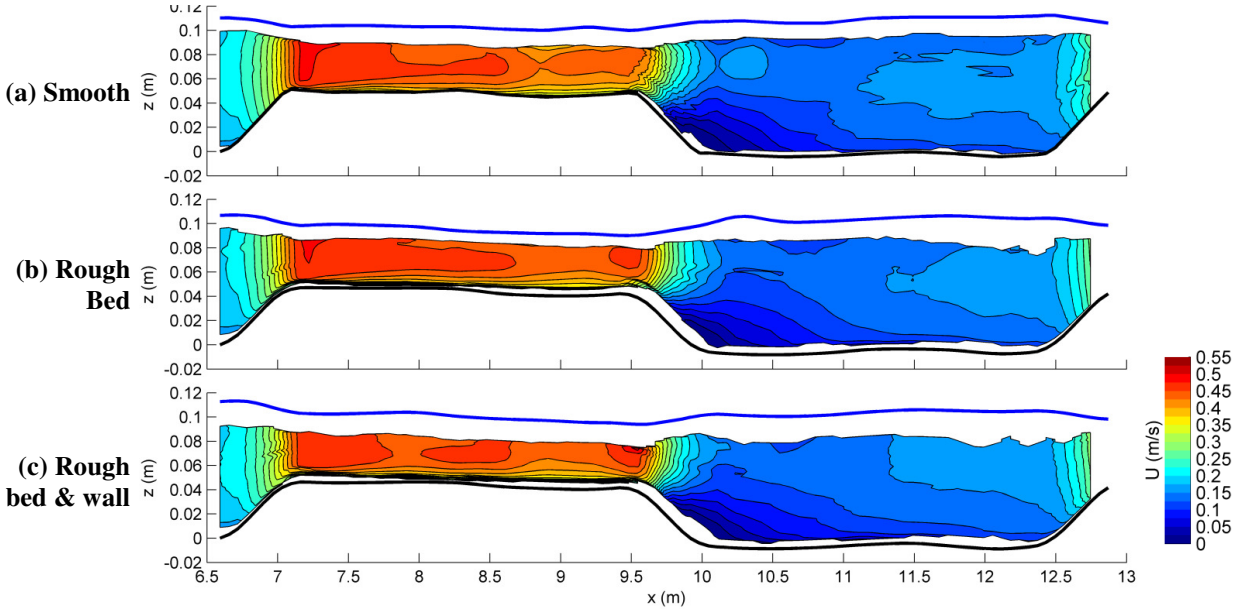

Figure 105. Mean streamwise velocity (U) in the XZ plane near the channel wall (y=0.03 m) for different roughness factors.

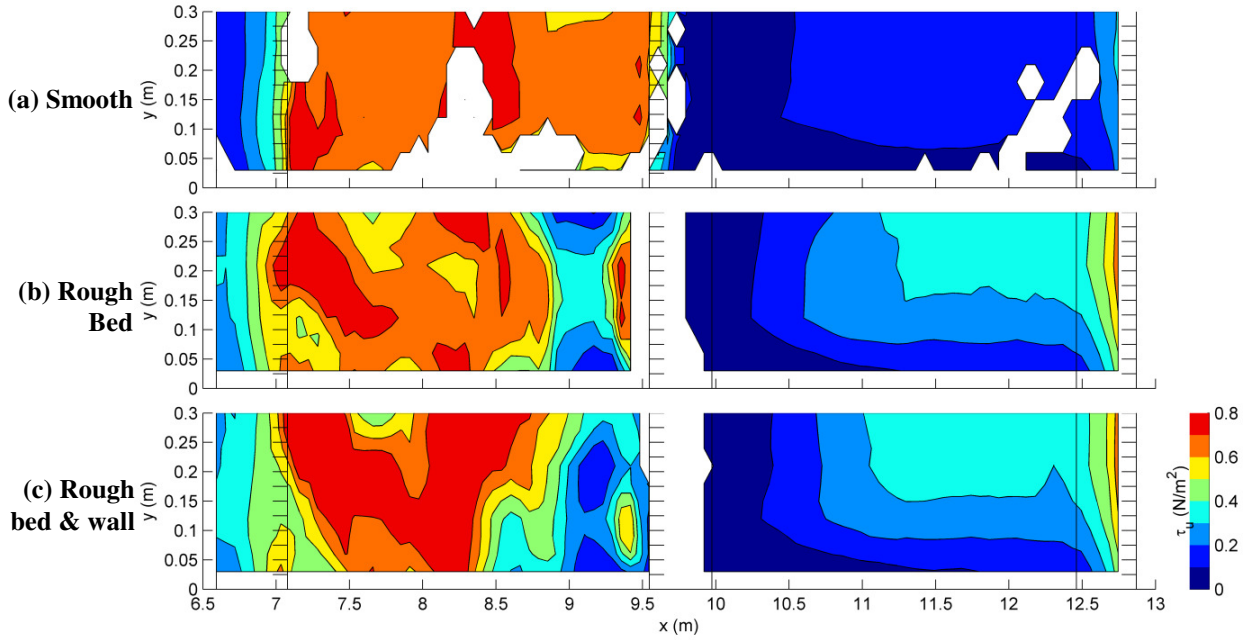

Figure 106. Shear stress estimated from the velocity profile (τ_u) in the XY plane for different roughness factors.

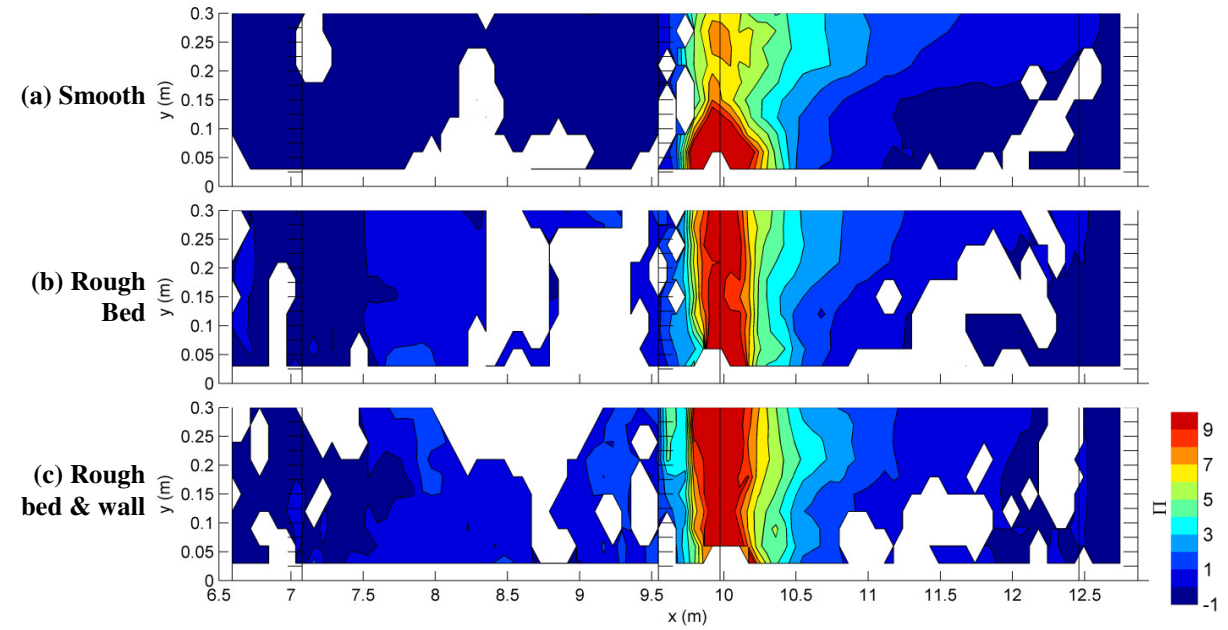

Figure 107. Coles' wake parameter (Π) in the XY plane for different roughness factors.

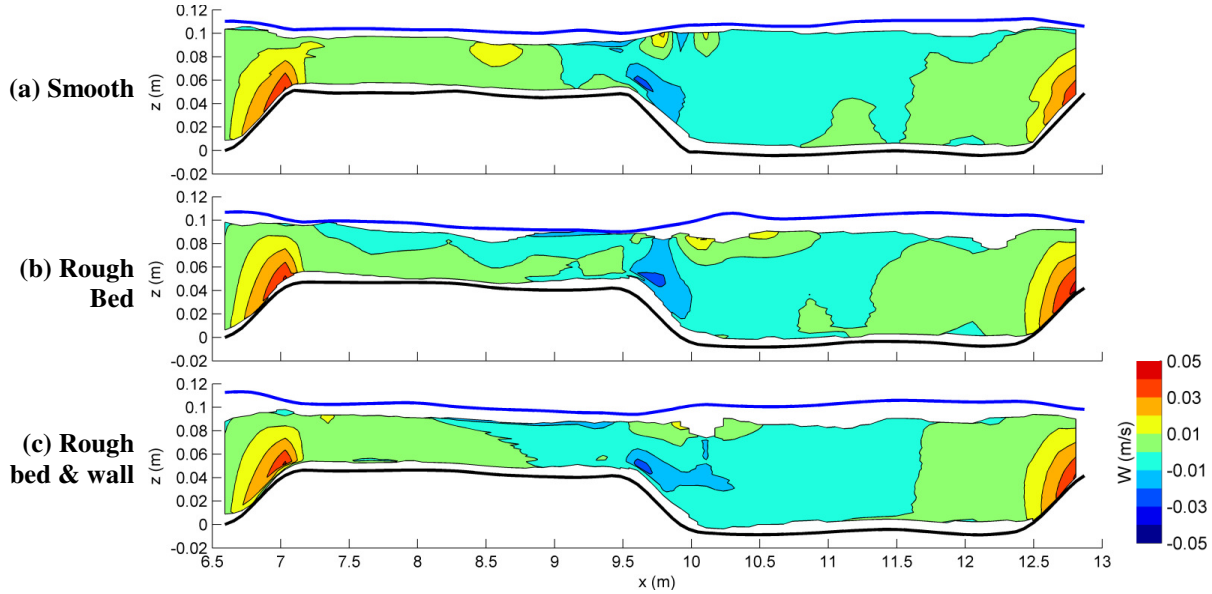

Figure 108. Mean vertical velocity (W) in the XZ plane at the channel centerline (y=0.30 m) for different roughness factors.

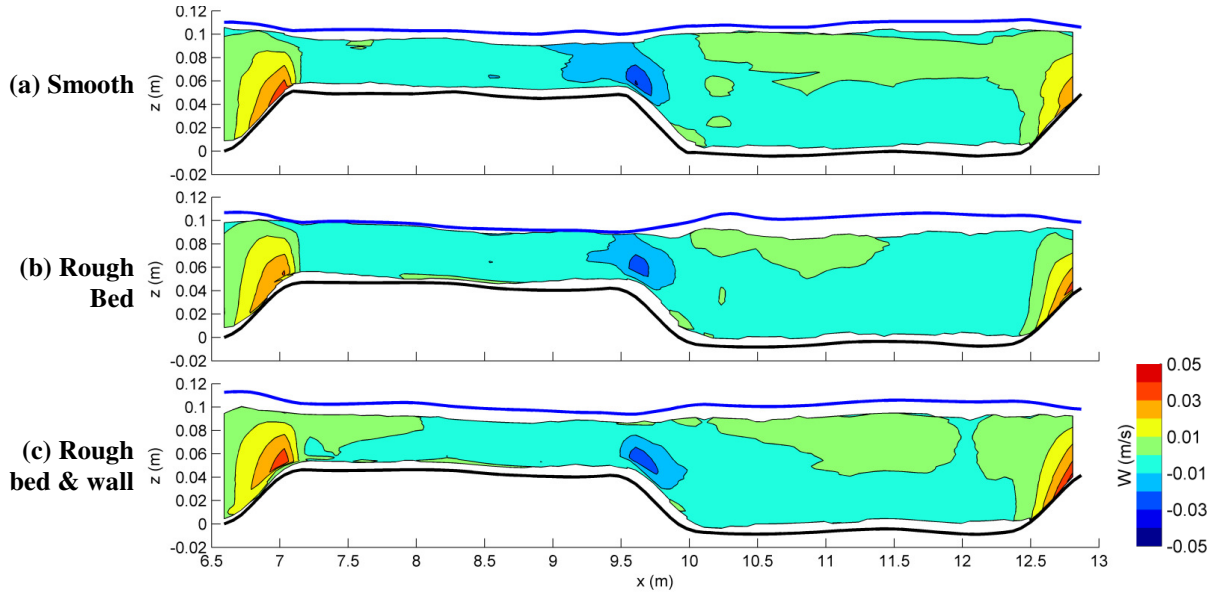

Figure 109. Mean vertical velocity (W) in the XZ plane near the channel wall (y=0.03 m) for different roughness factors.

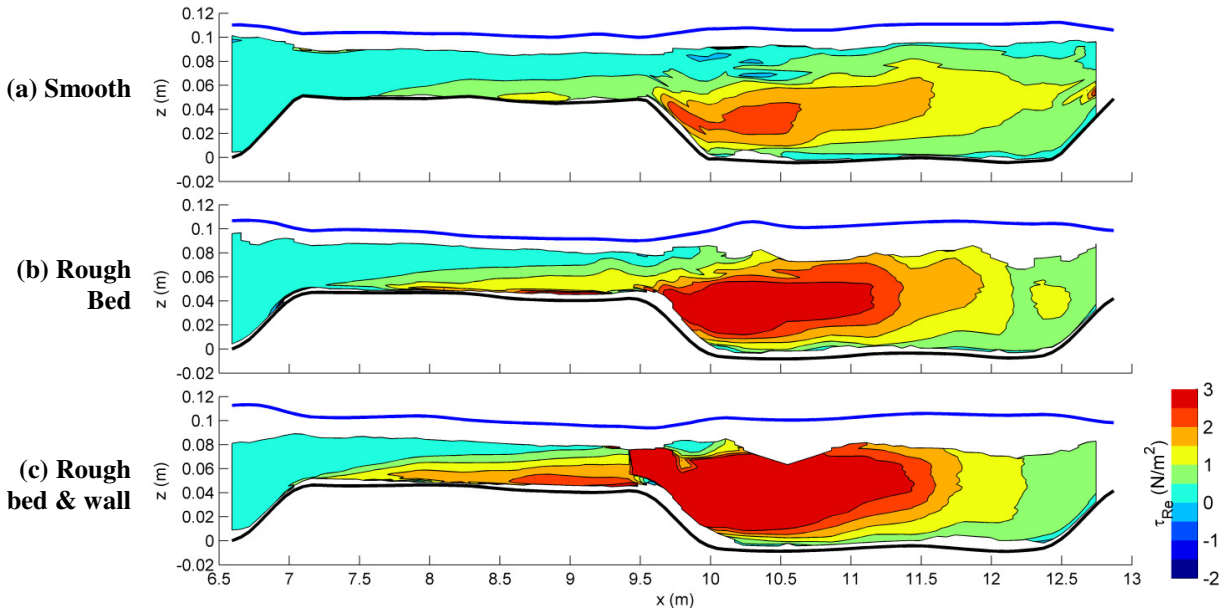

Figure 110. Reynolds stress (τ_{Re}) in the XZ plane at the channel centerline (y=0.30 m) for different roughness factors.

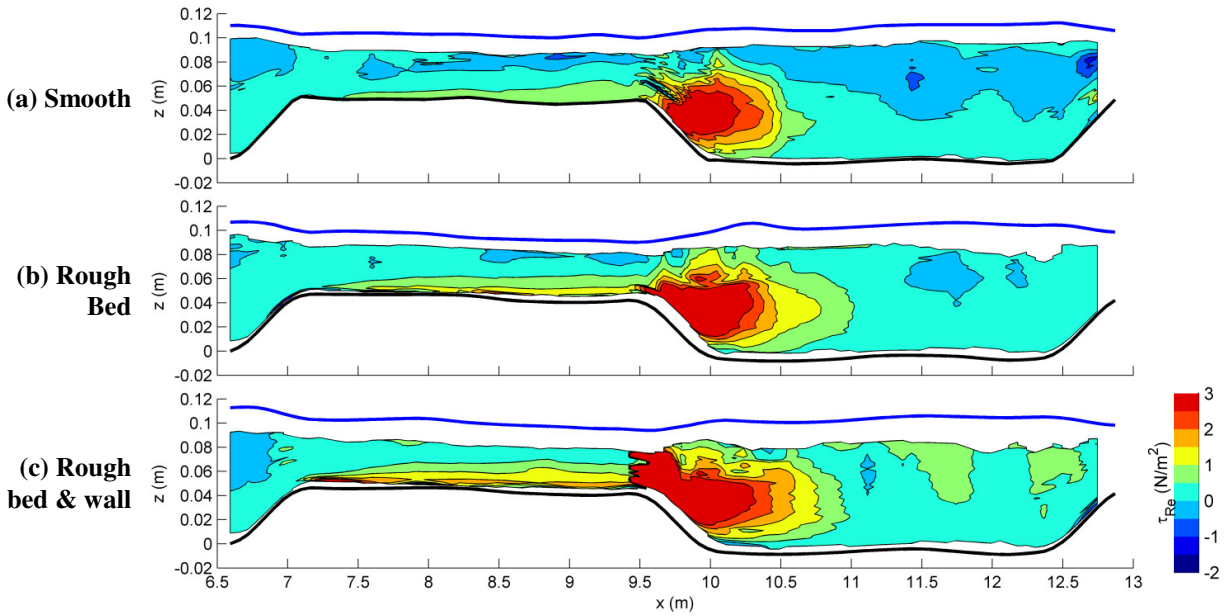

Figure 111. Reynolds stress (τ_{Re}) in the XZ plane near the channel wall (y=0.03 m) for different roughness factors.

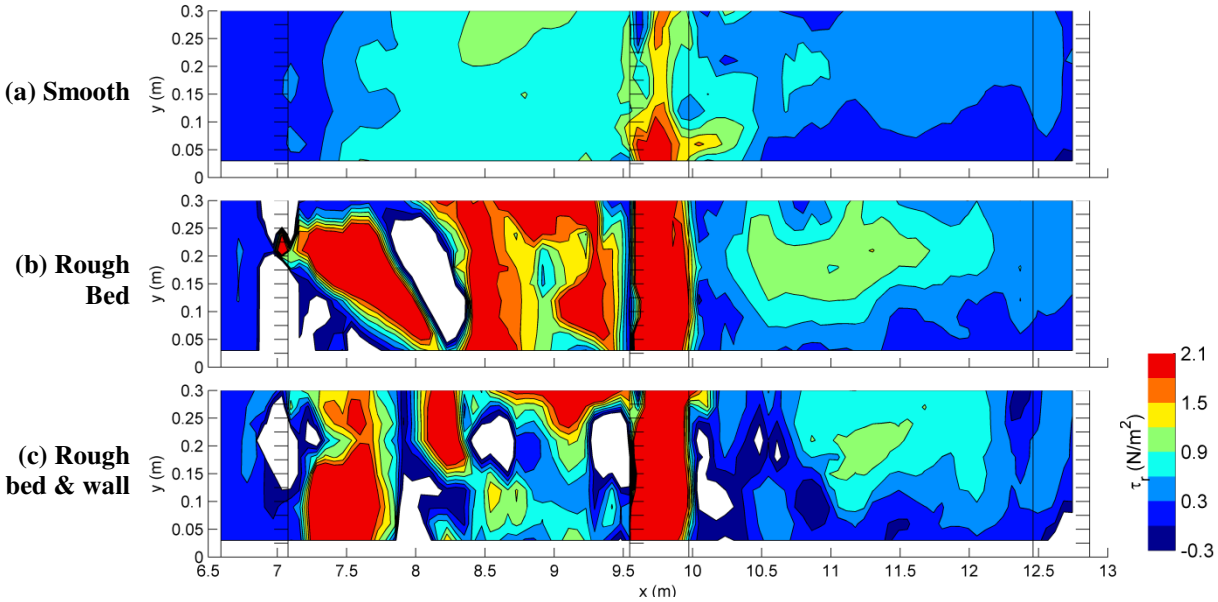

Figure 112. Shear stress estimated from the Reynolds stress profile (τ_r) in the XY plane for different roughness factors.

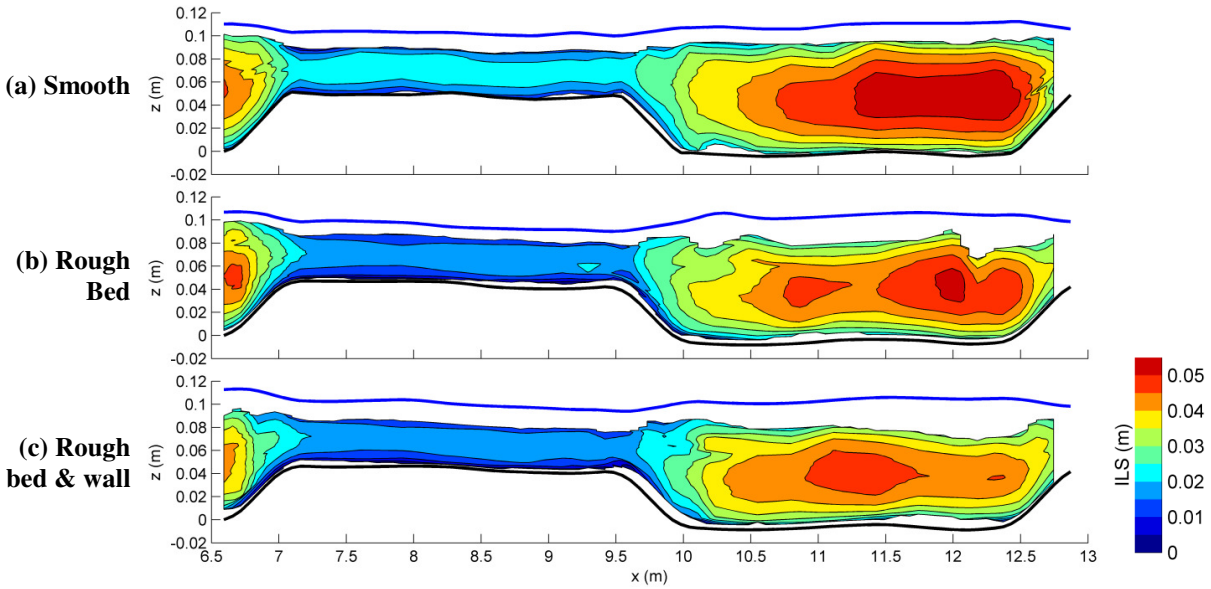

Figure 113. Integral length scale (ILS) in the XZ plane at the channel centerline (y=0.30 m) for four different depths using the US probe.

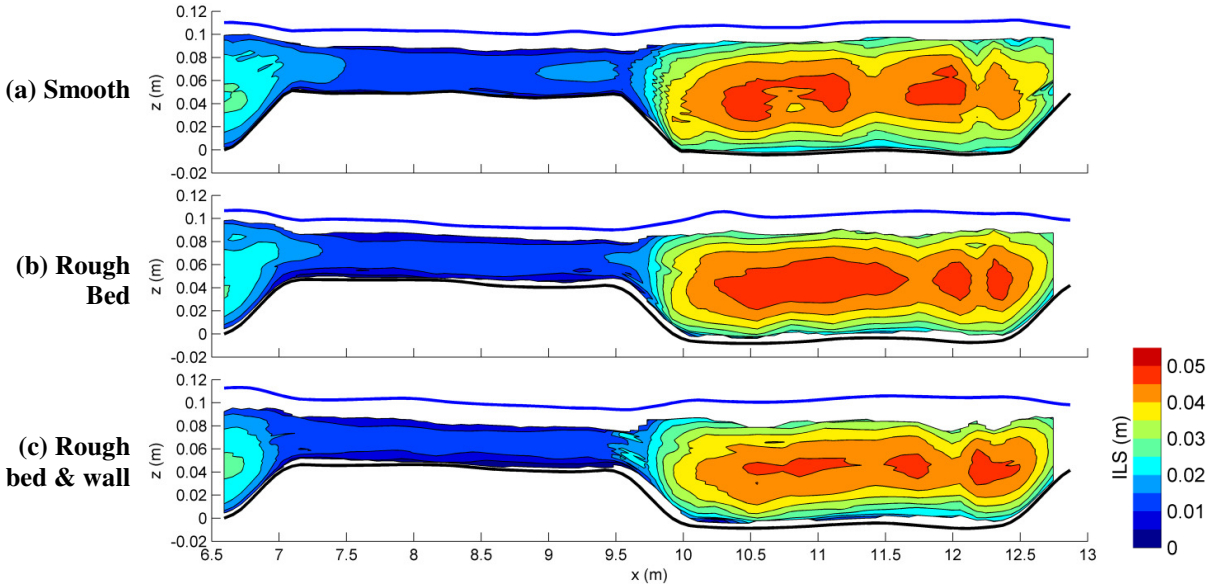

Figure 114. Integral length scale (ILS) in the XZ plane near the channel wall (y=0.03 m) for four different depths using the US probe.

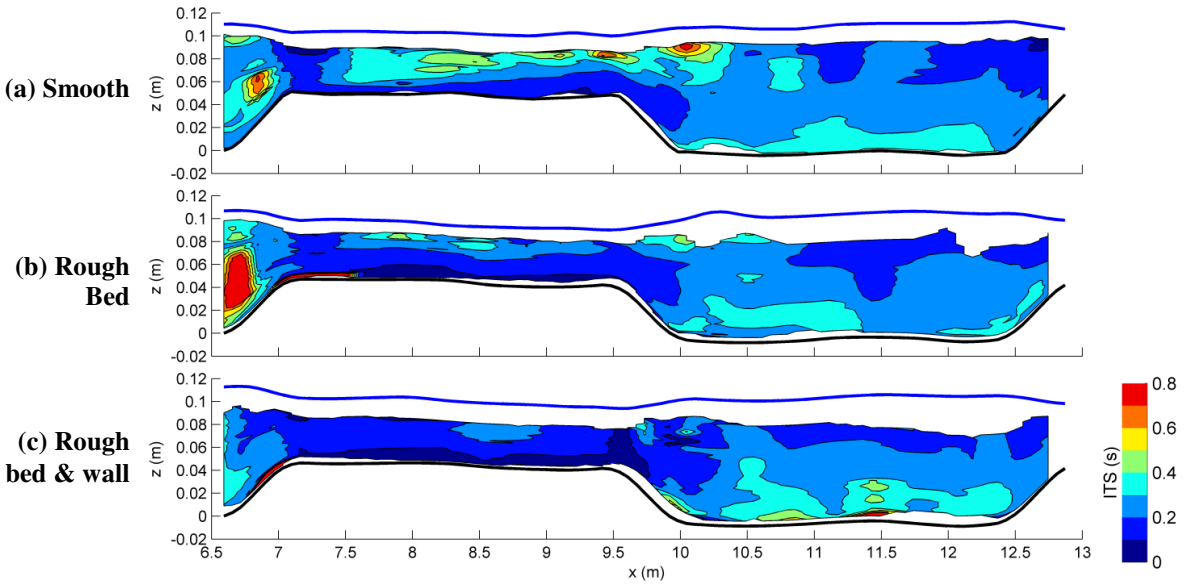

Figure 115. Integral time scale (ITS) in the XZ plane at the channel centerline (y=0.30 m) for three different roughness factors using the US probe.

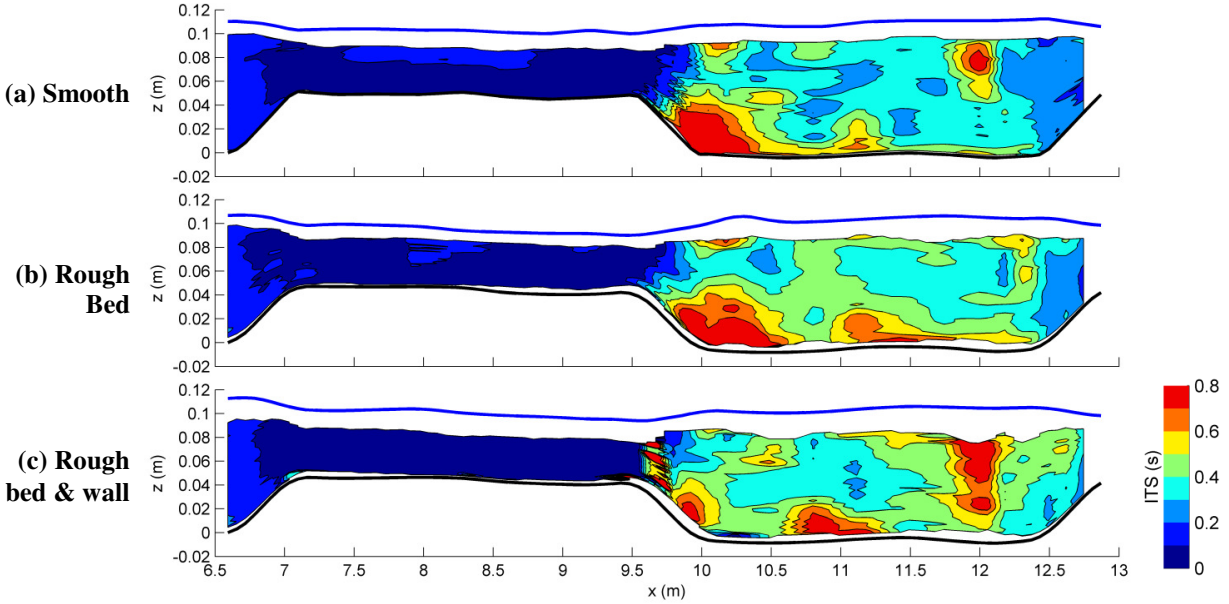

Figure 116. Integral time scale (ITS) in the XZ plane near the channel wall (y=0.03 m) for three different roughness factors using the US probe.